INFORMATION TO USERS

This manuscript has been reproduced from the microfilm master. UMI films the text directly from the original or copy submitted. Thus, some thesis and dissertation copies are in typewriter face, while others may be from any type of computer printer.

The quality of this reproduction is dependent upon the quality of the copy submitted. Broken or indistinct print, colored or poor quality illustrations and photographs, print bleedthrough, substandard margins, and improper alignment can adversely affect reproduction.

In the unlikely event that the author did not send UMI a complete manuscript and there are missing pages, these will be noted. Also, if unauthorized copyright material had to be removed, a note will indicate the deletion.

Oversize materials (e.g., maps, drawings, charts) are reproduced by sectioning the original, beginning at the upper left-hand corner and continuing from left to right in equal sections with small overlaps.

Photographs included in the original manuscript have been reproduced xerographically in this copy. Higher quality 6" x 9" black and white photographic prints are available for any photographs or illustrations appearing in this copy for an additional charge. Contact UMI directly to order.

Bell & Howell Information and Learning
300 North Zeeb Road, Ann Arbor, MI 48106-1346 USA

UMI®
800-521-0600

STUDIES OF $\Delta I = 4$ BIFURCATION IN $A \sim 150$ SUPERDEFORMED BANDS

By

DEAN STUART HASLIP, B.SC., M.SC.

A Thesis

Submitted to the School of Graduate Studies

in Partial Fulfillment of the Requirements

for the Degree

Doctor of Philosophy.

McMaster University

STUDIES OF STAGGERING IN MASS-150 SUPERDEFORMED BANDS

DOCTOR OF PHILOSOPHY (1998) McMaster University
(Physics) Hamilton, Ontario

TITLE: Studies of $\Delta I = 4$ Bifurcation in $A \sim 150$ Superdeformed Bands

AUTHOR: Dean S. Haslip, B.Sc. (McMaster University),
M.Sc. (Queen's University)

SUPERVISOR: Dr. J. C. Waddington

NUMBER OF PAGES: x, 135

Abstract

When some nuclei are excited to tens of MeV above their ground state, with angular momenta so high that they are on the verge of fissioning, they can take on cigar-like shapes with axis ratios of 2 : 1, so-called superdeformed shapes. These superdeformed nuclei de-excite by the emission of cascades of γ rays (a superdeformed band). One of the most puzzling aspects of this emission is the phenomenon called $\Delta I = 4$ bifurcation, or staggering, in which every second γ-ray energy in a given superdeformed band is shifted upward relative to the other energies in the band. Very little is known about this phenomenon, making a systematic investigation necessary.

In this thesis, $\Delta I = 4$ bifurcation has been studied in twenty-two bands in europium and gadolinium nuclei with mass numbers A near 150. The results obtained include the observation that the staggering patterns in three identical bands (bands with identical moments of inertia) are very highly correlated. This result seems to agree with what one might expect from a restrictive interpretation of the model of Hamamoto and Mottelson, and the staggering patterns in these three bands are used to constrain the model parameters for this triplet of bands.

This systematic survey of $\Delta I = 4$ bifurcation has been used to rigorously test the model of Pavlichenkov, and that of Hamamoto and Mottelson. It is demonstrated that neither of these models is capable of explaining the results presented.

Finally, a statistical analysis of the staggering patterns presented in this thesis is proposed and carried out. This analysis underlines the highly non-statistical nature of the staggering phenomenon, but also emphasizes the importance of independent verification of these results.

Acknowledgements

I would first like to thank my wife Deanne for her love and support and for keeping me in the manner to which I've become accustomed.

In my two years as a graduate student and three years as a summer student with the McMaster nuclear structure group, I have had the privilege of working with a number of exceptional people. This group includes Jim Waddington, Simon Mullins, Daniel Prévost, Greg Hackman, John Cameron, Stéphane Flibotte, Jon Wilson, John Nieminen, and Carl Svensson. These people have been a tremendous source of nuclear physics knowledge and experience, and of friendship.

I would also like to thank Roby Austin, Tom Rodinger, Tim Lampman, Bryan "Byron" Schaly, and Joanne O'Meara for making it a pleasure to come to work every day.

Contents

1 Introduction to Superdeformation 1

1.1 Nuclear Models . . . 2

1.1.1 The Single-Particle Model . . . 3

1.1.2 Collective Models . . . 5

1.1.3 Deformation Parameters . . . 7

1.2 Superdeformation: Physics in the Second Well . . . 9

1.2.1 Superdeformed Fission Isomers . . . 9

1.2.2 Intruders . . . 11

1.3 The Mass-150 Region . . . 11

2 Theory of Superdeformed Bands 15

2.1 The Particle-Rotor Model . . . 15

2.2 Alignments . . . 17

2.2.1 Effective Alignment . . . 18

2.2.2 Incremental Alignment . . . 20

2.3 Routhian Diagrams . . . 21

2.4 Identical Bands . . . 23

2.4.1 Theoretical Explanations . . . 26

2.5 $\Delta I = 4$ Bifurcation . . . 28

2.5.1 Experimental Evidence 28
2.5.2 Theoretical Efforts 31

3 Experimental Techniques **36**

3.1 Heavy-Ion Fusion-Evaporation Reactions 36
3.2 Gamma-Ray and Charged-Particle Detectors 38
3.2.1 Solid-State Detectors 39
3.2.2 Scintillators 40
3.3 Coincidence Spectroscopy 41
3.3.1 Multiple Gating 44
3.3.2 Elliptical Gating 46
3.3.3 Spike-Free Incrementation 47
3.4 Background Subtraction 49
3.4.1 Background Subtraction in Higher Folds 51

4 Staggering in Identical Bands **53**

4.1 Motivation for the Experiment 53
4.2 The Experiment 56
4.3 Experimental Results 58
4.3.1 New Bands 58
4.3.2 Transition Energy Determination 58
4.3.3 Staggering 61
4.4 Interpretation of the Staggering Results 68
4.4.1 Sinusoidal Staggering 68
4.4.2 A More Complete Description 70
4.4.3 Implications for Pavlichenkov 75

5 Further Studies of Staggering **77**

5.1 Staggering in ^{148}Eu(2) 77

5.2 Staggering in ^{147,148}Gd 80

5.2.1 Motivations 80

5.2.2 Bands Not Analyzed 82

5.2.3 Results 82

5.3 Staggering in ^{147}Eu 87

5.4 Staggering in ^{150,151}Gd 93

5.5 Statistical Considerations 100

6 Conclusions **106**

6.1 $\Delta I = 4$ Bifurcation in Identical Bands 106

6.2 Systematic Survey of $\Delta I = 4$ Bifurcation 108

6.2.1 Tests of the Models 108

6.2.2 Statistical Significance 111

6.3 Future Prospects 112

A Oscillation of the Tunneling Amplitude **114**

B Calculation of the Staggering Amplitude **118**

C Glossary of Symbols **122**

Bibliography **127**

List of Figures

1.1 Shell gaps in a Woods-Saxon potential. 4

1.2 Fission barrier with and without shell corrections. 10

1.3 Typical superdeformed band in the $A \sim 150$ region. 12

2.1 Schematic diagram defining the effective alignment. 19

2.2 Representative Routhian diagram. 22

2.3 Identical and non-identical superdeformed bands. 25

2.4 Moment of inertia of ^{149}Gd(1). 29

2.5 Construction of a staggering plot. 30

2.6 Moments Q_{44} for $J = 13/2$ and $J = 15/2$ subshells. 34

3.1 Illustration of the Compton background. 40

3.2 A demonstration of coincidence spectroscopy. 42

3.3 Partial level schemes of ^{146,147}Eu. 43

3.4 Multiple gating of a superdeformed band. 45

3.5 Contour plot of a two-dimensional Gaussian distribution. 47

4.1 Single-particle Routhians at deformations appropriate to the $A \sim 150$ region. 55

4.2 Partial γ-ray spectra of ^{148}Eu(1) and ^{148}Gd(6). 60

4.3 Staggering patterns for ^{148}Eu(1) and ^{148}Gd(6). 62

4.4 Systematic uncertainties in a staggering plot. 66
4.5 Identical band staggering patterns plotted as a function of spin. . . . 69
4.6 Good fits to the identical band staggering data. 72
4.7 Poor fits to the identical band staggering data. 73

5.1 Spectrum and staggering plot for ^{148}Eu(2). 79
5.2 Staggering plot for ^{148}Gd(5). 84
5.3 The effect of the 7_1 intruder on $\Delta I = 4$ bifurcation. 85
5.4 Staggering plots for cases involving $N = 6$ neutron orbitals. 86
5.5 Staggering plots for bands in ^{147}Eu. 91
5.6 Staggering plots as a function of spin for two triplets of identical superdeformed bands. 92
5.7 Staggering plots for bands in ^{150}Gd identical to ^{149}Gd(1). 96
5.8 Staggering plots for bands identical to ^{150}Gd(1). 98
5.9 Staggering plots for more bands in ^{150}Gd. 100
5.10 Staggering significance for the bands analyzed in this work. 103

List of Tables

4.1 Gamma-ray transition energies of the superdeformed bands ^{148}Eu(1) and ^{148}Gd(6). 61

4.2 Staggering significance for ^{149}Gd(1), ^{148}Eu(1), and ^{148}Gd(6). 67

4.3 Parameters for the Hamamoto and Mottelson Hamiltonian. 74

5.1 Single-particle configurations for superdeformed bands in ^{148}Eu. . . . 78

5.2 Gamma-ray transition energies of ^{148}Eu(2). 80

5.3 Single-particle configurations for superdeformed bands in ^{147,148}Gd. . 81

5.4 Gamma-ray transition energies of the superdeformed bands in ^{147,148}Gd. 83

5.5 Single-particle configurations for superdeformed bands in ^{147}Eu. . . . 89

5.6 Gamma-ray transition energies for bands in ^{147}Eu. 90

5.7 Single-particle configurations for superdeformed bands in ^{150,151}Gd. . 94

5.8 Gamma-ray transition energies for bands in ^{150}Gd. 95

5.9 Gamma-ray transition energies for bands in ^{151}Gd. 97

5.10 Staggering significance for the bands studied in this work. 102

6.1 Tests of Pavlichenkov's model. 110

Chapter 1

Introduction to Superdeformation

The nucleus is a system whose complexities are still a long way from being understood. Although current understanding of nucleon-nucleon interactions is probably sufficient to allow a solution of this quantal many-body problem in principle, the volume of calculations required to achieve this goal puts it out of reach for now. The nucleus also defies descriptions with the methods of statistical mechanics, since the assumptions of statistical physics break down when the system of interest consists of only a few hundred particles. These facts make the nucleus an exciting laboratory, full of surprises.

Since the nucleus is a bound quantal system, its excited states consist of a discrete collection of energy levels. Discovering these levels and measuring and interpreting their properties is the essence of low- and medium-energy nuclear physics. Experimentally, these levels are investigated in many ways, from resonant production to radioactive decay. The nuclear structure group at McMaster University studies these levels by observing the γ rays emitted as the nucleus de-excites to its ground state.

As discussed in Section 1.1, the properties of these levels may sometimes be understood by supposing that the levels are excitations of single protons or neutrons.

They may also sometimes be characterized as so-called "collective" excitations of the nucleus, like rotations or vibrations, or as a combination of collective and single-particle behaviour.

This thesis is a study of superdeformed (SD) bands, a type of collective structure obtained when the nucleus takes on a cigar shape with an axis ratio of almost 2:1. More specifically, it is an examination of fine perturbations in these superdeformed levels called $\Delta I = 4$ bifurcation, or staggering. The study is restricted to superdeformed bands in the nuclei ^{147,148}Eu and $^{147-151}$Gd.

This chapter provides a brief introduction to nuclear physics, with an emphasis on superdeformation in the $A \sim 150$ region*. Chapter 2 explores more deeply some of the relevant background to this work, including detailed explanations of what is meant by "$\Delta I = 4$ bifurcation" and "identical bands". Some of the experimental techniques that have been used in this work to study superdeformed bands are discussed in Chapter 3. Chapter 4 describes an experiment which was performed in order to study $\Delta I = 4$ bifurcation in ^{147}Gd and ^{148}Eu, and the key results which came from it. In Chapter 5, data from a number of experiments are analyzed similarly, providing the first systematic survey of $\Delta I = 4$ bifurcation. The conclusions drawn from this work are presented in Chapter 6.

1.1 Nuclear Models

As mentioned above, the exact solution of the nuclear system is beyond the reach of today's computers. As a result, the theoretical efforts to understand the nucleus must rely on models of the nucleus. This section discusses the two basic families of nuclear models, the single-particle and collective models.

*A is the nuclear mass. See Appendix C for a glossary of symbols used in this thesis.

1.1.1 The Single-Particle Model

Figure 1.1 shows the energy levels of the neutrons in the nucleus as a function of a deformation parameter β. The proton energy levels are qualitatively similar. There are a number of gaps in the energy-level spectrum for spherical nuclei ($\beta = 0$). At "magic" particle numbers 28, 40, 50, 64, and 82, spherical shapes are particularly stable. Deformations are energetically costly, as are single-particle excitations. This link between energy gaps and stability arises often in physics, including the lack of reactivity of noble gases, the insulating properties of solids with filled electron bands, and the stability of the BCS ground state of superconductors.

The energy levels of a nucleus such as $^{147}_{65}\mathrm{Tb}_{82}$ or $^{57}_{28}\mathrm{Ni}_{29}$, with one proton or neutron outside a doubly-magic core, can be thought of as the excitations of that one particle in the potential created by the nucleons in the core [Kra88]. The single-particle model, or shell model, uses the energy levels derived in this way, along with a model of nucleon interactions (so-called "residual interactions") to determine the properties of nuclei with many particles outside the core. Nuclear states derived in this way can be identified with specific configurations of particles, or mixtures thereof. This is a very convenient way to think of the excited states, and a lot of effort goes into performing these shell-model calculations.

This approach becomes very computationally intensive extremely quickly. At present, the most powerful supercomputers have only been able to do shell-model calculations for nuclei with masses up to $A \sim 50$ [Cau94, Mar97]. Thus, for heavier nuclei one is forced to abandon these techniques and make more assumptions about the nucleus before beginning.

A poor-man's version of the shell model is a mean-field model. A mean-field model assumes that each nucleon moves in an average potential which is the

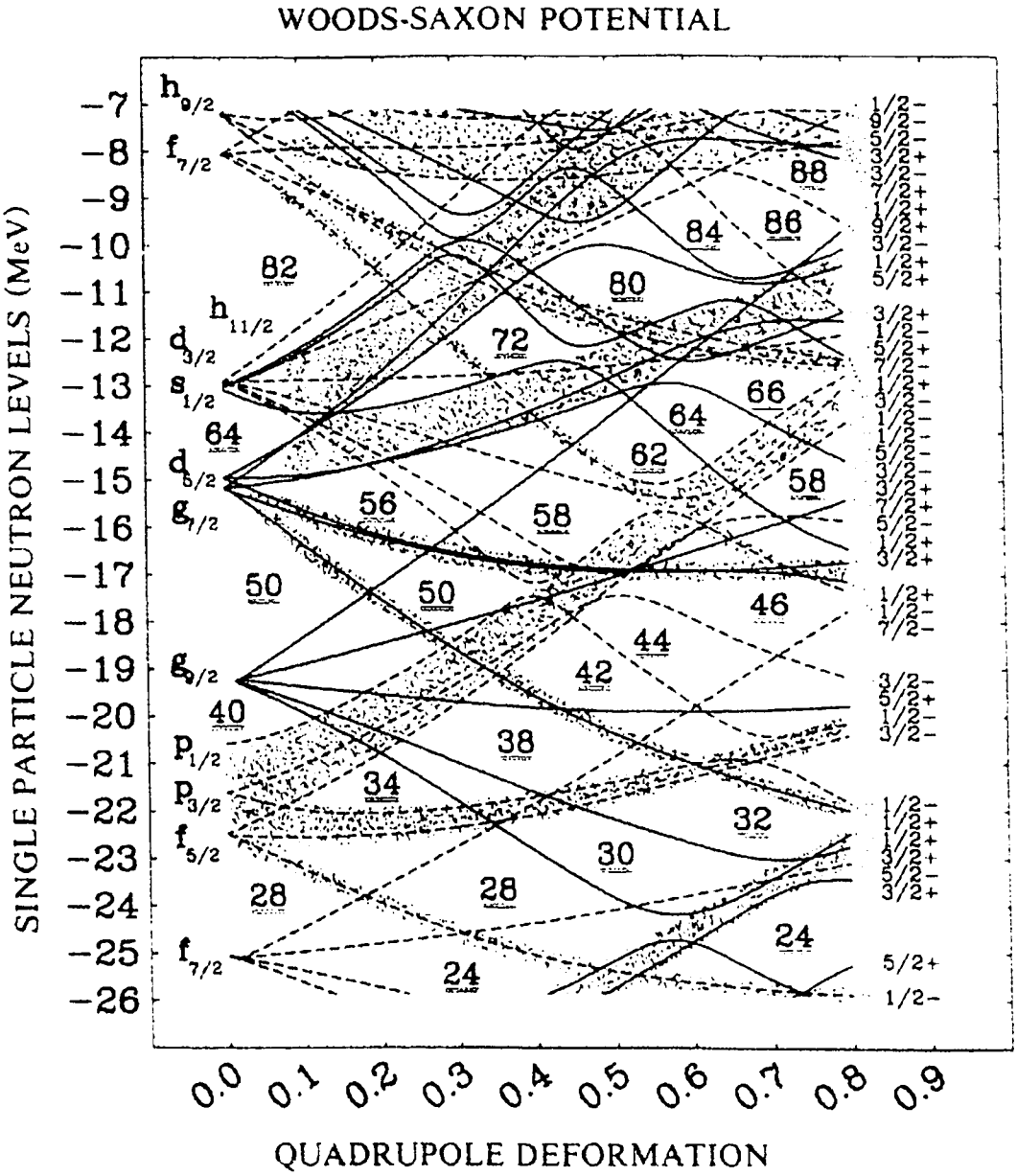

Figure 1.1: Shell gaps in a Woods-Saxon potential[Dud87]. Particle numbers at various gaps are shown. At zero deformation, the orbitals are labelled with the spectroscopic notation l_j, where l (j) is the orbital (total) angular momentum of the particle. At large deformation, they are labelled by the projection of their angular momentum on the symmetry axis of the nucleus, and by their parity. Shaded regions denote regions of higher level density.

result of its interactions with all of the other nucleons. This method circumvents the complicated diagonalizations inherent in shell-model calculations, including the calculation of residual interactions. The energy levels of individual particles are found by solving the Schrödinger equation (or Dirac equation, for relativistic models) for these particles in the mean-field potential. This is followed by mixing calculations for those orbitals with the same quantum numbers.

1.1.2 Collective Models

One simplifying assumption that has been extremely useful is that the nucleons can participate in coherent, or collective, excitations. These excitations can be related to the semi-classical excitations of a liquid drop, and include vibrations and rotations [Boh51]. The rotations are of interest in this thesis.

Quantum mechanically, collective rotation around a symmetry axis is forbidden [Boh75]. This arises because rotations about such an axis do not change the wave function, so that the rotating body is indistinguishable from the non-rotating one. This wave function can have only one energy eigenvalue, corresponding to the non-rotating state. The upshot of this is that spherical nuclei are not allowed to undergo collective rotation. Many nuclei, however, are prolate-deformed (sausage-shaped) in their ground or excited states and may rotate perpendicular to their axis of symmetry.

The energy levels E of a rotational nucleus with angular momentum I are those of a quantum rigid rotor:

$$E(I) = \frac{\hbar^2}{2\mathcal{J}} I(I+1). \tag{1.1}$$

This collection of states is called a rotational band. The states in a rotational band have angular momenta I, $I+2$, $I+4$, ..., as a result of symmetry considerations [Pre75]. The quantity $\mathcal{J}$ is the moment of inertia of the nucleus. In nuclear

physics, two moments of inertia, the kinematical moment $\mathcal{J}^{(1)}$ and the dynamical moment $\mathcal{J}^{(2)}$ are used. The kinematical moment is defined in terms of the first difference of the rotational energy, that is the energies of the γ rays connecting these states. Using Equation 1.1, one can show that

$$E(I) - E(I-2) = \frac{\hbar^2}{2\mathcal{J}^{(1)}}((I(I-1) - (I-2)(I-1)), \tag{1.2}$$

$$\text{ie: } E_\gamma(I \rightarrow I-2) = \frac{\hbar^2}{2\mathcal{J}^{(1)}}(4I-2) \tag{1.3}$$

where $E_\gamma(I \rightarrow I-2)$ is the energy of the γ ray connecting the states with spins I and $I-2$. To evaluate the moment of inertia with this expression requires knowledge of the nuclear angular momenta, and so is of no use in studies of many superdeformed bands, where the spins are not known. Hence the popularity of the dynamical moment, which is independent of I and is based on the second difference of the rotational energy (the difference in adjacent γ-ray energies), as follows:

$$E_\gamma(I+2 \rightarrow I) - E_\gamma(I \rightarrow I-2) = \frac{\hbar^2}{2\mathcal{J}^{(2)}}((4(I-2)-2) - (4I-2)) \tag{1.4}$$

$$\Delta E_\gamma(I) = \frac{4\hbar^2}{\mathcal{J}^{(2)}} \tag{1.5}$$

$$\mathcal{J}^{(2)} = \frac{4\hbar^2}{\Delta E_\gamma(I)}. \tag{1.6}$$

At this time, it is also useful to introduce the rotational frequency ω. This variable is semi-classical in nature, describing the rate of rotation of the nuclear liquid drop. To relate it to experimental quantities, one uses the classical expression

$$\omega = \frac{dE}{dI}. \tag{1.7}$$

For a rotational band, finite differences replace the derivative, so $\omega = \Delta E/\Delta I$. The change in energy ΔE is just the γ-ray energy, E_γ. The change in I is always $2\hbar$. Thus, the rotational frequency is given by

$$\hbar\omega = \frac{E_\gamma}{2}. \tag{1.8}$$

The combination of mean-field and collective models has been tremendously useful in describing the structure of rotational states in nuclei. In this case, the mean field potential must be deformed, to reflect the deformation of the collective nucleus. One of the most popular deformed mean-field models is the Nilsson model.

The Nilsson model [Nil55] employs an anisotropic harmonic oscillator potential with the commonly used spin-orbit and l^2 corrections. Using two large oscillator frequencies and one smaller one simulates a prolate nucleus, appropriate to the discussion of deformed rotational structures, including superdeformed bands.

The importance of the Nilsson model to this thesis is one of nomenclature. The use of the Nilsson model is so wide-spread that one commonly labels the single-particle orbitals with their quantum numbers in the Nilsson model, even when the calculations do not involve the model in any other way. These quantum numbers,valid in the limit of large prolate deformation, are the so-called asymptotic Nilsson quantum numbers, or Nilsson numbers $(N, n_3, \Lambda, \Omega)$ (commonly written as $[Nn_3\Lambda]\Omega$). The quantity n_3 is the number of oscillator quanta along the long axis of the prolate shape and N is the total number of oscillator quanta along all three axes. The symbols Λ and Ω denote the projections of the orbital and total angular momenta, respectively, onto the long axis.

1.1.3 Deformation Parameters

This thesis concerns deformed nuclei, and therefore requires a way to quantitatively describe this deformation. One of many sets of deformation parameters is discussed in this section.

The surface of the nucleus may be described [Rin80] by the function $R(\theta, \phi)$:

$$R(\theta, \phi) = R_0 \left(1 + a_{00} + \sum_{\lambda=1}^{\infty} \sum_{\mu=-\lambda}^{\lambda} a^*_{\lambda\mu} Y_{\lambda\mu}(\theta, \phi) \right). \tag{1.9}$$

where $Y_{\lambda\mu}$ are spherical harmonics, and R_0 and the a's are parameters. The volume of this shape is constrained to be $4\pi R_0^3/3$; this fixes a_{00}. The $\lambda = 1$ terms correspond to translations of the center of mass, and can be ignored. It is often sufficient to neglect all terms with $\lambda > 2$. In the body-fixed frame in which the coordinate axes coincide with the principal axes of the shape, $a_{21} = a_{2-1} = 0$, and $a_{22} = a_{2-2}$, leaving only two free parameters. The parameter a_{20} describes axially-symmetric deformations, while a_{22} describes non-axially-symmetric deformations. If both are zero, the nucleus is spherical.

This thesis employs the Hill-Wheeler coordinates (β, γ)[Hil53], a polar-coordinate version of the (a_{20}, a_{22}) pair which are defined through

$$a_{20} = \beta\cos\gamma \tag{1.10}$$

$$a_{22} = \frac{1}{\sqrt{2}}\beta\sin\gamma. \tag{1.11}$$

In these coordinates, β (also called β_2 in this thesis) describes the "magnitude" of the deformation, and γ describes what non-spherical shape the nucleus possesses. A prolate (cigar) shape has $\gamma = 0°$, while an oblate (pancake) shape has $\gamma = 60°$. The nuclei described in this thesis have γ's no larger than a few degrees, making them mostly prolate, with a hint of triaxiality[†]. They have β's near 0.6, corresponding to major-to-minor axis ratios slightly smaller than 2:1.

A next-order approximation is to include the Y_{40} term. The coefficient of this term, a_{40}, is generally called β_4 and rarely gets larger than 0.1. The hexadecapole deformations considered later in this thesis may be related to the Y_{44} term. However, non-axial terms, including this one, are often ignored in the standard calculations.

A convention exists in labelling the axes of a prolate nucleus. In the body-fixed frame, the axes are labelled (1, 2, 3) with the long axis called the 3-axis. The

[†]A triaxial shape is an ellipsoid with no two axes equal, like a kiwi.

collective angular momentum is perpendicular to this, generally taken to be along the 1-axis. In the lab frame, the axes are labelled (x, y, z) and the x-axis coincides with the body-fixed 1-axis.

1.2 Superdeformation: Physics in the Second Well

In Section 1.1.1, the spherical shell gaps in Figure 1.1 were discussed. There are also many gaps at non-zero deformations, suggesting that deformed configurations are also stable for some neutron numbers. It turns out that many of these deformed configurations are at high excitation energies at low spin, but that they can become energetically favoured at high spin. The configurations of particular interest in this work are those with deformations $\beta \sim 0.6$, the superdeformed configurations.

1.2.1 Superdeformed Fission Isomers

The first superdeformed nuclei observed were the superdeformed fission isomers[§] in the actinide region [Pol62]. These excited nuclear states, first produced in reactions of ^{16}O and ^{22}Ne on ^{238}U, were observed to spontaneously fission with lifetimes as many as 30 orders of magnitude shorter than observed for the ground states of the same nuclei. Experiments have revealed dozens of these isomers in the actinide region [Sin96].

Nuclear theories prior to 1966 could not explain these tremendously short half-lives. If one assumes the nucleus can be modelled as a charged liquid drop, neglecting the shell effects discussed above, then the potential energy of the nucleus as a function of deformation appears like the dashed line in Figure 1.2. That is, there is a minimum at zero deformation and for infinite deformation (a fissioned system).

[§]An isomer is a long-lived excited nuclear state. Although the focus here is on the short fission lifetime of these particular states, the lifetime is still tens of microseconds, making it a million times longer than is typical of most nuclear excited states.

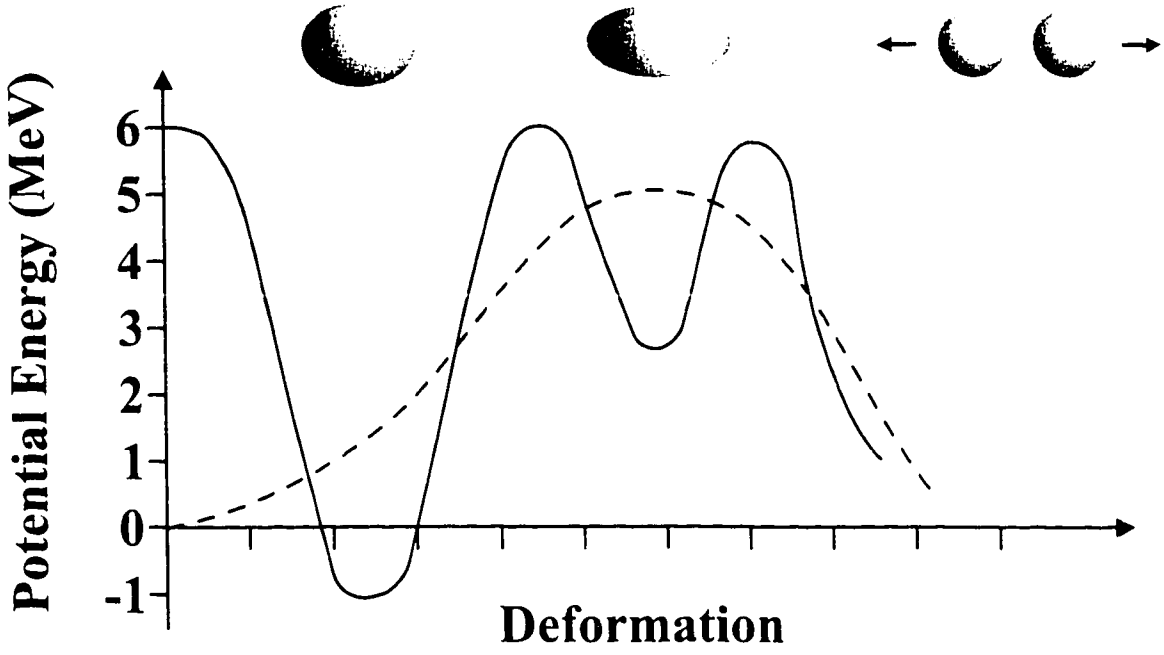

Figure 1.2: Schematic fission barrier with and without shell corrections. The dashed line shows the potential energy of the nucleus as a function of deformation, using only the liquid-drop model. The solid line shows the same, but including shell effects.

To fission, the nucleus has to tunnel through a wide barrier, giving rise to long fission lifetimes.

Strutinsky realized, however, that the shell effects described in the previous section would affect the stability of these liquid-drop shapes [Str67]. He invented the so-called "Strutinsky Prescription" to apply shell corrections to liquid-drop energies. When he and others [Tsa70] did this, they found a potential energy curve like the solid line in Figure 1.2. The appearance of the second well provided the solution to the fission isomer mystery. When excited to energies above that of the superdeformed minimum (which could happen in the reactions studies), the nucleus could first tunnel from the near-spherical minimum to the superdeformed minimum, and then tunnel into a fissioned system. Because the barriers are so much narrower in this case, the

tunnelling probability is much larger, and the lifetime much shorter.

1.2.2 Intruders

Consider the $g_{9/2}$ orbitals in Figure 1.1. The ones whose energy decreases most rapidly with deformation have small j projections on the nuclear symmetry axis, and thus have large projections on the collective angular momentum axis (relative to the nearby orbitals). Because of their energy dependence on deformation, they are called "deformation-driving", and are said to stabilize the superdeformed shapes for nuclei with proton and neutron numbers near 30-32. They have considerable influence on the properties of $A \sim 60$ superdeformed nuclei, such as their moments of inertia and deformations.

All major shells contain an analogous orbital with parity differing from the rest of the shell. These $h_{11/2}$, $i_{13/2}$, $j_{15/2}$, ... orbitals are called intruders or intruder orbitals. A few of these orbitals are near the Fermi surface in all of the superdeformed mass regions, and in all cases, they have considerable influence over the properties of the superdeformed bands, just as in the $A \sim 60$ case. They are so important that superdeformed band configurations are often specified by stating only the occupation of intruder orbitals, as described in the following section.

1.3 The Mass-150 Region

The superdeformed nuclei described in this thesis are in the $A \sim 150$ region. This region of superdeformation was discovered not by observing a fissioning band-head, as in the actinide region, but by identifying a cascade of γ rays de-exciting a superdeformed rotational band in ^{152}Dy. The first evidence of such a cascade came in 1984 [Nya84], with a discrete set of γ rays reported in 1986 [Twi86]. The properties

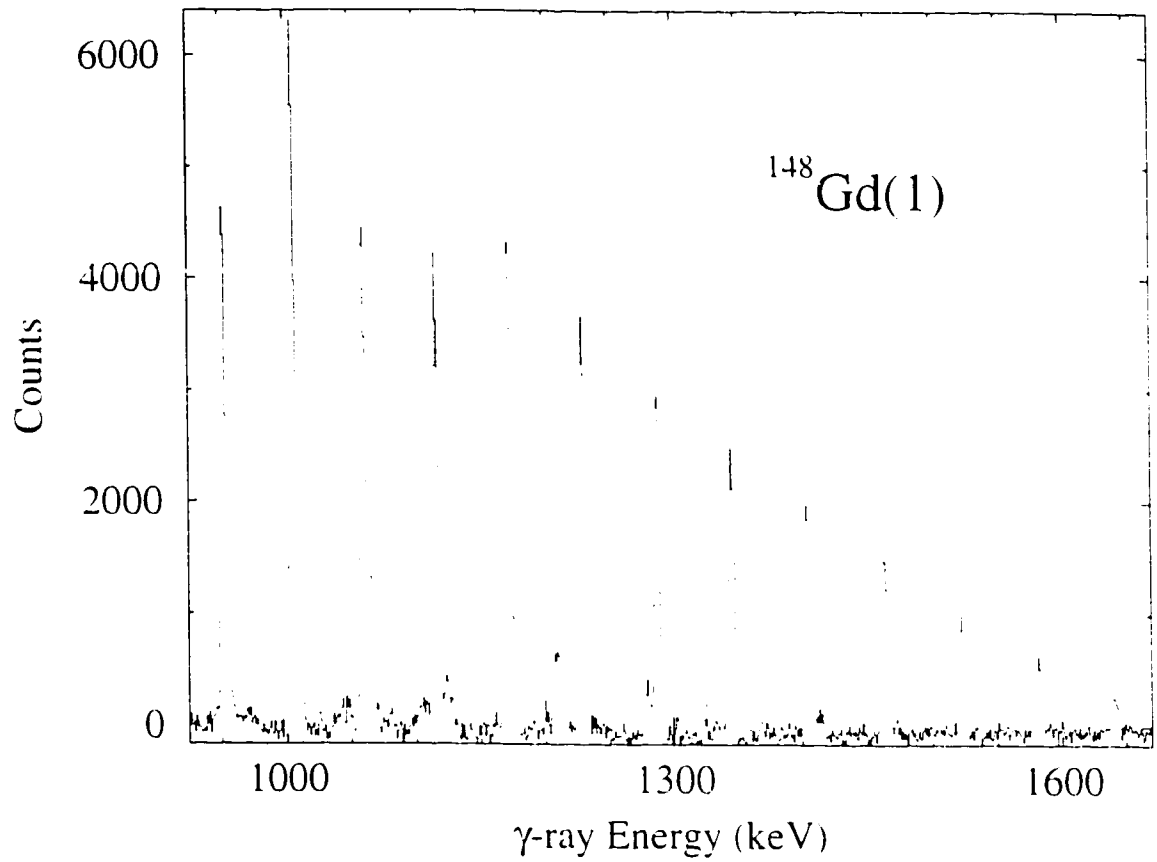

Figure 1.3: Partial γ-ray spectrum of a typical superdeformed band in the $A \sim 150$ region. The band is in ^{148}Gd and is the first of many such structures observed in this nucleus (hence the "(1)").

of superdeformed bands in this region are summarized below.

As discussed in Section 1.1.2, the states in a superdeformed rotational band have angular momenta I, $I+2$, $I+4$, ..., connected by γ rays. Equation 1.3 showed that, as long as the moment of inertia remains constant, the energies of the γ rays are proportional to I, so that the spectrum of γ ray energies should look like a row of fenceposts, as in Figure 1.3. Bands in this mass region typically have 15-20 transitions, giving them a very distinctive signature. It should be noted that

$A \sim 150$ superdeformed bands are never populated with more than two percent of the intensity of the channel, making them impossible to see without using a number of clever experimental techniques. These techniques are discussed in Chapter 3.

Most of the superdeformed nuclei in this mass region have several known superdeformed bands, based on different single-particle configurations. In this thesis, superdeformed bands are labelled by their nucleus, and a number in parentheses, like ^{148}Eu(2). This number is just a label and need not have any other significance, although bands are often numbered in order of decreasing intensity. Band 1 is almost always the most intense, implying that its excitation energy is the lowest of the superdeformed bands. This band is called yrast, a Swedish word meaning "dizziest". Yrast states have the largest angular momentum for a given excitation energy, or equivalently, the smallest excitation energy for a given angular momentum.

Important properties of these superdeformed levels include their spins, parities, and excitation energies. Because the $A \sim 150$ bands are produced in heavy-ion fusion reactions (discussed in Chapter 3), the only way one could know these quantities is by observing the decay of the bands into the well-established energy levels of these nuclei (sometimes called normal-deformed levels). By measuring the character of the γ rays that connect the superdeformed band with other nuclear states, one could infer all of these properties of the superdeformed levels. However, the decay out of these bands goes along many different routes, with no route intense enough to have yet been observed. Thus, until better data are available, the quantum numbers of these bands must be estimated.

The $A \sim 150$ bands are stabilized by the proton shell gaps at 62 66 and the neutron shell gaps at 84-86 (see Figure 1.1). The intruder orbitals stabilizing these gaps are the proton $i_{13/2}$ and the neutron $j_{15/2}$ orbitals with Nilsson numbers $N = 6$

and $\bar{7}$, respectively. As discussed in the previous section, the properties of $A \sim 150$ superdeformed bands are determined to a large extent by the occupation of their intruder orbitals. As a result, configuration assignments in these nuclei begin, and sometimes end with the intruder configurations.

Rather than label the $N = 6$ proton intruders by their full Nilsson labels, they are labelled $\bar{6}_1$, $\bar{6}_2$, ..., in order of excitation energy. A band with the first m proton intruders filled is said to have a $\pi 6^m$ configuration (note the superscript). Similarly, the $N = 7$ neutron intruders are labelled $\bar{7}_1$, $\bar{7}_2$, ..., and a band with the first n neutron intruders filled has a $\nu 7^n$ configuration. Band 1 in $^{152}_{66}\mathrm{Dy}_{86}$ has an intruder configuration of $\pi 6^4 \nu 7^2$, while $^{149}_{64}\mathrm{Gd}_{85}$(1) has an intruder configuration of $\pi 6^2 \nu 7^1$. This notation will be used frequently in this thesis.

This chapter has provided a whirlwind introduction to nuclear structure physics, culminating in a discussion of $A \sim 150$ superdeformation. The next chapter continues the theoretical discussion, pursuing topics important to the study of superdeformation in this thesis.

Chapter 2

Theory of Superdeformed Bands

This chapter supplies the theoretical background necessary to understand fully the chapters that follow. The first three sections describe areas of importance in many sub-fields of nuclear physics; the last two sections describe specific phenomena studied in this work.

2.1 The Particle-Rotor Model

The particle-rotor model [Boh53] employs a relatively simple Hamiltonian to describe the interaction between the single-particle and collective degrees of freedom. It is widely used, and some of its results will be used later in this work.

In the particle-rotor model, one imagines that the nucleus can be treated as a few particles coupled to a deformed core. The Hamiltonian H for this system is made up of a collective part $H_{\rm coll}$, attributed to the core, and a single-particle part ϵ, given by the energy of the particles outside the core (in the field of the deformed core):

$$H = H_{\rm coll} + \epsilon \tag{2.1}$$

The collective energy is given by the classical expression

$$H_{\rm coll} = \frac{\hbar^2}{2}\left(\frac{R_1^2}{\mathcal{J}_1} + \frac{R_2^2}{\mathcal{J}_2} + \frac{R_3^2}{\mathcal{J}_3}\right) \tag{2.2}$$

where the R_i are the components of the core angular momentum along the body-fixed axes, and the $\mathcal{J}_i$ are the principal moments of inertia.

The total angular momentum of the nucleus, I, is made up of the core angular momentum R and the single-particle contribution j. Thus, each of the components satisfies the equation

$$I_i = R_i + j_i \tag{2.3}$$

and the collective Hamiltonian may be re-written as

$$H_{\rm coll} = \frac{\hbar^2}{2}\left(\sum_{i=1}^{3}\frac{I_i^2}{\mathcal{J}_i} + \sum_{i=1}^{3}\frac{j_i^2}{\mathcal{J}_i} - \sum_{i=1}^{3}\frac{2I_ij_i}{\mathcal{J}_i}\right). \tag{2.4}$$

These three terms are called the rotational term, the recoil term, and the Coriolis term, respectively.

To a good approximation, one may assume that the nuclei of interest are axially symmetric about the 3-axis. This means that $\mathcal{J}_1 = \mathcal{J}_2$, and that $R_3 = 0$ (so $I_3 = j_3$). In this limit, the collective Hamiltonian becomes

$$H_{\rm coll} = \frac{\hbar^2}{2\mathcal{J}}\left(\sum_{i=1}^{2} I_i^2 + \sum_{i=1}^{2} j_i^2 - \sum_{i=1}^{2} 2I_ij_i\right). \tag{2.5}$$

where $\mathcal{J} = \mathcal{J}_1$. At this point, one can exploit the fact that $I_1^2 + I_2^2 = I^2 - I_3^2$, with a similar equation for j. Also, one should remember that the eigenvalue of I^2 is $I(I+1)$ (and similarly for j) and that $I_3 = j_3$. The equation may thus be rewritten as

$$H_{\rm coll} = \frac{\hbar^2}{2\mathcal{J}}\left(I(I+1) - 2I_3^2 + j(j+1) - 2(I_1j_1 + I_2j_2)\right). \tag{2.6}$$

Since the recoil term depends only on the valence particles, it is often absorbed into ϵ. This means that the total Hamiltonian can be written as

$$H = \frac{\hbar^2}{2\mathcal{J}}\left(I(I+1) - 2I_3^2 - 2(I_1j_1 + I_2j_2)\right) + \epsilon. \tag{2.7}$$

The nuclei of interest in this thesis have large deformations. In this case, and when the valence particles have small values of j_1, the so-called strong coupling limit is applicable. In this limit, the Coriolis matrix elements (which connect states differing in I_3 by 1) are small compared to the level splitting and can be neglected for all states with $I_3 \neq 1/2$. Thus, the Hamiltonian can be written as

$$H = \frac{\hbar^2}{2\mathcal{J}}(I(I+1) - 2I_3^2) + \epsilon. \tag{2.8}$$

For the $I_3 = 1/2$ case, the Coriolis term causes the $I_3 = 1/2$ states to mix with $I_3 = -1/2$ states (that is, themselves) and cannot be ignored. In this limit, it can be shown that the energies of the states are given by [Rin80]

$$E = \frac{\hbar^2}{2\mathcal{J}}(I(I+1) - \frac{1}{4} + a(I+\frac{1}{2})(-1)^{I+1/2}) \tag{2.9}$$

where a is called the decoupling parameter, and is given by the expectation value of $ij_+e^{-i\pi j_1}$. This expression neglects the single-particle component.

In the case where j_1 is larger, the Coriolis term becomes more important. In this limit, the Hamiltonian strongly favours states in which j is aligned closely with the x-axis. The deformation-driving intruder orbitals are highly aligned with the rotation axis for this reason.

2.2 Alignments

As described above, superdeformed nuclei may be treated as deformed rotating cores coupled to a few particles. Thus, it is often possible to understand the properties of a given superdeformed band relative to another band in a neighbouring nucleus by considering only the properties of those particles which make the structures of the two bands different. One of those single-particle properties that is most important is the effective alignment Δi_x. This section defines the effective alignment, describes why

it is an important quantity for nuclear physicists, and introduces the closely related quantity, the incremental alignment $\Delta i_{\rm inc}$.

2.2.1 Effective Alignment

The γ-ray spectrum of a rotational band is uniquely defined by a plot of its angular momentum I versus its rotational frequency ω. Thus, given the spectrum of one band, the transition energies of a second band can be determined if one knows the difference between their respective I versus ω graphs. This quantity, the difference in angular momentum between two bands as a function of frequency, is defined as the effective alignment $\Delta i_x(\omega)$ (see Figure 2.1).

The effective alignment has a simple interpretation in terms of single-particle properties as well. In a high-spin nucleus, where I is predominantly along the axis of collective rotation (the x-axis), I is approximately equal to I_x. Since I_x is made up from the contributions of the A nucleons in the nucleus,

$$I_x = \sum_{i=1}^{A} \langle j_x^{(i)} \rangle \tag{2.10}$$

where $\langle j_x^{(i)} \rangle$ is the expectation value of the x-component of the angular momentum of the ith nucleon. If the quantity $\langle j_x^{(i)} \rangle$ changes very little in going from a band in a mass-A nucleus to a neighbouring mass-$(A+1)$ nucleus*, then the effective alignment is given by

$$\begin{aligned} \Delta i_x(\omega) &= I^{A+1}(\omega) - I^{A}(\omega) && (2.11)\\ &\simeq I_x^{A+1}(\omega) - I_x^{A}(\omega) && (2.12)\\ &= \sum_{i=1}^{A+1} \langle j_x^{(i)} \rangle - \sum_{i=1}^{A} \langle j_x^{(i)} \rangle && (2.13) \end{aligned}$$

*This assumption that $\langle j_x^{(i)} \rangle$ is insensitive to the nucleus is a particularly good one when the mass-A nucleus is a rigid core, like ^{152}Dy. However, it is found that this assumption remains good throughout the $A \sim 150$ superdeformed nuclei, where most of the nucleons can still be assumed to be involved in rotation of the core.

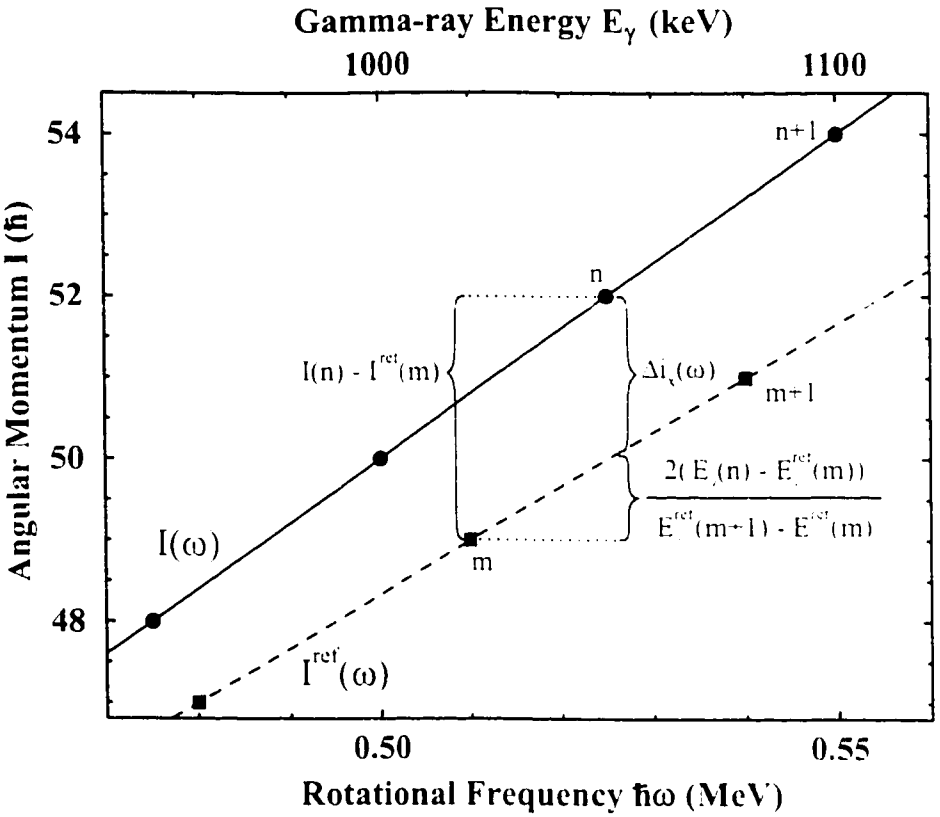

Figure 2.1: Schematic diagram defining the effective alignment. The individual terms from Equation 2.15 are also illustrated.

$$= \langle J_x^{(A+1)} \rangle. \tag{2.14}$$

Thus, Δi_x is approximately equal to the aligned spin of the last nucleon. More generally, Δi_x for two bands is a measure of the sum of the aligned spins of the nucleons which make the structures of the two bands different.

Calculating experimental effective alignments is simple. Consider a reference band whose mth transition energy is $E_\gamma^{\rm ref}(m)$. Consider also another band with transition energies $E_\gamma(n)$. The effective alignment of the second band with respect

to the reference is given by

$$\Delta i_x(E_\gamma(n)) = (I(n) - I^{\rm ref}(m)) - 2\hbar \frac{E_\gamma(n) - E_\gamma^{\rm ref}(m)}{E_\gamma^{\rm ref}(m+1) - E_\gamma^{\rm ref}(m)} \tag{2.15}$$

where $I^{\rm ref}(m)$ is the spin of the level fed by $E_\gamma^{\rm ref}(m)$, and $I(n)$ is spin of the level fed by $E_\gamma(n)$. The first term is the difference in spins of corresponding levels. The second term is an interpolation necessary because pairs of bands have, in general, different γ-ray energies and so a direct comparison at a given rotational frequency is not possible.

Effective alignments are commonly used in the $A \sim 150$ region to assign single-particle configurations to superdeformed bands. It has been shown that the effective alignment of a given orbital is relatively constant over the entire mass region, and that the effective alignment of bands differing by two nucleons is given by the sums of the effective alignments of the two nucleons added individually [Rag91]. This property is called additivity.

2.2.2 Incremental Alignment

The incremental alignment is defined by Stephens [Ste90] as

$$\Delta i_{\rm inc} = 2\hbar \frac{E_\gamma(n) - E_\gamma^{\rm ref}(m)}{E_\gamma^{\rm ref}(m+1) - E_\gamma^{\rm ref}(m)} \tag{2.16}$$

where the notation is the same as in the previous section. The reader will recognize this as the negative of the second term in the effective alignment. The incremental alignment thus ignores the contribution to the effective alignment coming from the difference in spins of the emitting levels, and retains the "interpolated alignment" coming from the difference in γ-ray energies.

Although the incremental alignment has no convenient physical interpretation, as does the effective alignment, it is easy to calculate and finds common use

in nuclear structure studies. Superdeformed bands obey additivity rules for the incremental alignment just as for the effective alignment (as they must, since the $(I(n) - I^{\rm ref}(m))$ terms cancel one another). The incremental alignment is, therefore, just as useful in assigning single-particle configurations. In addition, since the spins of many SD bands are not known, using the incremental alignment avoids the problem of having to guess the spins of the emitting levels.

2.3 Routhian Diagrams

As discussed above, the relative properties of different superdeformed bands are determined by the behaviour of the nucleon orbitals at the Fermi surface. Thus, theoretical predictions of the properties of these orbitals can be useful to experimentalists in assigning single-particle configurations to superdeformed bands. This section examines some of the simplest theoretical predictions that can be made.

The behaviour of a nucleon is a function of the nuclear angular momentum, since it is in a rotating system and so, classically speaking, it is subject to Coriolis and other non-inertial forces. One is therefore interested in knowing what the single particles are doing as a function of angular momentum, or equivalently, rotational frequency. This information is provided in a Routhian diagram.

The Routhian operator $\mathcal{R}$ is defined as the Hamiltonian in the rotating frame of the nucleus. It is thus related to the Hamiltonian in the lab frame, H, by the canonical transformation $\mathcal{R} = H - \vec{\omega} \cdot \vec{J}$. For a single particle the expectation value of the Routhian operator (often called the Routhian), e', is given by

$$e' = e - \omega j_x \tag{2.17}$$

where e is the single-particle energy at $\omega = 0$, and j_x is the component of its angular momentum along the collective rotation axis of the nucleus. A Routhian diagram is

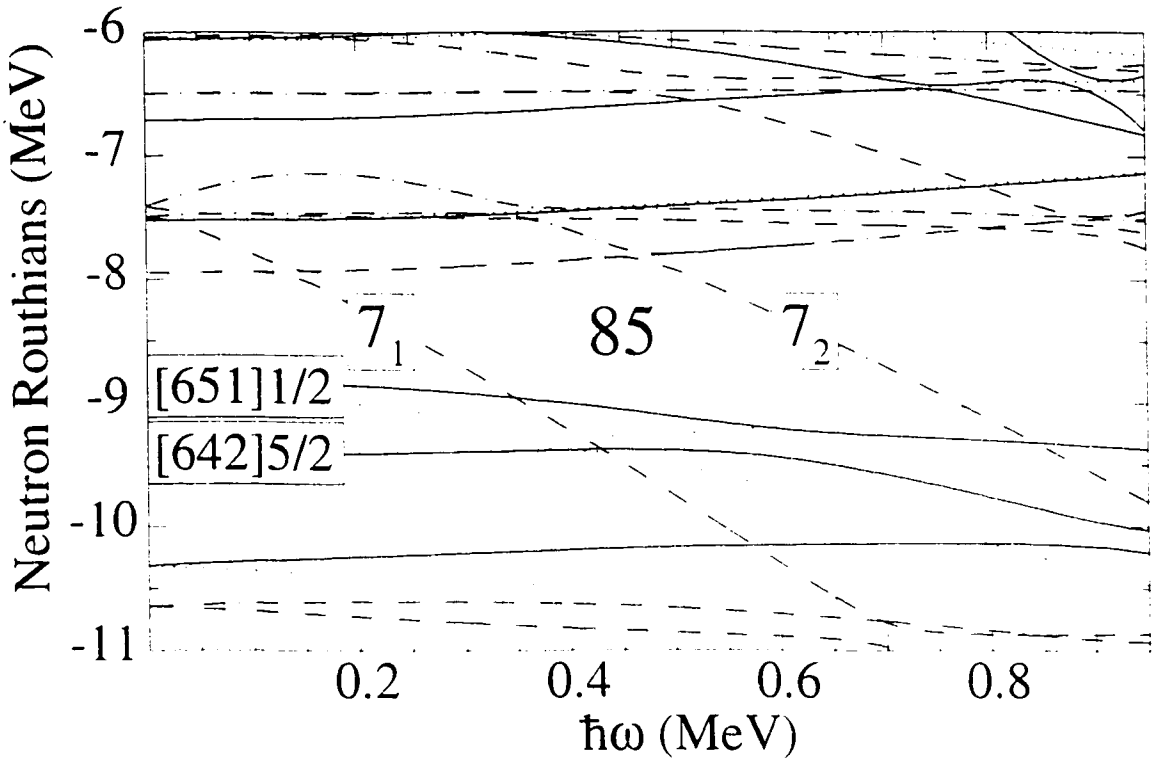

Figure 2.2: Representative Routhian diagram for neutrons near $N = 85$ (N is the neutron number; Z is the proton number). Some of the intruder orbitals are labelled. The Nilsson numbers of some others are also shown.

a plot of e' as a function of frequency.

A representative Routhian diagram is shown in Figure 2.2. Each line is the Routhian of a different orbital, with the line types indicating the signature, α, and parity, π, of the orbital (to be defined). The label "85" means that 85 orbitals lie below that gap.

According to Equation 2.17, the slope of a Routhian is equal to the negative of the aligned spin j_x of that orbital. The orbitals labelled "7_1" and "7_2" have large slopes and are thus highly aligned. These are the $N = 7$ intruder orbitals, which help stabilize the superdeformed shapes in the $A \sim 150$ region.

Routhians with constant slopes are of special interest. These orbitals have constant alignments as a function of rotational frequency, which is a necessary (but not sufficient) condition for the generation of identical bands, as discussed in the following section.

Routhians with non-constant slopes are also of interest, especially those that quickly change their slopes, like the orbitals labelled with the Nilsson numbers [651]1/2 and [642]5/2. The dotted orbitals, for instance, interact at $\hbar\omega = 0.4$ MeV, undergoing a quantum mechanical level repulsion. If a superdeformed band has only one of these orbitals filled, then this interaction (or crossing) is said to be unblocked and its effect can be seen in deviations from an otherwise smoothly varying moment of inertia.

The orbitals are labelled by their parity and signature, the only two good quantum numbers left to orbitals in a rotating nucleus. Parity is a commonly-used symmetry quantum number which describes whether the wave function is even (positive parity) or odd (negative parity) under reflection through the origin. The signature is given by j_x mod 2. The astute reader will notice that the orbitals in this diagram have non-constant slopes and so cannot possibly have constant signature (recall that the slope is $-j_x$). This is an example of the contradiction between the quantum and semi-classical treatments of the nucleus. It is, strictly speaking, incorrect to treat ω as a continuous variable, so the smoothly-varying curves in the Routhian diagram should not be taken as absolute truths. However, the predictions of this semi-classical description with respect to alignments and crossing frequencies are still good.

2.4 Identical Bands

Consider two superdeformed bands in neighbouring nuclei in the $A \sim 150$ region. Since the masses of the nuclei differ by one part in 150, and since the moment of

inertia scales like $A^{5/3}$, one should expect the moments of inertia of these two nuclei to differ by approximately one percent. Since γ-ray energies are inversely proportional to the moment of inertia, one may expect one percent shifts in gamma-ray energies between these two bands, and since the γ-ray energies are approximately 1000 keV, these shifts should be around 10 keV. The superdeformed bands in neighbouring nuclei should, therefore, bear little resemblance to one another.

This expectation is fulfilled in most pairs of bands in neighbouring nuclei. A typical pair is shown in the top two spectra of Figure 2.3. However, the top and bottom spectra in this Figure are highly correlated. This pair of bands is an example of what are called identical bands.

Identical bands were first observed in 1990 by Byrski *et al.* [Byr90], in the bands ^{150}Gd(2) and ^{151}Tb(2) (identical to ^{151}Tb(1) and ^{152}Dy(1), respectively). Since that discovery, tens of examples of superdeformed identical bands have been found in most of the superdeformed mass regions [Bak95]. It should be noted that not all of these identical bands are as identical as those shown in Figure 2.3. The ones in Figure 2.3, and the ones seen by Byrski *et al.*, belong to a subset of the identical bands called isospectral identical bands, meaning that they have the same transition energies. The more general class of identical bands do not have the same transition energies, but do have identical dynamical moments of inertia.

Since the γ-ray energies of isospectral bands are the same, their relative incremental alignments are zero, and their relative effective alignments are a constant, the spin difference of the levels de-excited by the identical γ rays. More generally, bands with identical moments of inertia have constant incremental and effective alignments. Plots of these alignments are often used in the nuclear physics literature to demonstrate that two bands are identical.

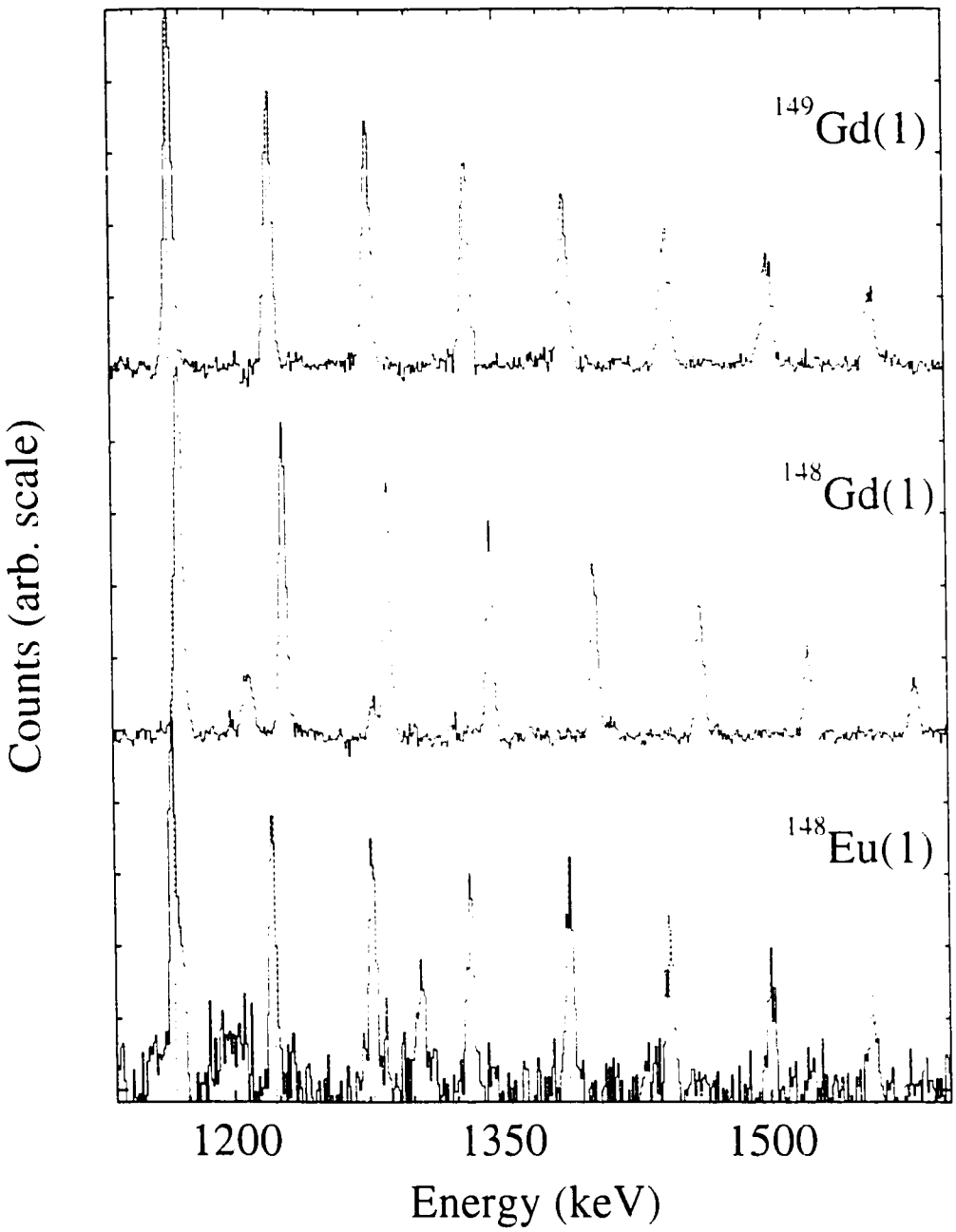

Figure 2.3: Examples of identical and non-identical bands. The uppermost spectrum is that of the SD band ^{149}Gd(1) [Fli97], the middle one ^{148}Gd(1), and the bottom spectrum ^{148}Eu(1). It is clear how little correlation there is between the top two spectra, but how much there is between the top and bottom spectra.

The identical bands ^{151}Tb(2) and ^{152}Dy(1) differ in structure by a single particle, a proton in the negative-signature [301]1/2 Nilsson orbital. This is also true of the identical pair ^{150}Gd(2) and ^{151}Tb(1), and of other SD bands in the $A \sim 150$ mass region. It thus appears that there is something special about this orbital that makes it responsible for the generation of identical bands. The same appears to be true of the positive-signature [411]1/2 neutron orbital, although the experimental evidence for this is not as abundant.

2.4.1 Theoretical Explanations

Several attempts have been made to explain the identical bands phenomenon, but only the two best-known explanations will be discussed here.

The first explanation, proposed by Ragnarsson [Rag90, Rag93], is that the similarity between the γ-ray energies in the two bands is essentially accidental. He has presented some evidence that the effective alignment of the negative-signature [301]1/2 proton orbital (which must be $-1/2$ to generate isospectral bands) can be reproduced in his cranked Nilsson-Strutinsky calculations. In this model, the removal of this proton from the nucleus causes a decrease in nuclear mass, and an increase in nuclear deformation; these two effects cancel one another, making the moments of inertia identical in the two cases.

This approach is somewhat unsatisfying, in that it takes what appears to be an incredible, cross-nucleus degeneracy, and relegates it to the status of a coincidence. Another problem is that the calculations of Ragnarsson [Rag93] reproduce the observed $-1/2$ alignment to no better than twenty percent. Thus, many people have sought alternate explanations.

A very attractive option invokes the concept of pseudospin. The notion of pseudospin [Hec69, Ari69] arises from the observation that as the deformation be-

comes large, orbitals in a given oscillator shell with quantum numbers $(l, j = l + 1/2)$ and $(l+2, l+3/2)$ approach one another. It has been found convenient to relabel these orbitals with pseudo-orbital angular momentum $\tilde{l}$ and pseudo-spin $\tilde{s}$, so that these orbitals form the pseudo-spin doublet $(\tilde{l} = l + 1, j = \tilde{l} \pm 1/2)$ with small pseudo-spin-orbit coupling. This trick of changing the l-value in order to decrease the spin-orbit splitting tends to work because the nuclear Hamiltonian depends mostly on j, and is almost independent of l.

The band ^{151}Tb(2) has an angular momentum projection along its symmetry axis of $I_3 = 1/2$, and in the strong-coupling limit its γ-ray energies are given by [Rin80]

$$E_\gamma(I) = \frac{\hbar^2}{\mathcal{J}}(2I - 1 + (-1)^{I+1/2}a) \tag{2.18}$$

where a, the decoupling parameter, is given by $(-1)^N \delta_{\Lambda 0}$, where N and Λ are the Nilsson numbers of the missing proton. For the $\pi[301]1/2$ orbitals, $\Lambda = 1$ so $a = 0$, and the γ-ray energies are unperturbed from a rigid-rotor sequence. No identical band is expected.

When described in a pseudo-spin framework, however, the identical band phenomenon arises naturally. In this model, one uses the pseudo-Nilsson quantum numbers for the orbital, $\tilde{N} = 2$ and $\tilde{\Lambda} = 0$. This makes $a = 1$, and since the spins of the band have even $I + 1/2$, the γ-ray energies are given by

$$E_\gamma(I) = \frac{\hbar^2}{\mathcal{J}}(2I - 1 + 1) \tag{2.19}$$

$$= \frac{\hbar^2}{\mathcal{J}}(2(I + 1/2) - 1). \tag{2.20}$$

That is, the energies are the same as those in ^{152}Dy(1) (which has spins $I + 1/2$). Thus, ^{151}Tb(2) should be identical to ^{152}Dy(1) in the limit that the deformations are large. By the same reasoning, the neutron orbital with Nilsson numbers [411]1/2 and pseudo-Nilsson numbers $[\tilde{3}\tilde{1}\tilde{0}]1/2$ should also generate identical bands.

This is an intriguing theory, but it has a major flaw which was glossed over in the above discussion. This flaw is that the theory ignores the differences in moment of inertia between the two nuclei. The pseudospin model can shed no light on this aspect of the phenomenon, and therefore remains incomplete.

2.5 $\Delta I = 4$ Bifurcation

The observation of the effect known as $\Delta I = 4$ bifurcation was one of the most remarkable developments in the recent history of nuclear structure. The following sections describe this phenomenon and some of the theoretical attempts to explain it.

2.5.1 Experimental Evidence

In 1993, Flibotte *et al.* [Fli93] presented evidence for an unexpected anomaly (called $\Delta I = 4$ bifurcation, or staggering) in the dynamic moment of inertia of the yrast SD band of ^{149}Gd. This moment of inertia, plotted in Figure 2.4 is not a smooth function of rotational frequency, but exhibits a regular "zig-zag" behaviour. The details of this unusual oscillation can best be seen in a "staggering plot", the construction of which is explained below.

Since the dynamic moment of inertia is given by the reciprocal of ΔE_γ, one can also see the staggering effect in a plot of ΔE_γ, shown in the upper panel of Figure 2.5. Since one is interested not in the gross characteristics of this graph, but rather in the subtle deviations from its mean behaviour, a smooth reference curve $\Delta E_\gamma^{\mathrm{ref}}$ is constructed from the data, also shown in the upper panel of Figure 2.5. For the smooth reference, the well-known four-point smoothing formula [Bev92] is used:

$$\Delta E_\gamma^{\mathrm{ref}}(I) = \frac{1}{4}\left(\Delta E_\gamma(I+2) + 2\Delta E_\gamma(I) + \Delta E_\gamma(I-2)\right). \qquad (2.21)$$

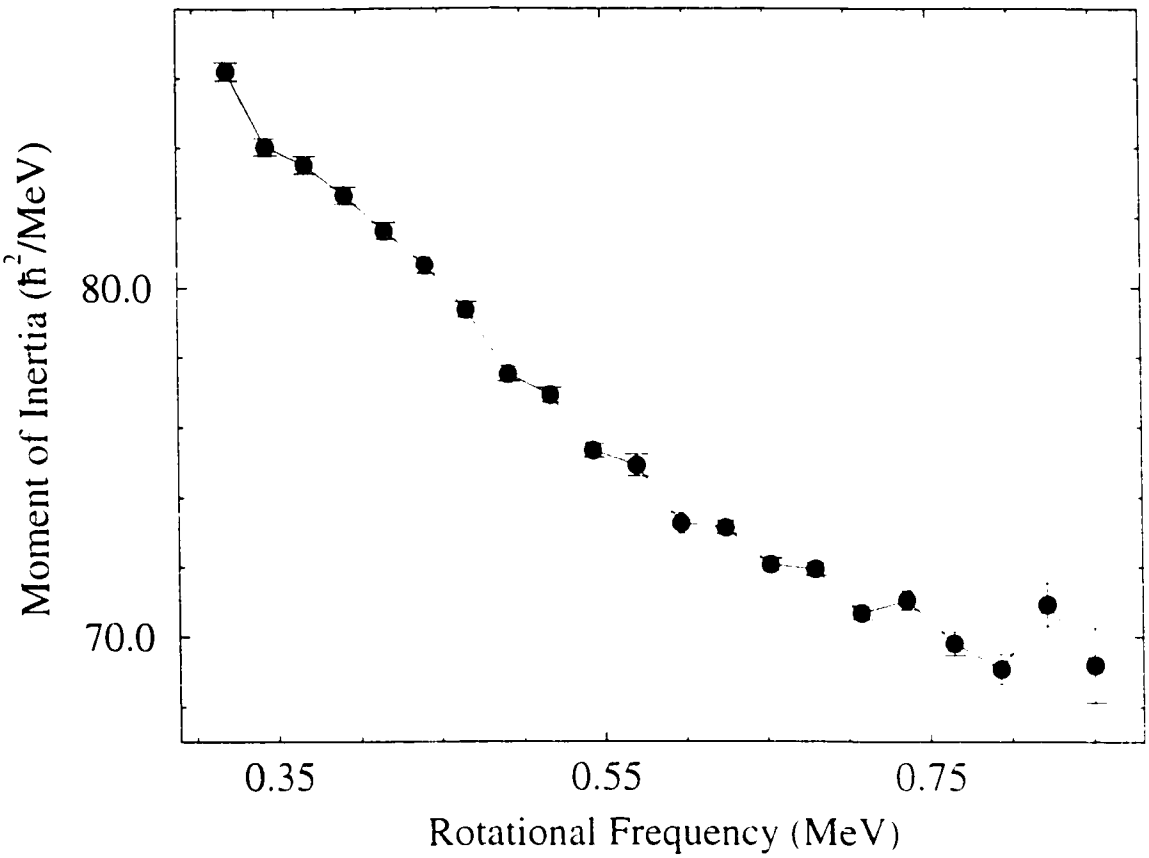

Figure 2.4: Dynamic moment of inertia of the yrast band of ^{149}Gd. Note how the data exhibit an oscillation about their mean behaviour.

One then subtracts from each data point the value of the smooth reference at the same rotational frequency. This gives a staggering plot, shown in the lower panel of Figure 2.5.

This staggering in ΔE_γ indicates that the sequence of levels in the superdeformed band has been separated into two sequences (the sequence has "bifurcated"), one with spins $(I, I+4, I+8, \ldots)$, shifted slightly in energy with respect to the other, with spins $(I+2, I+6, I+10, \ldots)$. Since the magnitude of the staggering in ΔE_γ is approximately 240 eV at the mid-point of the staggering pattern, the relative shift

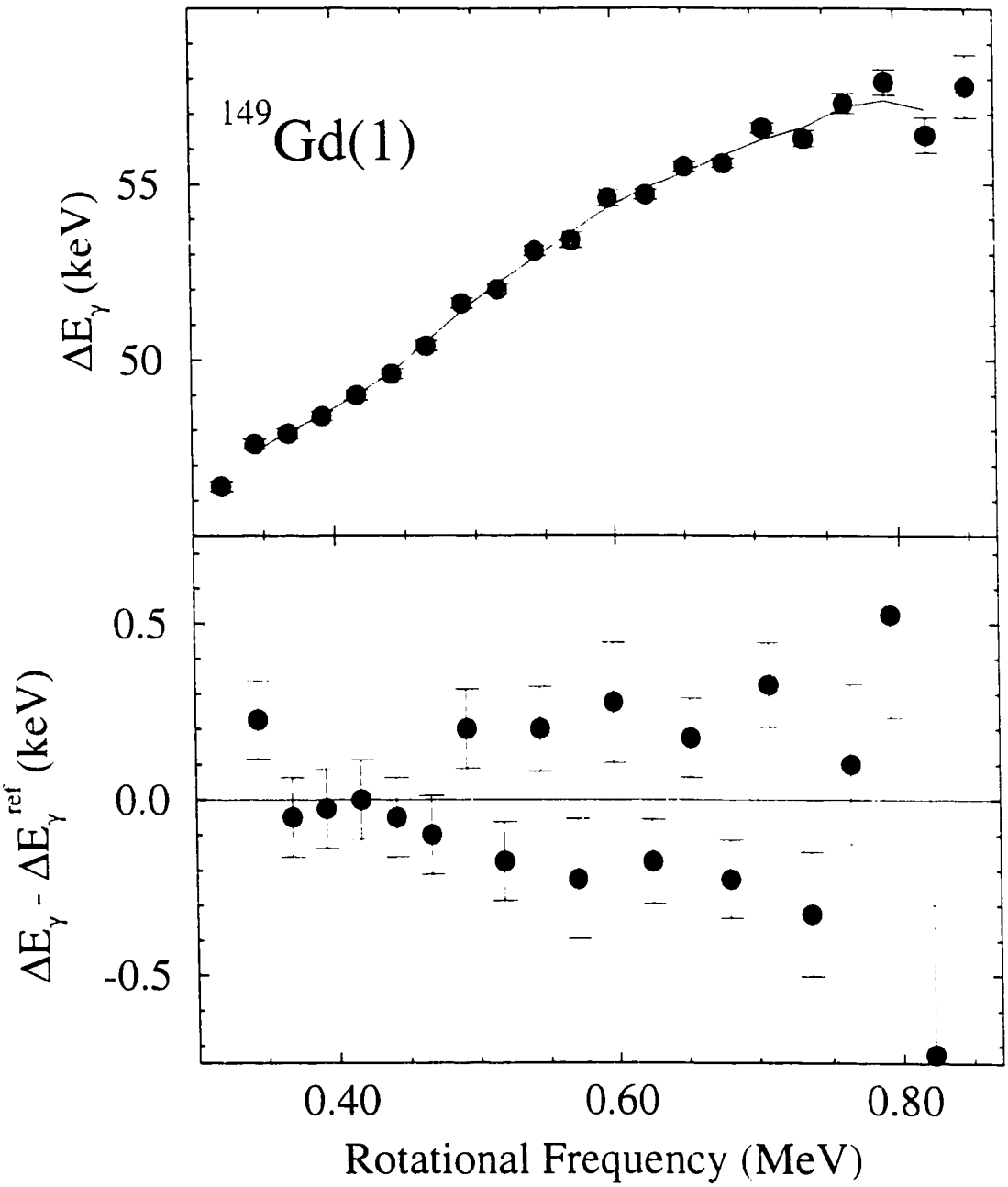

Figure 2.5: Construction of a staggering plot. In the upper panel, the points represent the ΔE_γ values for ^{149}Gd(1); the solid line is obtained by applying a four-point smoothing formula to the data. In the lower panel is the difference between the data and the smooth curve. The staggering effect is clearly seen.

of the energy levels of the two sequences is only 60 eV. This is quite small, especially when one considers that the energy levels of interest are at excitation energies of about 20 MeV.

Some authors have suggested [Rev96, Don96] that the staggering effect is due to one or more band crossings. That is, levels from other SD configurations with the same spin and parity as the ^{149}Gd yrast band are mixed with those of the yrast band, producing level repulsion and thus staggering. While it is true that band crossings can produce irregular staggering effects over a relatively narrow spin region (as shown by Riley *et al.* [Ril96]), it is difficult to imagine a band crossing scenario capable of producing a staggering pattern as regular as that of ^{149}Gd(1) that persists over so many transitions.

2.5.2 Theoretical Efforts

There have been numerous attempts to explain the origin of $\Delta I = 4$ bifurcation [Ham94, Bur95, Mac95, Mag95, Mik95, Pav95, Sun95]. Many of these theories assert that the presence of two regular $\Delta I = 4$ sequences suggests an explanation involving a four-fold rotational symmetry (an invariance with respect to the C_4 point symmetry[†]). The best known such theory is that of Hamamoto and Mottelson [Ham94], the basics of which are described below. This approach is very similar to that proposed by Pavlichenkov and Flibotte [Pav95].

Hamamoto and Mottelson begin with a generic C_4-invariant Hamiltonian, which they suppose to be a perturbation to the conventional particle-rotor Hamiltonian:

$$H = AI_3^2 + B_1(I_1^2 - I_2^2)^2 + B_2(I_1^2 + I_2^2)^2, \tag{2.22}$$

[†]In general, a C_n symmetry is an invariance with respect to a rotation through $360/n$ degrees.

where I_i are the three components of the nuclear angular momentum I with the 3-axis coincident with the long axis of the prolate shape and the 1- and 2-axes lying in the equatorial plane. The quantities A, B_1, and B_2 are constants. The first term in this Hamiltonian serves to keep I away from the 3-axis, as expected for a superdeformed nucleus. The second term breaks the C_∞ symmetry of the Hamiltonian and is the simplest term (lowest power in I) which makes C_4 the dominant symmetry. The third term is axially symmetric, but is included so that all C_4-invariant terms of fourth order in I are present in the Hamiltonian. To some extent, it counteracts the first term (since $(I_1^2 + I_2^2)$ is proportional to $-I_3^2$), so it must be assumed that $2B_2I^2 < A$ so that the angular momentum lies in the equator. Some authors [Mac95] have shown that B_2 must be very small so that the regular rotational structure of the SD band is not destroyed. In this thesis, B_2 will be set to zero.

The Hamiltonian describes a potential energy surface with four minima in the equatorial plane. Quantum mechanics allows the angular momentum to tunnel from one of these minima to another, producing a level splitting which is proportional to the tunneling matrix element. It is shown in Appendix A that for $I^2 > A/4B_1$, the tunneling matrix element acquires a factor which changes sign when I changes by $2\hbar$. This produces an effect like that observed in ^{149}Gd(1).

This model is not without its critics. Dönau, Frauendorf, and Meng [Don96] have provided the most notable criticism, performing calculations to estimate the relative magnitudes of the parameters B_1 and A. Their calculations show that it is extremely unlikely that the C_∞ symmetry-breaking terms in the above Hamiltonian come from a static hexadecapole deformation of the superdeformed shape, as was suggested by Hamamoto and Mottelson. However, this does not negate the validity of the model; it only establishes that the appearance of C_4 terms in the Hamiltonian

is not the result of a static deformation.

Recently, Pavlichenkov has taken a new but related approach. He has considered [Pav97a] a Routhian consisting of single-particle energies, two-body quadrupole and hexadecapole interactions, and cranking terms for rotation about the axes perpendicular to the long axis of the nucleus. From this, he has derived an effective Hamiltonian

$$H = \frac{\hbar^2}{2\mathcal{J}} I(I+1) + \mathcal{B} I^2(I+1)^2 + d(I_+^2 + I_-^2) + c(I_+^4 + I_-^4), \qquad (2.23)$$

where $\mathcal{B}$, c, and d depend on the quadrupole and hexadecapole moment operators, and the corresponding deformations. This Hamiltonian produces a staggering effect when $c > 0$. He can, therefore, determine whether a given band will stagger by determining the sign of c, which is proportional to the multipole moment Q_{44} [Pav97b].

The moment Q_{44} is dominated by the contribution of high-j subshells that are less than half-filled, namely the $N = 6$ proton and $N = 7$ neutron intruder orbitals. Figure 2.6 shows Q_{44} for these subshells as a function of the number of particles in the shell, for three different rotational frequencies. Thus, one should be able to predict whether the band will stagger by finding the Q_{44}'s of the proton and neutron intruder configurations. For instance, the yrast band of ^{151}Dy has a $\pi 6^4 \nu 7^1$ intruder configuration. Four $j = 13/2$ particles have a positive Q_{44}, as does a single $j = 15/2$ particle. Thus, staggering is expected for this band. On the other hand, ^{150}Gd(1) has a $\pi 6^2 \nu 7^2$ configuration, for which both contributions are negative. No staggering is expected in this case.

Unfortunately, ^{149}Gd(1) is a tougher case because the proton contribution is negative and the neutron contribution positive. As a result, one must rely more heavily on the accuracy of the calculations, and the role of other orbitals may be more important. Nevertheless, the model's predictions are testable and will be rigorously

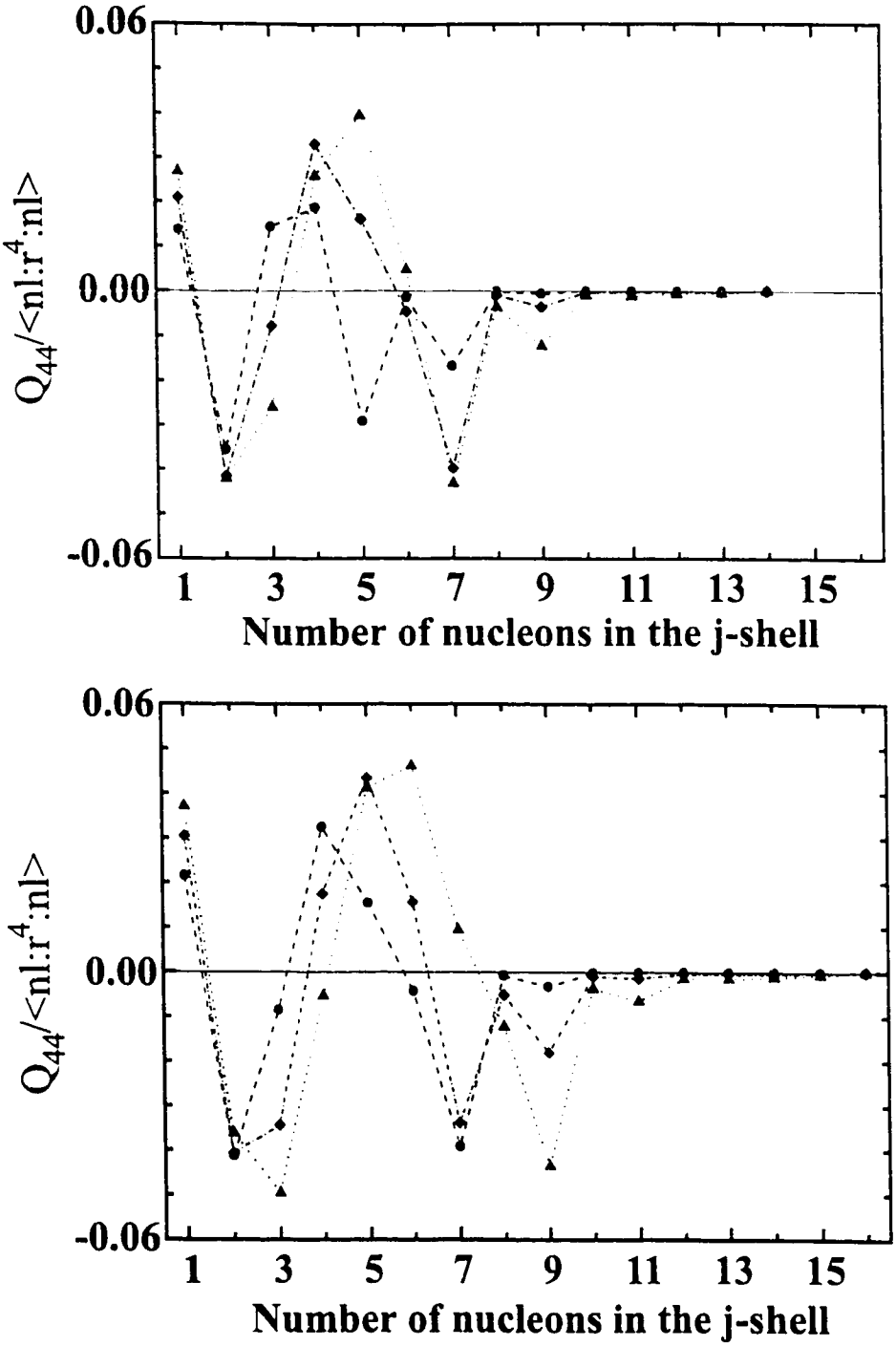

Figure 2.6: Moments Q_{44} for $j = 13/2$ (upper panel) and $j = 15/2$ (lower panel) subshells. Calculations are performed for rotational frequencies ω of 0.4 MeV (circles), 0.6 MeV (diamonds), and 0.8 MeV (triangles). Taken from [Pav97b, Pav98].

tested in this thesis.

The theoretical stage is now set for this investigation of $\Delta I = 4$ bifurcation in superdeformed bands. It is now important to understand the experimental techniques used in this thesis, before the discussion of the data begins.

Chapter 3

Experimental Techniques

This chapter describes some of the experimental and data analysis techniques that were used to perform the data collection and analysis described in this thesis.

3.1 Heavy-Ion Fusion-Evaporation Reactions

High-spin nuclear states are most often populated in heavy-ion fusion-evaporation reactions. In these reactions, a beam of projectile nuclei (e.g. ^{29}Si) is sent through a target composed of some other material (e.g. ^{124}Sn). In the experiments described in this thesis, the targets were about one micrometer thick; these thicknesses are normally given in micrograms per square centimeter. If the beam energy is high enough for the target and projectile nuclei to overcome their Coulomb repulsion, they can fuse, forming a compound nucleus (in this case, ^{153}Gd). The compound nucleus formed has a fixed excitation energy, given by the beam energy and the Q-value for the reaction; however, the angular momentum of the compound nucleus has a wide distribution, related to the distribution of impact parameters for the reaction. For the reactions considered in this thesis, the compound nuclei were formed at an excitation energy greater than 50 MeV, with angular momenta as high as 70$\hbar$.

When it is formed, the compound nucleus is excited to tens of MeV above

the yrast line, and must find a way to cool off. This is most often accomplished by neutron evaporation, although fission can compete with this process at the highest angular momenta. Neutron evaporation carries away almost 10 MeV [Hac96], on average, in binding energy and kinetic energy; this makes it much more efficient than γ-ray emission, which removes only a few MeV on average. Neutrons take away only about $1\hbar$ in angular momentum, so the angular momentum distribution is largely unaltered. The compound nucleus can also emit protons or alpha particles, but these charged particles must overcome a Coulomb barrier in order to escape. Thus, their emission is often suppressed, unless the compound nucleus is neutron deficient.

Neutron emission continues until the system is within one neutron binding energy of the yrast line. At this point, it can no longer emit neutrons, and the cooling process continues by γ-ray emission. At first, the nucleus is still at a relatively high excitation energy above the yrast line, and the level density* is large. This means that the number of possible decay pathways down to the yrast line is also large, and so the decay produces a continuum of γ-ray energies. Some information can be gained from the analysis of this continuum, but such analyses are not performed in this thesis, and the continuum serves only as a source of background.

As the decay path gets close to the yrast line, the level density decreases, and the population of specific pathways becomes large enough for these pathways to be observed through their individual γ rays. The superdeformed bands analyzed in this work are all yrast or near-yrast decay pathways at angular momenta above $50\hbar$, whose γ-ray decays can be seen in discrete peaks.

Below $50\hbar$, the superdeformed structures are no longer yrast. However, the transition matrix elements between adjacent superdeformed states are so large that

*"Level density" refers to the number of energy levels present at a given excitation energy, per unit excitation energy. It increases exponentially as one moves away from the yrast line.

in-band decays remain favoured until spins as low as $25 - 35\hbar$. At these lower spins, the nucleus is again several MeV in excitation energy above the (normal-deformed) yrast line, the normal-deformed level density becomes quite large, and a continuum decay takes over again. Experimenters have not been able to find discrete-line decay pathways between the superdeformed bands and the normal-deformed states in the $A \sim 150$ region; this has made it impossible to make spin and excitation energy assignments for the superdeformed bands in this region.

3.2 Gamma-Ray and Charged-Particle Detectors

In this work, the γ rays emitted by the residual nuclei are studied. This makes the γ-ray detectors the key experimental apparatus. A charged-particle detector, the Microball, also plays an important role in one of the experiments described in this thesis, so the operation of these detectors will also be addressed.

Both γ-ray and charged-particle detectors operate on the same principle. The γ ray or charged particle enters some detection medium, and creates electron-hole pairs. With charged particles, this is done through direct ionization of atoms by the charged particles. Gamma rays first create energetic electrons, through the photo-electric effect, Compton scattering, or pair production; these electrons then ionize the atoms in the detection medium. These electrons and holes are then detected to infer some of the properties of the incident particle or γ ray.

The detectors in use today fall into two categories, solid-state detectors and scintillators. These are discussed in the following sections.

3.2.1 Solid-State Detectors

In solid-state detectors, the detection medium is a semiconductor, such as silicon or germanium, doped to make a large p-n diode. The diode is reverse-biased at several thousand volts to make the depletion zone as large as possible, since it is this volume which is the active detection region. When electron-hole pairs are liberated in the depletion zone, they are quickly swept away by the large electric field in the detector. The charge collected is proportional to the energy of the incident radiation.

The γ-ray spectroscopy in this thesis was done with germanium detectors. Germanium detectors provide the experimenter with excellent energy resolution (full-width at half-maximum of 2 keV for a 1 MeV γ ray). However, in addition to the full-energy peak, there is a continuum spectrum extending from that peak down to zero energy (see Figure 3.1). This continuum results from events in which the Compton-scattered γ ray escapes from the germanium crystal before depositing all of its energy. This Compton background can be suppressed by surrounding the germanium detector with sensitive detectors to detect the escaping γ ray, and then discarding signals from the germanium detector that are accompanied by a signal from one of the surrounding detectors. However, the Compton background remains a non-negligible source of background for these detectors.

Today's high-spin γ-ray spectroscopy is done with arrays of Compton-suppressed germanium detectors. The experiments described in this thesis were performed with Gammasphere[Lee90], an American array consisting of up to 110 detectors. This detector can be run on its own, or in conjunction with a variety of auxiliary detectors. One of these auxiliary detectors is the Microball [Sar96], a charged-particle detector which will be described briefly in the following section.

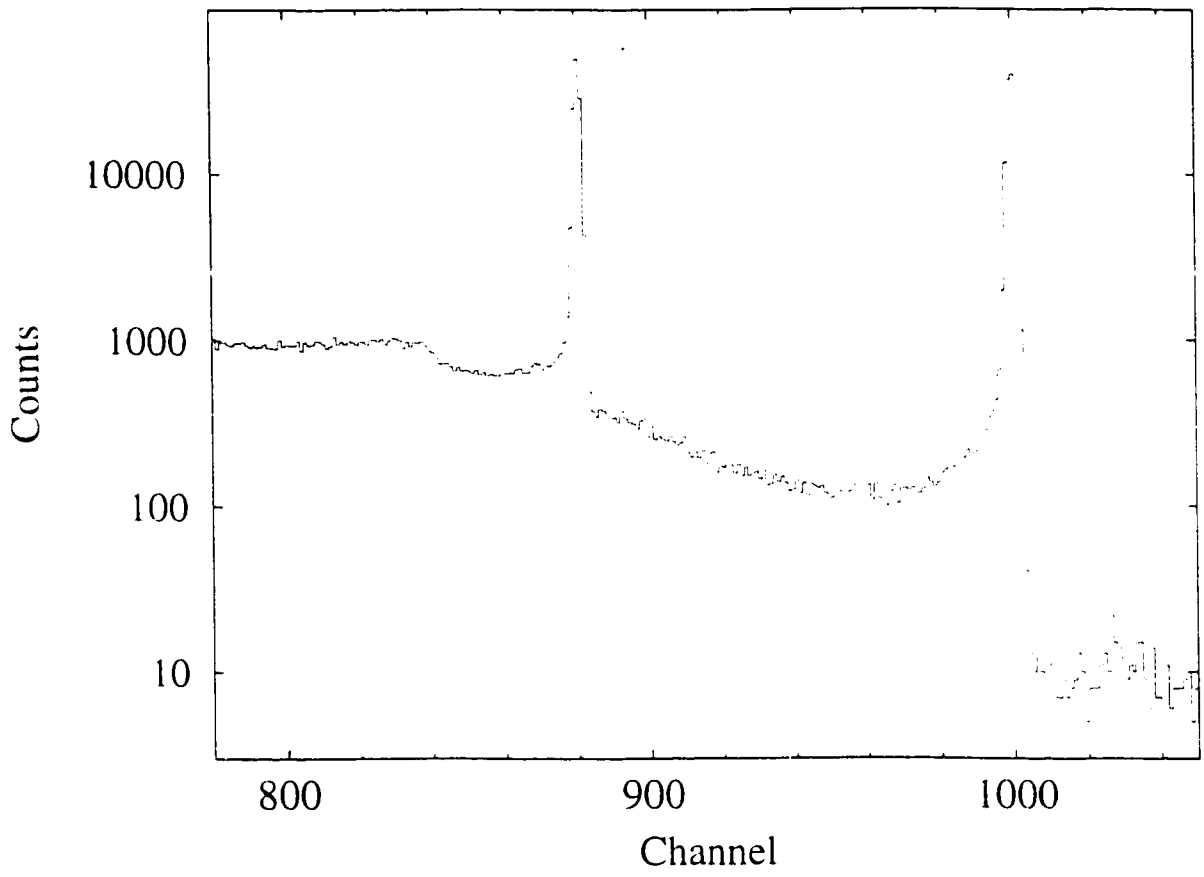

Figure 3.1: Illustration of the Compton background. The spectrum shown is of a ^{60}Co source, collected with one of the Gammasphere germanium detectors. Compton suppression has been turned off. Data is taken from [Sve98].

3.2.2 Scintillators

Scintillators do not directly detect the electrons and holes, but rather the visible light that is emitted when they recombine. Scintillators made from bismuth germanate (BGO) are used as Compton suppressors for the germanium detectors in Gammasphere. The Microball uses an array of 95 cesium iodide scintillators to detect protons and alpha particles emitted in fusion-evaporation reactions.

The principles behind charged-particle spectroscopy are slightly more complicated than those behind γ-ray spectroscopy. As with γ rays, the amount of light collected from the scintillator is proportional to the energy of the incident particle. However, one also wants to know what type of charged particle is incident. This is done by looking at the time profile of the light collection, as described below.

Alpha particles, due to their larger charge, are stopped more quickly in the detector than a proton of the same energy. As a result, their energy is deposited over a smaller region, and so the electron-hole pairs are more likely to be created as bound pairs (excitons) [Leo87]. Protons, on the other hand, distribute their energy over a larger region, and a smaller fraction of the electron-hole pairs are excitons. In cesium iodide, excitons have a shorter recombination time than free electron-hole pairs. As a result, the light emission for an alpha particle takes place over a shorter time than for a proton. This is exploited in the identification of charged particles in cesium iodide.

3.3 Coincidence Spectroscopy

The top panel of Figure 3.2 is a background-subtracted partial γ-ray spectrum obtained from the GS-118 experiment discussed in this thesis. The spectrum shows all of the γ rays observed in this experiment, and is often called the "total projection". Due to the nature of heavy-ion fusion-evaporation reactions, many nuclei are produced in this experiment, and the total projection is known to contain γ rays from $^{145-148}$Eu and $^{145-147}$Sm. Thus, if one wants to assign γ rays to a particular nucleus, or if one wants to study very weak structures, like superdeformed bands, one has to look beyond the total projection. Today's γ-ray spectrometers detect in germanium detectors as many as 6 or 7 of the γ rays emitted by a given compound nucleus, so one can make great strides by asking which γ rays are seen in coincidence with other

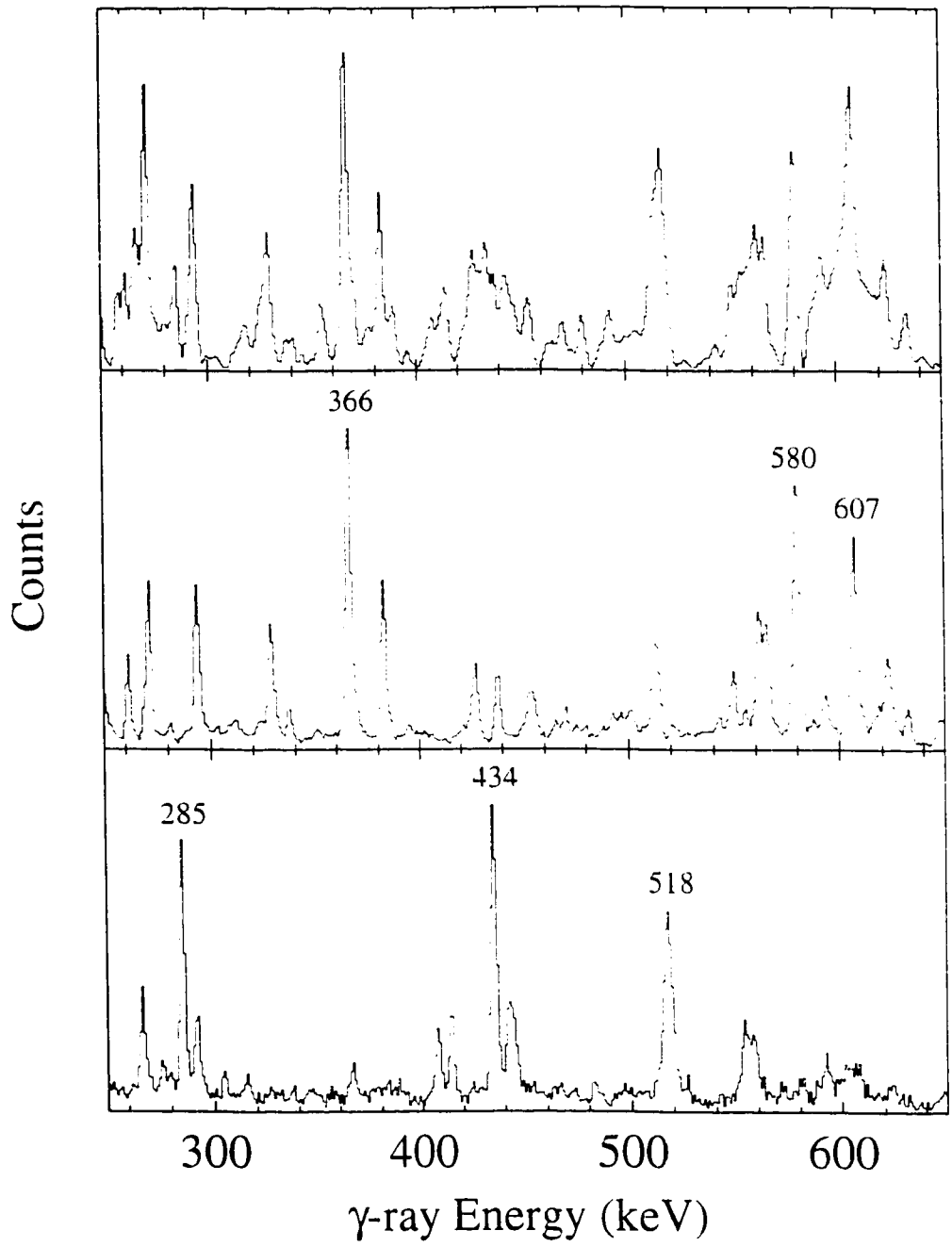

Figure 3.2: A demonstration of coincidence spectroscopy. In the top panel is the total projection. In the middle panel is the spectrum in coincidence with the 721 keV γ ray in ^{147}Eu, while the bottom panel shows the spectrum in coincidence with the 1439 keV γ ray in ^{146}Eu.

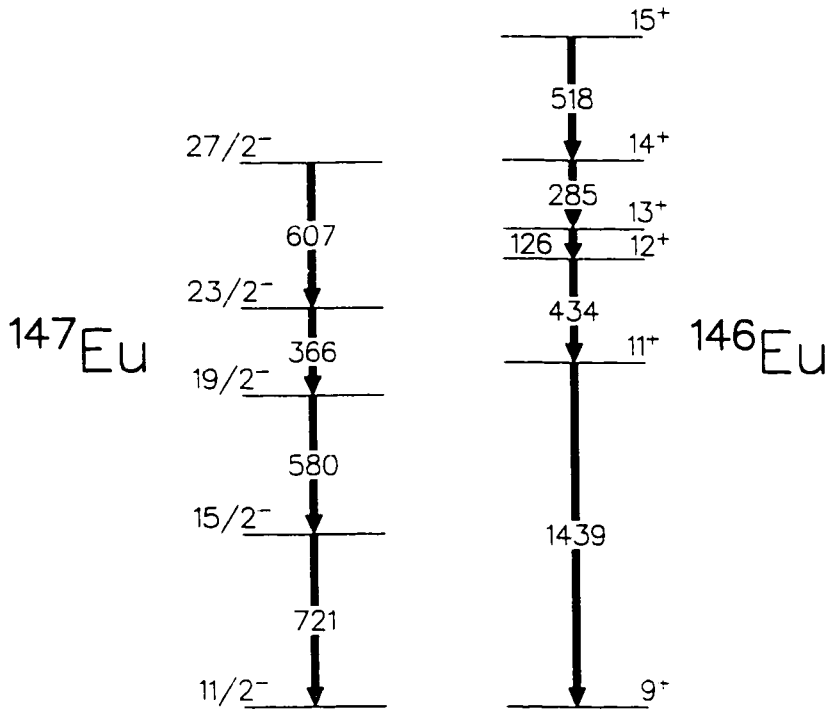

Figure 3.3: Partial level schemes of ^{146,147}Eu. Gamma-ray energies are given in keV. Levels are labelled by their spin I and parity π, as I^{π}.

γ rays. A simple example of this technique follows.

Partial level schemes of ^{146,147}Eu are shown in Figure 3.3 [Erc88, Fle77, Zho97]. Because the γ rays on the left are in the same cascade, they should be seen in coincidence with one another. For example, if the 607 keV γ ray is observed, the ones below it in the cascade were also emitted, and may have been detected. The same is true of the γ rays on the right. However one should not expect to see the 721 keV γ ray in coincidence with any of the ones on the right; they belong to different nuclei.

and should not be emitted in the same event (that is, by the same residual nucleus).

This is demonstrated in Figure 3.2. The middle panel is the spectrum of γ rays in coincidence with the 721 keV γ ray, while the bottom panel is the spectrum in coincidence with the 1439 keV γ ray (in the language of γ-ray spectroscopy, the 721 keV or 1439 keV γ ray are called "gates", and the spectra in coincidence with them are called "gated spectra"). As expected the 721-gated spectrum has peaks at 366 keV, 580 keV, and 607 keV, while the 1439-gated spectrum has peaks at 285 keV, 434 keV, and 518 keV; neither spectrum has peaks belonging to the other cascade. In addition, the gated spectra each have fewer peaks than the total projection, as a result of the exclusion of other channels. This allows more detailed spectroscopy to be done. This technique can not only be used to separate reaction channels; it can also be used distinguish between different decay paths in the same nucleus, and more generally to determine what the decay pathways are in a given nucleus.

3.3.1 Multiple Gating

Analysis is often performed on spectra in coincidence with two or more γ rays. This allows even more selectivity in choosing a given decay path, and it reduces further the uncorrelated backgrounds, such as the Compton background. An example of the power of multiple gating in the spectroscopy of superdeformed bands can be seen in Figure 3.4, described in the following paragraphs.

The uppermost panel of Figure 3.4 shows the total projection from an experiment on ^{148}Gd. This nucleus has a superdeformed band with nineteen known transitions. However, it is populated in only one percent of all reactions populating ^{148}Gd, and so it cannot be seen in the total projection.

One can improve things by setting gates. The other panels in Figure 3.4 show sums of spectra gated once, twice, three times, four times, five times, and six times

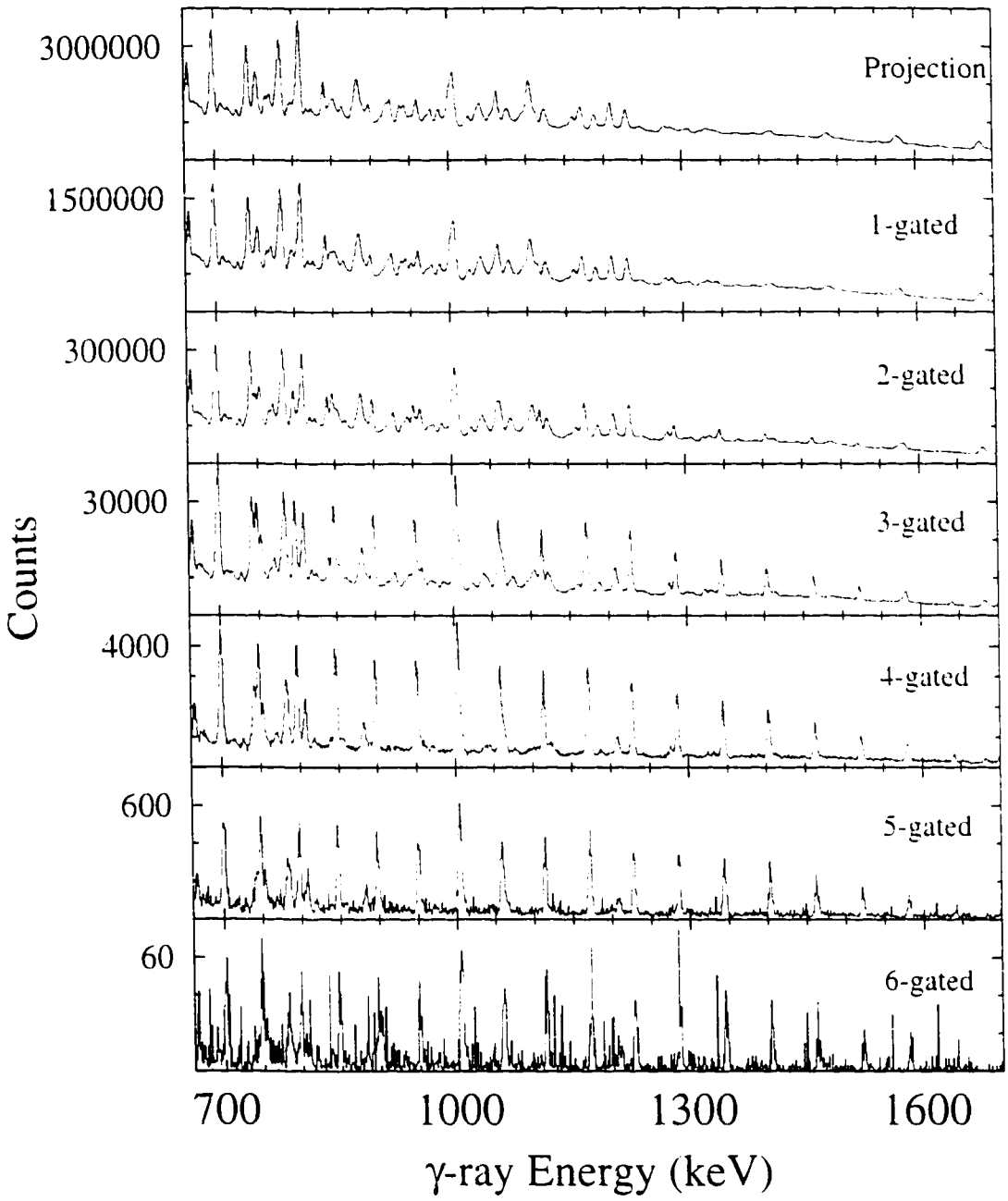

Figure 3.4: Gated spectra of the superdeformed band ^{148}Gd(1).

on the band. That is, the second panel shows the sum of the spectrum gated on the first transition, plus the spectrum gated on the second transition, and so on up to the nineteenth transition. It is clear that one can enhance the signal from the band, and simultaneously decrease the background by setting large numbers of gates.

The biggest drawback to setting multiple gates is the loss in statistics. Requiring an event to contain four γ rays from the band is a stringent condition. One is fortunate with superdeformed bands that they contain so many transitions: with nineteen transitions, the quadruply-gated spectrum in the figure is a sum of $\binom{19}{4} = 3876$ individual quadruple-gated spectra. However, the figure shows how one cannot set arbitrarily high gating conditions.

3.3.2 Elliptical Gating

A single-gate condition is a statement of the form, "if the γ-ray energy lies between a and b, ...". This can be generalized to two dimensions, to become, "if the first γ-ray energy, E_1, lies between a and b, and the second γ-ray energy, E_2, lies between c and d, ...". This kind of gate is called a rectangular gate (imagine a graph of E_1 versus E_2, and picture the region passing the gating condition). The spectra in Figure 3.4 used rectangular gates, and their higher-dimensional analogs; they are obviously highly effective, but they could be improved. In E_1E_2 space, the peaks do not have a rectangular geometry, but an elliptical one with axes in the ratio $(b-a) : (d-c)$ (see Figure 3.5). This means that the corners of the rectangular gate contain mostly background.

This situation can be ameliorated with a so-called "elliptical gate" [Cro95, Wil97b]. That is, in place of the rectangular gating statement above, one uses the condition, "if the point (E_1, E_2) lies within the ellipse centred at $(\frac{a+b}{2}, \frac{c+d}{2})$ with

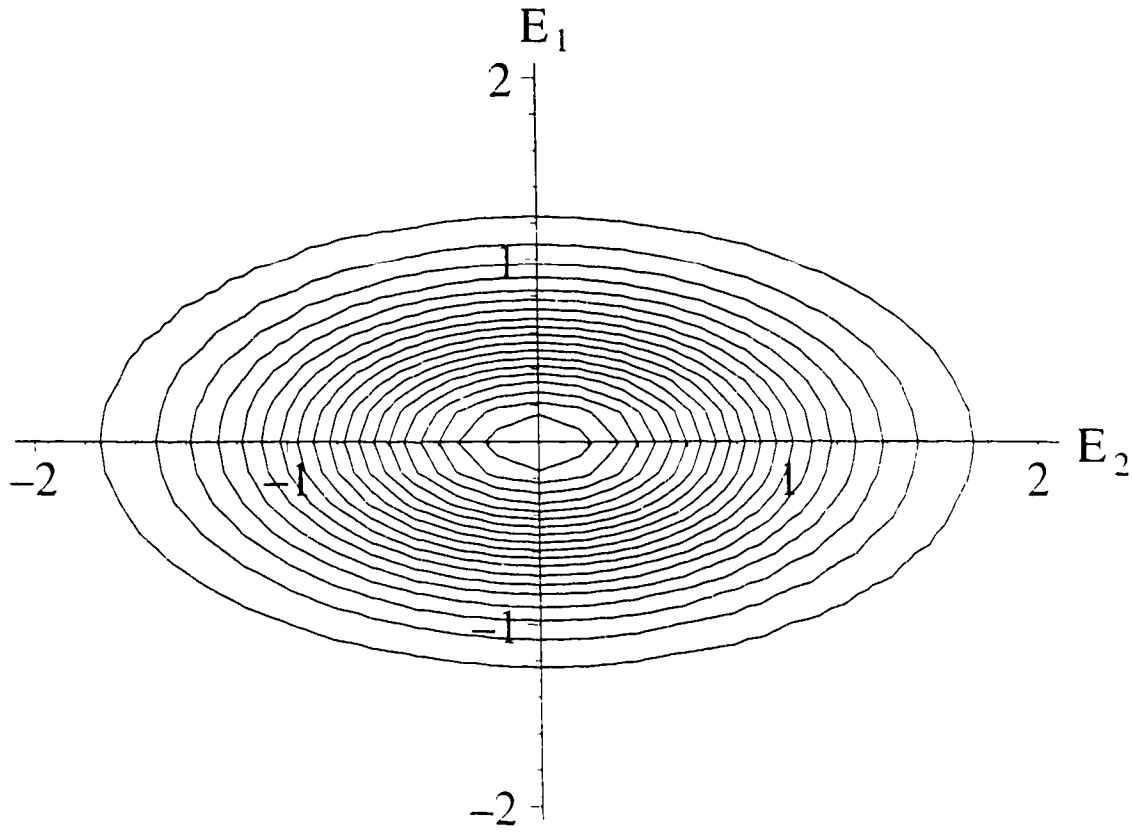

Figure 3.5: Contour plot of a two-dimensional Gaussian distribution. Note that the distribution has an elliptical geometry in E_1E_2 space.

axes $\frac{b-a}{2}$ and $\frac{d-c}{2}$, ...". Although the implementation of such a statement is more computationally intensive than that of a rectangular gate, it can be useful in reducing backgrounds.

3.3.3 Spike-Free Incrementation

The reader will likely have noticed that the sextuply-gated spectrum in Figure 3.4 contains some decidedly non-statistical fluctuations. These anomalies, called spikes, arise as a result of the algorithm used to create these spectra, as discussed below.

For many years, the efficiency of γ-ray spectrometers was such that they could collect only two γ rays per event (called 2-fold data). As a result, data analysis techniques developed around the analysis of "doubles". Events with three detected γ rays were too infrequent to be analyzed by double-gating; as a result, they were "unpacked" into doubles. That is, an event with γ-ray energies (E_1, E_2, E_3) was converted into three double-coincidence events, (E_1, E_2), (E_1, E_3), and (E_2, E_3). This caused no problems and became standard.

When the present generation of spectrometers began operation, data were available with more γ rays, analysis took place with multiple gates, and the practice of unpacking continued. If, for instance, one wanted to triple-gate, then only 4-fold data were required. All events with five or more γ rays were then unpacked into quadruples prior to analysis. However, this procedure leads to the production of spikes in some situations.

Consider an event with eight γ rays, seven of which fall inside gates of a superdeformed band. If one wants to make a sextuply-gated spectrum, then this eight-fold event is unpacked into eight seven-fold events. Seven of these events contain the γ ray that does not fall inside the gates, and six that do. As a result, the γ-ray energy falling outside the gates will be incremented seven times in the spectrum. These incrementations are not independent of one another, and so the spectrum is no longer statistically correct, in that the spectrum no longer obeys Poisson statistics.

Beausang *et al.* [Bea95] have suggested an incrementation scheme in which these spikes are not created. Their algorithm takes each γ ray in the event in turn, and asks whether the gating conditions are satisfied by the rest of the γ rays in the event. If so, that energy is incremented once in the spectrum; if not, then no incrementation is made. Obviously, in this scheme a given energy is incremented only once and spikes

are eliminated.

3.4 Background Subtraction

In practice, $A \sim 150$ superdeformed bands can be studied most effectively with the present generation of detector arrays by triple-gating. However, it is clear from Figure 3.4 that there is a significant quantity of background in a triple-gated spectrum. The question of how to subtract background is, therefore, important. As will become clear later in the thesis, the proper treatment of this background is absolutely critical to the accomplishment of the goals of this research.

As discussed in Section 3.2.1, the germanium spectrum of a monoenergetic γ-ray source will consist of a peak at the full energy and a Compton tail extending to lower energies. The spectrum obtained from a heavy-ion experiment consists of hundreds of discrete peaks, each with its own Compton tail. These backgrounds combine to form a smooth background underlying all of the peaks.

A second source of background is continuum γ rays. Section 3.1 described two instances where the γ-ray decay proceeds by a myriad of unresolved pathways. This kind of decay also produces a broad background spectrum underlying all of the peaks.

Consider first a spectrum arising from a single gate on an energy E_1. This spectrum will contain background for two reasons. First, the gate includes both a peak and the background underlying it. The gated spectrum contains, therefore, the spectrum in coincidence with the peak and the spectrum in coincidence with the background. This latter contribution is a source of discrete lines, Compton backgrounds, and continuum backgrounds not desired in the gated spectrum. Second, even the spectrum in coincidence with the peak contains the Compton and continuum back-

grounds inherent to that spectrum. This is a less offensive form of background, but can be distracting. The primary goal of background subtraction is to remove the first component to the background; the second is a smooth curve which can be removed by hand. It should also be noted that for multiply-gated spectra, the first component becomes much more complicated, whereas the second component retains its simplicity.

The task, then, is to create the spectrum in coincidence with the background underlying the gated peak. This spectrum can then be subtracted from the gated spectrum, leaving the spectrum of interest. Twenty years ago, a common approach would be to set a gate on a region close to the original peak, but free of discrete lines. This is exactly the spectrum required, as long as the spectrum in coincidence with the background is not too sensitive to where the background gate is taken. It turns out that this is an excellent assumption.

This method is not without its drawbacks. There are often cases where it is impossible to find a peak-free region close to the gate. Second, the generalization of this method to a multiply-gated superdeformed band is very complicated.

Palameta and Waddington [Pal85] suggested that the above assumption (that the background spectrum is independent of the position of the background gate) is so good that one can make a single background spectrum gated on all background channels in the spectrum. This background spectrum can be used as the background for all single-gated spectra. Moreover, since the total number of background channels is large, this spectrum can be made with great statistical accuracy. The generalization of this method to higher folds is also considerably simpler than the earlier alternative. This is further explored in the following section.

3.4.1 Background Subtraction in Higher Folds

This section will give the reader a sense of how background subtraction is performed on multiply-gated spectra. For a complete discussion of this topic, the reader is directed to the article by Hackman and Waddington [Hac95].

Consider a spectrum triple-gated on three γ rays. This spectrum can be thought of as comprising four separate components:

1. a spectrum in genuine triple-coincidence with the γ rays of interest,
2. a spectrum in coincidence with two of the interesting peaks and the background underlying a third,
3. a spectrum in coincidence with one of the interesting peaks and the backgrounds underlying two others, and
4. a spectrum in coincidence in triple-coincidence with the backgrounds underlying the peaks.

Only component 1 is desired. Components 2, 3, and 4 should be subtracted.

In analogy with the discussion in the preceding section, a spectrum of component 2 may be produced by triple-gating on two peaks of interest and a set of background channels. Similarly, components 3 and 4 may be extracted. Even a spectrum employing a sum of triple gates, as in Figure 3.4, is only marginally more complicated, since the set of background channels is taken to be universal, and not affiliated with any particular gate.

There are some complications in this scheme. For example, the peak-peak-background gate used to create the spectrum for component 2 contains components 3 and 4 as backgrounds. As a result, when this spectrum is subtracted from the

original triple-gated spectrum, component 3 is oversubtracted, and must be added back. In addition, while the use of a single set of background channels simplifies enormously the background subtraction of a spectrum made from a sum of multiple gates, there are still fairly detailed combinatorics arguments which determine how much of each background spectrum to subtract from, or add to, the original in order to recover component 1. However, the so-called "operator method" of Hackman and Waddington lays out all of these details.

This chapter has described the important principles underlying the collection of γ-ray spectroscopy data, and its analysis. Coupled with the knowledge of nuclear structure theory gleaned from the preceding chapters, this information should have the reader properly primed to understand and appreciate the results presented in the chapters to come.

Chapter 4

Staggering in Identical Bands

This chapter presents the results of an experiment performed in July 1996 to study the staggering phenomenon. It concludes with a discussion of the importance of this work to the current understanding of the effect.

4.1 Motivation for the Experiment

Section 2.5 described $\Delta I = 4$ bifurcation and the excitement it generated in the nuclear structure community. The first evidence of this phenomenon came from ^{149}Gd(1) [Fli93]. The staggering pattern in this band remains the clearest single example of the effect, since it shows a regular oscillation that persists over $20\hbar$ in angular momentum. Although several groups have claimed to see staggering in other superdeformed bands [Sem96, deA96, Fis96, Ced94, Kru96], doubt remains regarding the statistical significance and reproducibility of these results.

An understanding of this phenomenon clearly demands investigation of staggering in nuclei other than ^{149}Gd. Knowing which bands exhibit $\Delta I = 4$ bifurcation could be valuable in determining which aspects of the structure of these bands might be responsible for the effect. Pavlichenkov's model, for instance, makes definite predictions about certain orbitals and their contribution to the staggering phenomenon.

It can, therefore, be rigorously tested if it is known which bands in the mass region exhibit the staggering effect. As a result, a systematic survey of the mass region could be very useful in tracking down the cause of $\Delta I = 4$ bifurcation. However, with the modern γ-ray spectrometers in high demand, a more focussed and less time-consuming experiment must be proposed.

As discussed in Appendix A, Hamamoto and Mottelson have shown that, in their model, the staggering amplitude is approximately proportional to $\cos(\frac{\pi}{2}(I-I_0))$, where I_0 is a phase factor uniquely determined by the parameters A and B_1 of their Hamiltonian [Ham94]. This might have some predictive power if one knew the origin of these parameters. For instance, this expression would be useful if one knew that the parameters were the same in two different bands. If that were the case, then one could begin to constrain the model parameters.

Is there a possibility that pairs of bands can be found in which the parameters of the model Hamiltonian are the same? An intriguing avenue of investigation is to study pairs of *identical* bands. As discussed in Section 2.4, identical bands have γ-ray energies that are correlated to a much higher degree than might be expected. The origin of this phenomenon is not yet understood, and so the extent of the similarity may run deeper than is generally realized. If any bands have a chance of sharing C_4 Hamiltonian parameters, identical bands do.

It has previously been noted that the removal of a proton from the negative-signature [301]1/2 Nilsson orbital in ^{152}Dy and other $A \sim 150$ nuclei generates an isospectral identical band. As shown in Figure 4.1, this orbital is occupied and at the Fermi surface of ^{149}Gd(1), suggesting that the yrast superdeformed band in ^{148}Eu should be identical to ^{149}Gd(1). Being yrast, this band should be easy to populate and identify.

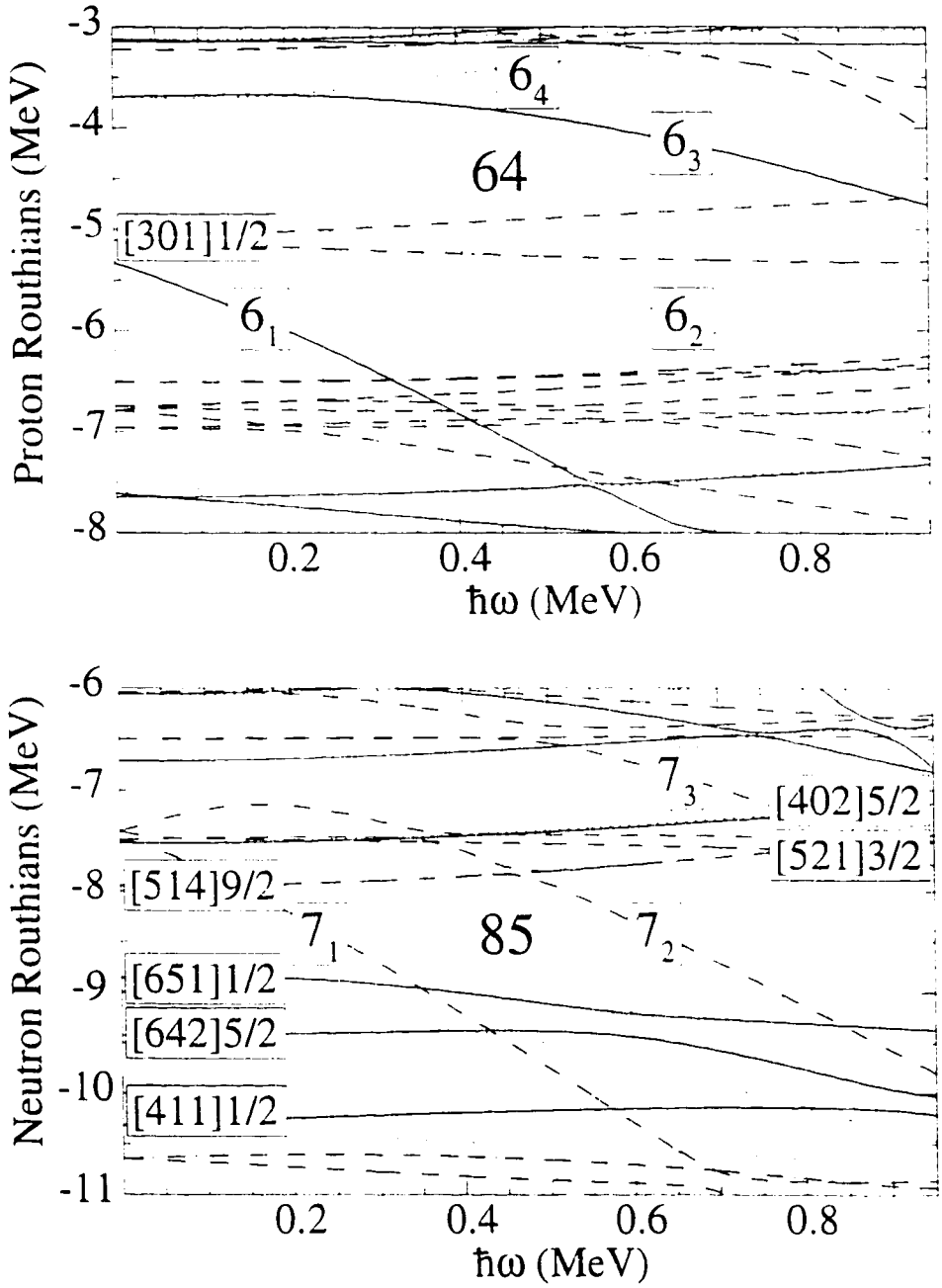

Figure 4.1: Single-particle Routhians at deformations $(\beta_2, \beta_4, \gamma) = (0.57, 0.07, 3.8°)$. Orbitals with parity and signature $(\pi, \alpha) = (+, +\frac{1}{2})$, $(+, -\frac{1}{2})$, $(-, +\frac{1}{2})$, and $(-, -\frac{1}{2})$ are indicated by solid, dotted, dash-dotted, and dashed lines, respectively.

Before proceeding, it should be noted that, even if the parameters of the C_4 Hamiltonian do not remain the same in the two bands, this is an interesting experiment to perform. Superdeformed configurations have not previously been observed in any europium nuclei with $A > 144$. The experiment thus probes nuclei which have not been studied at high spins. In addition, because ^{148}Eu and ^{149}Gd differ by only one proton, the configurations of the superdeformed structures in these nuclei are expected to be quite similar. The presence or absence of staggering in ^{148}Eu bands may still, therefore, provide information regarding the nuclear structure origin of $\Delta I = 4$ bifurcation, as discussed at the beginning of this section.

4.2 The Experiment

By the standards of high-spin nuclear physicists, ^{148}Eu is neutron-rich. This means that neutron evaporation will dominate over charged-particle evaporation in a heavy-ion fusion-evaporation reaction producing ^{148}Eu. Ideally, therefore, a beam and target combination is desired that can populate ^{148}Eu in a neutron evaporation channel.

Unfortunately, no combinations exist that can populate ^{148}Eu with the spin and excitation energy appropriate to a study of superdeformed bands. One must, therefore, resort to a reaction in which a charged particle is emitted. A proton emission channel is preferred, since alpha particles tend to remove more angular momentum.

There are several suitable reactions populating ^{148}Eu, at the right spin and excitation energy, in which a proton is emitted. A beam of ^{29}Si with an energy of 158 MeV and a 700 μg/cm^2 target of ^{124}Sn was chosen. This produces ^{148}Eu following the evaporation of one proton and four neutrons. This experiment was carried out at the Ernest Orlando Lawrence Berkeley National Laboratory, with the 88-Inch Cyclotron

providing the beam. The γ-ray decays were detected with Gammasphere. Because the probability of proton emission from the compound nucleus is small for this reaction, it was expected that the decays of the europium nuclei would be outnumbered by a factor of ten by decays from gadolinium, formed after evaporation of neutrons only. As a result, even the strongest bands in ^{148}Eu would be as difficult to detect as the weakest ones in ^{148}Gd. To remedy this situation, the Microball was used in conjunction with Gammasphere to detect the evaporated protons. In this way, the weak europium channels could be cleanly separated from the strong gadolinium channels*. With this channel separation, strong bands in ^{148}Eu could be detected easily and spectra of these bands could be produced without contamination from the gadolinium channels. In a five-day experiment, 240 million proton-gated four- and higher-fold events were collected. Events in which no charged particles were detected numbered 1.8 billion.

As mentioned above, a consequence of using this reaction is the production of a large data set for ^{147,148}Gd, with ^{148}Gd produced optimally for superdeformation. Although these nuclei have been well studied by others [The96, deA96, deF95, Byr98], a thorough analysis of the staggering in these nuclei has not been performed. Of special interest is ^{148}Gd(6)†. This band is identical to ^{149}Gd(1) and has the ^{149}Gd(1) configuration [deF95], with a neutron hole in the positive-signature [411]1/2 orbital (see Figure 4.1 for the neutron Routhians in this mass region). As described in Section 2.4.1, this orbital is also significant in the pseudospin explanation of identical bands; this makes it another interesting candidate for study. This band and ^{148}Eu(1)

*Alpha particles were also detected with the Microball, leading to the formation of superdeformed states in ^{145}Sm. A description of the two observed bands does not appear in this thesis, but can be found in [Has98a].

†In this thesis, the superdeformed bands in ^{148}Gd are numbered with the scheme suggested in Reference [deF95], and employed in [Sin96, Has97, Byr98]. An alternate numbering scheme exists, suggested in Reference [deA96] and used in [The96, Pav97b, Has98b]. In this latter scheme, bands numbered 1-6 in this thesis are numbered 1,2,6,5,3, and 4, respectively.

are the focus of this chapter; analyses of the other bands in ^{147,148}Gd are left to Chapter 5.

4.3 Experimental Results

4.3.1 New Bands

The codes EVOLVE [Wil97a] and ANDBAND [Has94] were used to search the proton-gated data for superdeformed bands. These searches revealed two bands in ^{148}Eu. The more intense band, named ^{148}Eu(1), was populated with an intensity of $0.79 \pm 0.08\%$ relative to the ^{148}Eu channel[§], and is assigned the single-particle configuration discussed earlier in this chapter, the ^{149}Gd(1) configuration with a hole in the negative-signature [301]1/2 proton orbital. The less intense band, ^{148}Eu(2), was populated with an intensity of $0.24 \pm 0.03\%$ relative to the channel, and is assigned the same configuration, but with the hole in the positive-signature [301]1/2 proton orbital instead. For further information on the configuration assignments of these bands, the reader is urged to see Reference [Has98b].

4.3.2 Transition Energy Determination

All analysis in this thesis was performed on triple-gated spectra. It is possible that quadruple-gating is optimal for the most intense bands in the gadolinium data sets analyzed in Chapter 5. However, because these bands are so intense, these considerations are not important. In most cases, the spectra were created with spike-free incrementation, with the background subtracted according to the operator approach.

For the purposes of this thesis, the most important quantities measured in these bands are their transition energies, since these permit the extraction of stagger-

[§]The intensities are extracted as explained in [Has98b]; for more detail on intensity measurements in gated spectra, the reader is directed to [Hac96].

ing data. To extract these energies, the γ-ray peaks were fitted with Gaussian shapes with the code GF2 [Rad85]. The background was fixed to be flat, and in most fits it was fixed to be zero. The transition energies are, however, relatively insensitive to the height of the background.

In cases where a peak was deemed to be "contaminated" by a peak from the normal-deformed level scheme, this normal-deformed peak was fitted in the background spectrum, and its position and width obtained from this fit were fixed in the fit of the superdeformed band spectrum.

The GF2 code may be used to find the height, width, and centroid of each superdeformed peak. Obviously, the degrees of freedom associated with the widths contribute to the uncertainties in the centroids. For this reason, it has been useful to fix the widths of the peaks. In a preliminary fit, the widths were allowed to vary. The widths, W, extracted from these fits, were then fitted to the function proposed by Radford [Rad94]:

$$W = \sqrt{F^2 + G^2 x + H^2 x^2}, \tag{4.1}$$

where F, G, and H are parameters, and x is the channel number divided by one thousand. The widths of the superdeformed peaks were then fixed according to this function and the spectrum was re-fit. In cases where several bands were fit in the same nucleus, the parameters (F, G, H) extracted from the fit of the most intense band were used to fix the widths in all of the bands. This is desirable because the width parameters are determined by Doppler broadening and detector characteristics, and so should be the same for all bands in a given nucleus produced in a given experiment.

Figure 4.2 shows partial γ-ray spectra of the bands ^{148}Eu(1) and ^{148}Gd(6). The transition energies of these bands are given in Table 4.1. The transition energies for ^{148}Eu(2) will be presented in Chapter 5, when the staggering of this band is

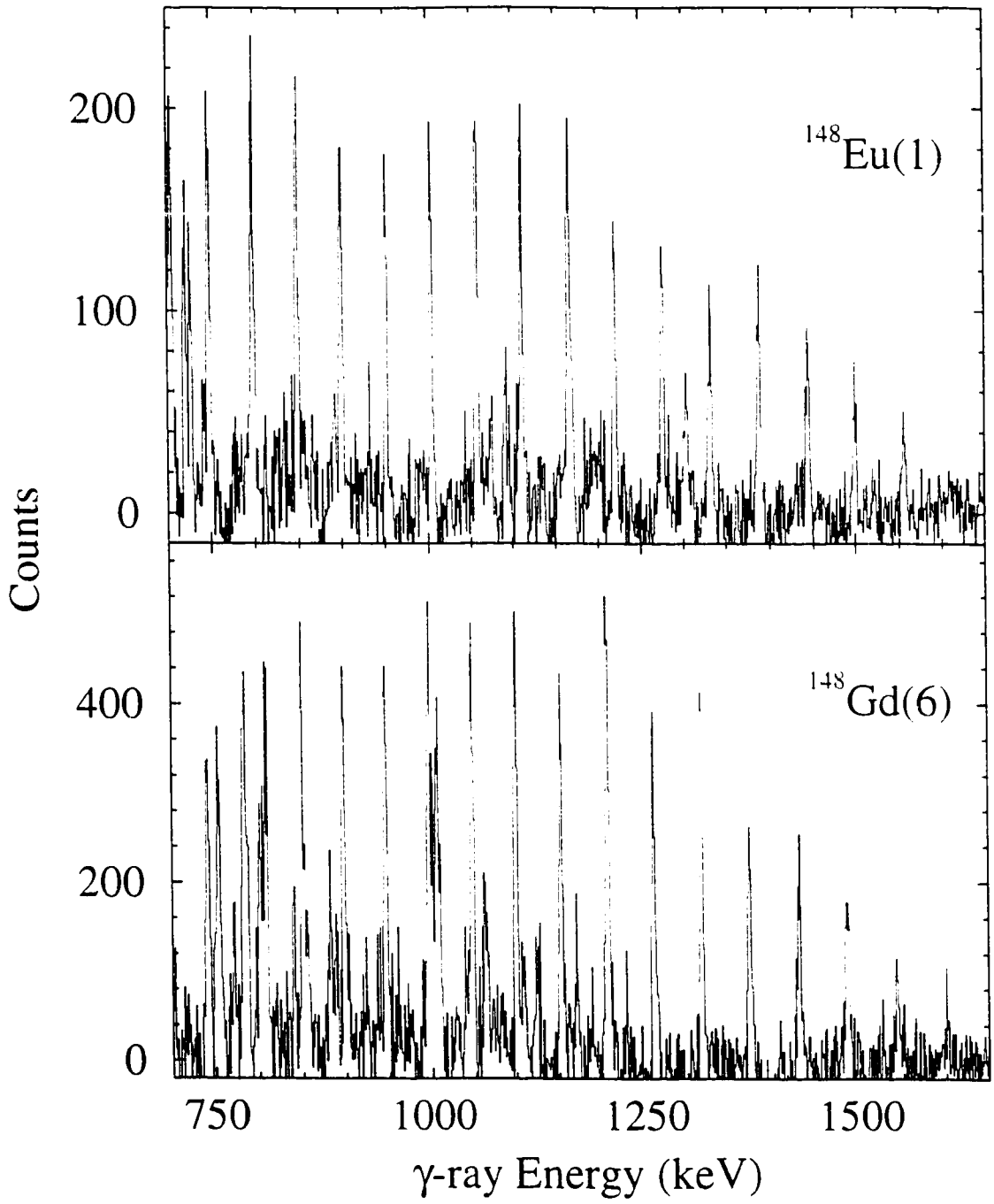

Figure 4.2: Partial γ-ray spectra of ^{148}Eu(1) and ^{148}Gd(6).

Table 4.1: Gamma-ray transition energies, in keV, of the superdeformed bands ^{148}Eu(1) and ^{148}Gd(6).

^{148}Eu(1)	^{148}Gd(6)
747.7(1)	849.2(2)
797.9(2)	897.3(2)
848.3(1)	945.7(2)
899.5(2)	995.9(2)
951.4(2)	1046.7(1)
1003.8(2)	1099.2(2)
1057.1(2)	1152.0(1)
1110.7(2)	1206.6(2)
1165.3(2)	1260.8(2)
1220.1(2)	1316.4(1)
1275.7(2)	1371.9(2)
1330.9(2)	1428.3(2)
1387.5(2)	1484.9(3)
1443.3(2)	1542.1(4)
1498.9(3)	
1555.1(4)	

analyzed.

4.3.3 Staggering

The staggering results are, of course, the most important results of this chapter. Figure 4.3 shows the staggering patterns extracted for ^{148}Eu(1) and ^{148}Gd(6), using the energies from Table 4.1. Also shown is the staggering pattern for ^{149}Gd(1), from [Fli93]. One is immediately struck by the presence of $\Delta I = 4$ bifurcation in both of the identical bands. This is remarkable because staggering is a relatively rare phenomenon. Chapter 5 will show many examples of bands that exhibit no staggering at all. This makes the occurrence of the phenomenon in three identical bands quite surprising. Although neither of these new examples persists over as large a range in

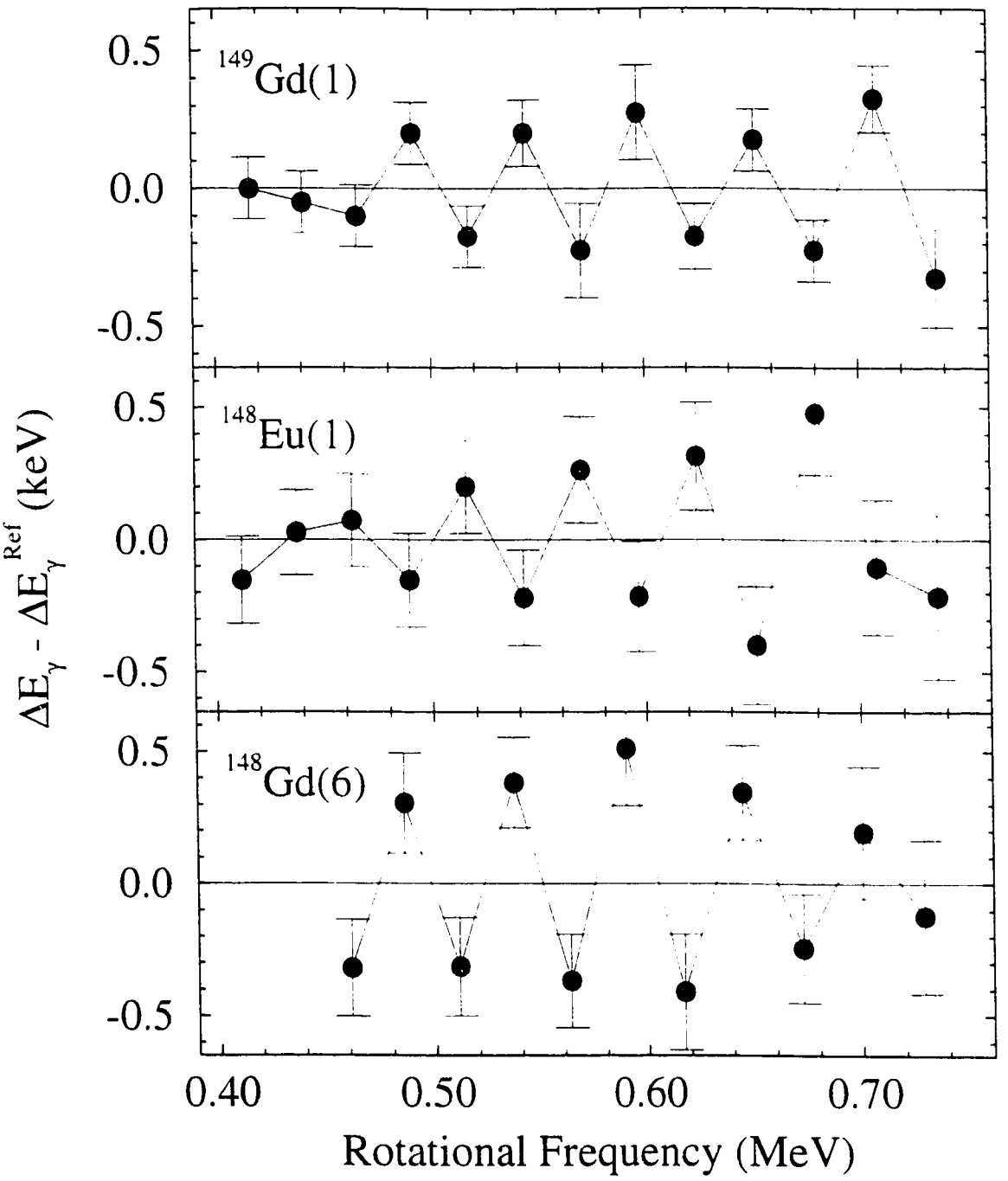

Figure 4.3: Staggering patterns for ^{148}Eu(1) and ^{148}Gd(6). That of ^{149}Gd(1) is also shown, for reference [Fli93].

spin as the ^{149}Gd(1) case, both are more convincing than any of the cases published by other authors.

The error bars in the staggering plots are derived from the statistical uncertainties reported by the GF2 fits. However, in claiming the existence of such small perturbations, one must be prepared to answer questions about the systematic uncertainties in the result. A variety of experimental issues have been raised about the validity of experiments claiming to see $\Delta I = 4$ bifurcation. The chief objection is that it is impossible to measure γ-ray energies to an accuracy of 0.1 keV, as claimed in Table 4.1. It has been argued that it is impossible to calibrate a γ-ray detector that well. In addition, it has been suggested that a non-linearity in the operation of the analog-to-digital converters (ADC's, devices that convert the current pulses in the germanium detectors into digitized energies) could produce staggering in the energies.

These concerns are largely unfounded. It should first be noted that staggering depends on differences of γ-ray energies. It is thus unnecessary to have an absolute calibration accurate to 0.1 keV. Varying the calibration coefficients (within reasonable bounds) has virtually no effect on a staggering plot.

Non-linearities in the ADC's cannot be responsible for the staggering phenomenon either. A given peak in a superdeformed band occurs at a different set of channels for each of the detectors. This occurs because the γ rays are Doppler-shifted due to the velocity of the nucleus, and because the signals from the detectors are not aligned anyway[¶]. As a result, a systematic non-linearity in the ADC's would be applied to a different energy for each detector. With one hundred detectors, these effects are completely washed out. It is also important to note that, as stated above,

[¶]Corrections for these effects are made in software.

many bands have been shown in this work to exhibit no staggering at all, suggesting that there are no systematic problems with the detector. The ^{149}Gd(1) staggering has also been measured with three different detector arrays [Haa90, Fli93, Viv96].

It is worth demonstrating at this time that the reported uncertainty in the energies is consistent with basic statistical arguments. Consider, for example the 1220 keV peak in ^{148}Eu(1). The full-width at half-maximum of this peak is measured to be 4.2 keV, corresponding to a standard deviation of 1.8 keV. The area of this peak is approximately 670 counts. If the peak was observed in the absence of background, elementary statistics asserts that the variance in the centroid is equal to the variance of the distribution divided by the area of the peak [Bev92]. This yields an uncertainty in the mean of 0.07 keV. However, this peak was observed on an effective background of approximately 2240 counts. Thus, the uncertainty should be scaled up by a factor of $\sqrt{(2240+670)/670} = \sqrt{2910/670}$ (consider the case where the background area is equal to the peak area, and generalize). Thus, the expected uncertainty in the centroid is 0.14 keV. This is smaller than the reported uncertainty of 0.17 keV. The larger uncertainty can be justified because the fit of the superdeformed band also allows the area of the peak to vary. Nevertheless, the reported uncertainties are no smaller than those that might be expected from simple statistical considerations.

The most likely source of systematic uncertainties is the background subtraction. This, more than any stage in the analysis, depends on the judgement of the experimenter. The experimenter must decide on the shape of the smooth Compton and continuum backgrounds, determine which superdeformed peaks are contaminated and how to fit these contaminating peaks. Even the ratio of smooth background to gated background in the subtraction is subject to the experimenter's discretion; it is felt that this is the dominant source of systematic uncertainty.

In order to make an estimate of the size of this uncertainty, a spectrum was prepared in which approximately five percent more gated background was subtracted than in the optimal spectrum. A spectrum was also prepared in which five percent less gated background was subtracted. In both cases, the amount of smooth background subtracted was adjusted to make the counts in the background channels sum to zero in the final spectrum. The five percent deviation was not completely arbitrary; at this level, the spectra no longer look properly background subtracted. These obviously over- and under-subtracted spectra were then fitted in the same way as described above, and a staggering plot was made. Figure 4.4 shows the results of this study. Shown is a staggering plot of ^{148}Gd(6); the filled circles are the same data as plotted in Figure 4.3 and the error bars are the statistical errors on these points. The upward- and downward-pointing triangles are the results of the analyses of the over- and under-subtracted spectra, respectively. This analysis is encouraging, in that it shows that in many cases, the results are virtually the same for all three cases, and it is rare that this systematic uncertainty is comparable to the statistical error bars. Therefore, one can safely neglect the systematic uncertainties from background subtraction.

The staggering results presented in this chapter certainly look non-statistical. However, it is important to ask what the probability is that a measurement of a perfectly regular band would yield a staggering plot like the ones shown here, simply as a result of statistical fluctuations. This question is not as easy to answer as one might imagine because the points on the staggering plot are so heavily correlated*. However, the analysis described below gives an answer to this question.

A computer program was written which takes as input ten consecutive transition energies (with their statistical uncertainties) from one of the bands. The energies

*Recall from Equation 2.21 that each point on a staggering plot depends on three ΔE_γ's, and therefore four γ-ray energies.

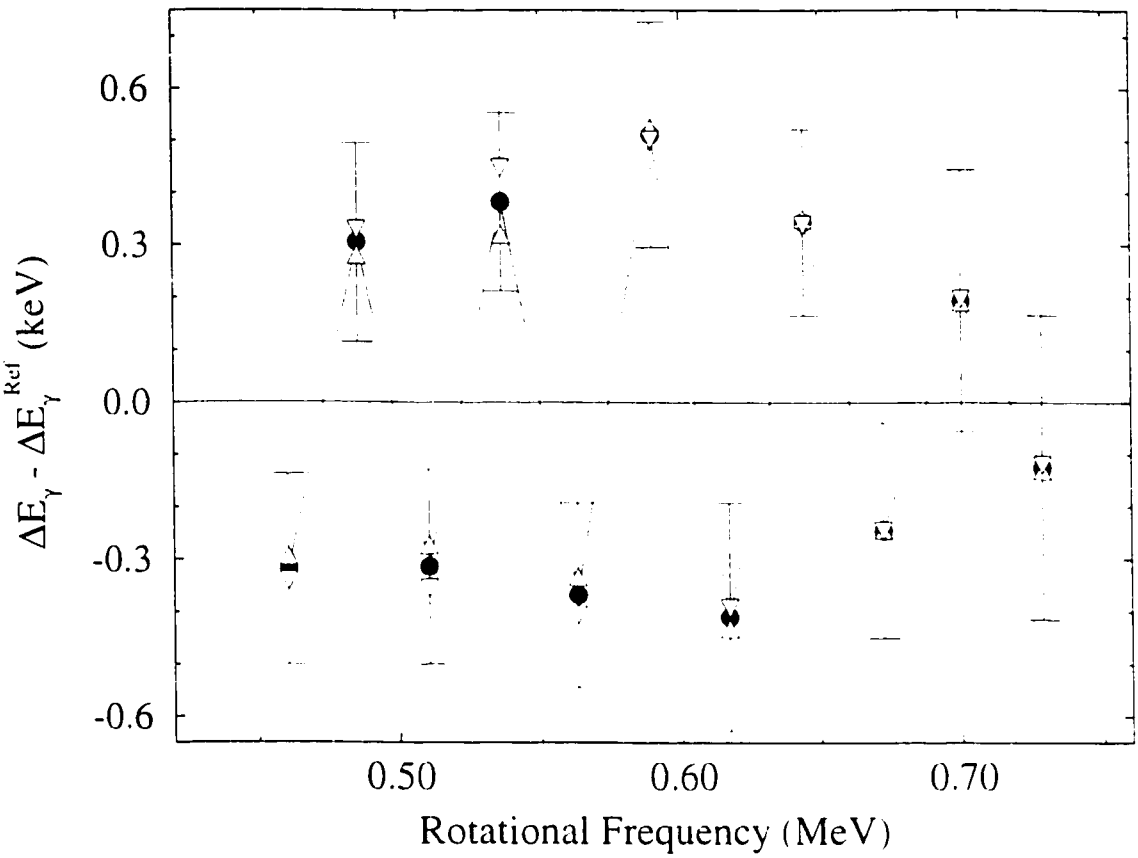

Figure 4.4: Systematic uncertainties in a staggering plot. The filled circles give the staggering data for ^{148}Gd(6) and the error bars show the statistical uncertainties in these points. The upward(downward)-pointing triangles show the results of the same analysis, but with an over(under)-subtracted spectrum.

are selected from a region centered at E_γ = 1200 keV. The program then produces 100000 copies of this band, with the transition energies in each copy randomized with Gaussian distributions with means and standard deviations equal to the measured transition energies and their uncertainties, respectively. For each copy, the seven staggering values x_i are calculated and the mean staggering $\bar{x}$ is calculated according

Table 4.2: Mean staggering $|X|$ and staggering significance Y for ^{149}Gd(1), ^{148}Eu(1), and ^{148}Gd(6). Also given is the probability P as defined in the text.

Band	Mean Staggering $\|X\|$ (keV)	Significance Y	Probability P
^{149}Gd(1)	0.21(9)	2.3	2.1%
^{148}Eu(1)	0.30(13)	2.3	2.1%
^{148}Gd(6)	0.37(12)	3.1	0.19%

to

$$\bar{r} = \frac{1}{7}\sum_{i=1}^{7}(-1)^i r_i. \tag{4.2}$$

The mean, $|X|$, and standard deviation σ_X of the distribution of $\bar{r}$'s is then calculated and output as the amount of staggering in the band (and its uncertainty).

The ratio $Y = |X|/\sigma_X$ is a measure of the significance of the result, in that the result differs by Y standard deviations from the null result (no staggering). One can report either this level of significance or the probability that a random sample from a standard normal distribution would yield a result with absolute value greater than Y (this can be found in tables in Bevington [Bev92] or virtually any statistics text). The probability, P, is exactly equal to the probability that a measurement of a band with no $\Delta I = 4$ bifurcation would produce a value of $|X|$ as large as that observed, answering the initial question.

The results of this analysis for the three bands in Figure 4.3 are shown in Table 4.2. In each case, the mean staggering $|X|$, the significance Y and the probability P are given. The table shows how unlikely it is that a measurement of a regular band would produce these results by chance. This issue is revisited in Section 5.5 after a more systematic survey of staggering in this mass region is performed.

4.4 Interpretation of the Staggering Results

4.4.1 Sinusoidal Staggering

The goal in performing this experiment was to see if there is any evidence that the model parameters of Hamamoto and Mottelson remain constant in the identical bands. This section examines this question.

In Hamamoto and Mottelson's model, the band staggering is proportional to $\cos(\frac{\pi}{2}(I - I_0))$. If the model parameters remain constant for identical bands, then the staggering results for ^{149}Gd(1), ^{148}Eu(1), and ^{148}Gd(6), when plotted as a function of spin, should all lie on a single cosine curve. One should, therefore, plot these data as a function of spin. However, as pointed out in Section 1.3, the spins of $A \sim 150$ superdeformed bands are not known, since no linking transitions have been found.

All is not lost, however. Because the relative single-particle structures of these superdeformed bands are understood, one can test the constancy of the model parameters without actually knowing the spins of any of the superdeformed bands.

Assuming that ^{149}Gd(1) has a $\pi 6^2 \nu 7^1$ intruder configuration with proton (neutron) orbitals filled up to the gap at $Z = 64$ ($N = 85$)[†], the signature of this band is $\alpha = -1/2$. That is, the spins of the levels are $2n - 1/2$, where n is an integer. Now consider the structure of ^{148}Eu(1). As stated at the beginning of this chapter, the structures of these two bands differ only by a proton in the negative-signature [301]1/2 proton orbital. This orbital contributes $-1/2$ to the nuclear angular momentum. Thus the corresponding ^{149}Gd(1) and ^{148}Eu(1) levels obey the relation

$$I(^{149}\text{Gd}(1)) = I(^{148}\text{Eu}(1)) - 1/2. \tag{4.3}$$

That is, the spins of the levels in ^{148}Eu(1) are $2n$. Similarly, the structure of ^{148}Gd(6)

[†]It is highly unlikely that this is wrong.

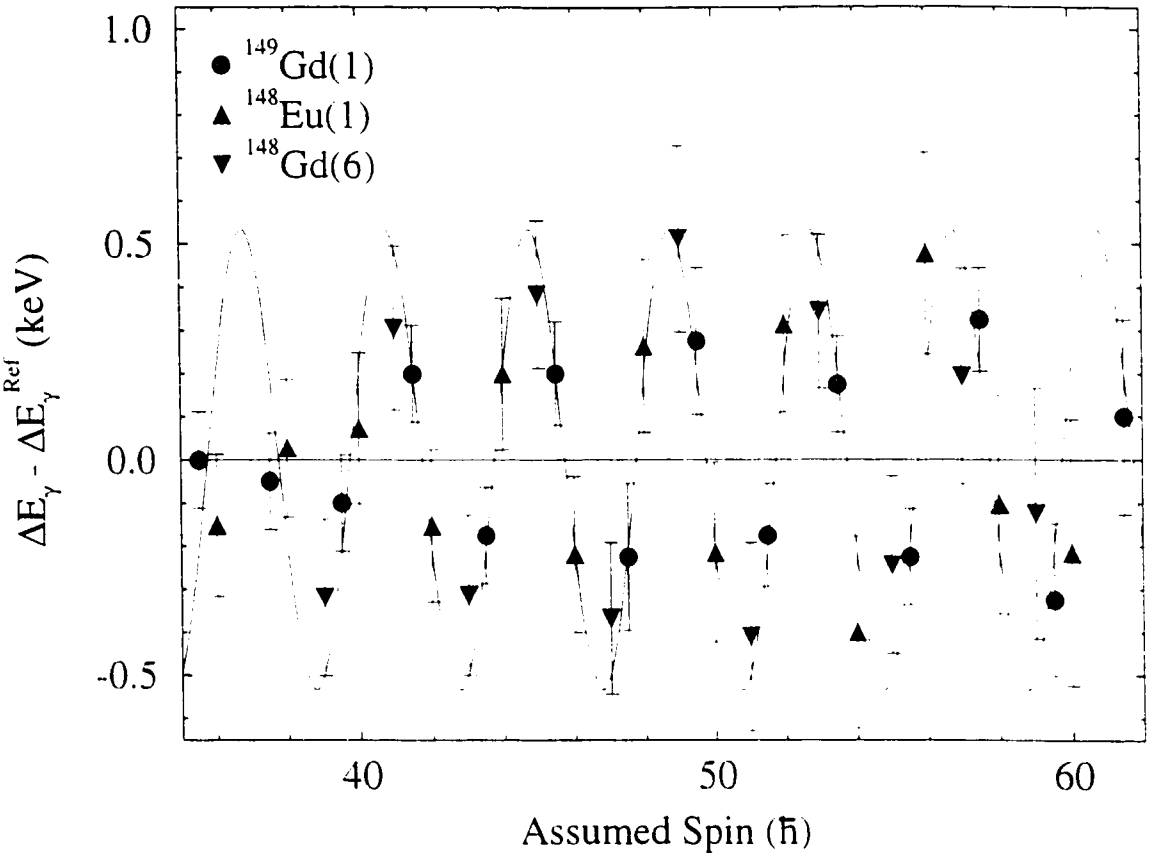

Figure 4.5: Staggering patterns for the three identical bands as a function of spin. A cosine is also plotted.

differs from ^{149}Gd(1) by a neutron in the positive-signature [411]1/2 orbital. Thus, the spins of the ^{148}Gd(6) levels obey

$$I(^{149}\mathrm{Gd}(1)) = I(^{148}\mathrm{Gd}(6)) + 1/2 \tag{4.4}$$

and so $I(^{148}\mathrm{Gd}(6)) = 2n - 1$.

The staggering patterns of the three bands are plotted as a function of spin in Figure 4.5. The spin assignments of Ragnarsson [Rag93] for ^{149}Gd(1) have been used instead of the generic $2n - 1/2$; this has no effect on this result. Over the spin range

where data from all three data sets are available, the cosine does a remarkable job of describing the data. At both higher and lower frequencies, the fit is considerably poorer; however, the results in Figure 4.5 suggest that the parameters are similar in the three bands.

The fit of this cosine to the data permits a constraint of some of the model parameters. As demonstrated in Appendix A, in this model the staggering is approximately proportional to $\cos(\frac{\pi}{2}(I - I_0))$, where I_0 is given by $\sqrt{A/4B_1}$. For these data, the fitted value of I_0 is (0.76 ± 0.08) mod 2. This parameter is further constrained in the next section.

4.4.2 A More Complete Description

Section 2.5.2 and Appendix A introduced the theory of Hamamoto and Mottelson. It was shown that if $I^2 > A/4B_1$, the action for tunneling between minima in their Hamiltonian acquires a real part. This real part produces a matrix element which oscillates with spin, and therefore an oscillating energy splitting, which manifests itself as staggering.

These discussions have ignored the imaginary part of the action. This is definitely a concern, however, since the imaginary part controls the amplitude of the staggering (apart from a constant factor). It is therefore interesting to ask whether one can learn anything by looking at the amplitude.

In Appendix B, the author examines the imaginary part of the action, and its effect on the amplitude of the staggering. Semi-classical arguments are used to derive an analytic expression for the staggering amplitude as a function of angular

momentum. This expression is

$$(\Delta E_\gamma - \Delta E_\gamma^{\rm ref}) = \frac{8A\hbar I^2}{\pi I_0} \frac{\left(\frac{I}{I_0} - 1\right)^{(I+I_0)/2}}{\left(\frac{I}{I_0} + 1\right)^{(I-I_0)/2}} \cos\left(\frac{\pi}{2}(I - I_0)\right). \qquad (4.5)$$

If the model parameters of Hamamoto and Mottelson are the same for all identical bands (as the results of the previous section suggest) and if these parameters are spin-independent (which also seems to be true, at least in the spin range plotted in Figure 4.5), then this expression can be fitted to extract values for the parameters.

This fit has been performed on the data. All data between $I = 37.5$ and $I = 61.5$ has been included. This omits the four lowest- and two highest-spin points in the ^{149}Gd(1) data set, and the lowest-spin point in the ^{148}Eu(1). There is no physical reason to exclude these points, but the data do not exhibit regular staggering in these regions, and so force the amplitude A to be too small. These regions are discussed later in this section.

The fit took the form of a grid search in I_0, with an exact solution for A at each value of I_0. All values of I_0 from 0.01 to 10.00, in steps of 0.01, were tested. For each, A was determined with an error-weighted average. It is apparent from the graphs in this chapter that the error bars on the staggering data are too large to strongly constrain the parameters. That is, the reduced χ^2 values for these fits were always much smaller than unity. However, much can still be learned from this fit.

Some of the best fits are shown in Figure 4.6. The analysis of the previous section revealed that the data are best fit by $I_0 \simeq 0.75$ mod 2. This analysis agrees in some sense, but also shows that only a small subset of the possible values of I_0 adequately fit the data. Figure 4.6 shows the staggering data as filled circles. Each panel also contains a solid curve, showing the best-fit $(\Delta E_\gamma - \Delta E_\gamma^{\rm ref})$ for I_0 equal to 0.75, 2.75, and 4.75. Both $I_0 = 0.75$ and $I_0 = 2.75$ do an excellent job of fitting the

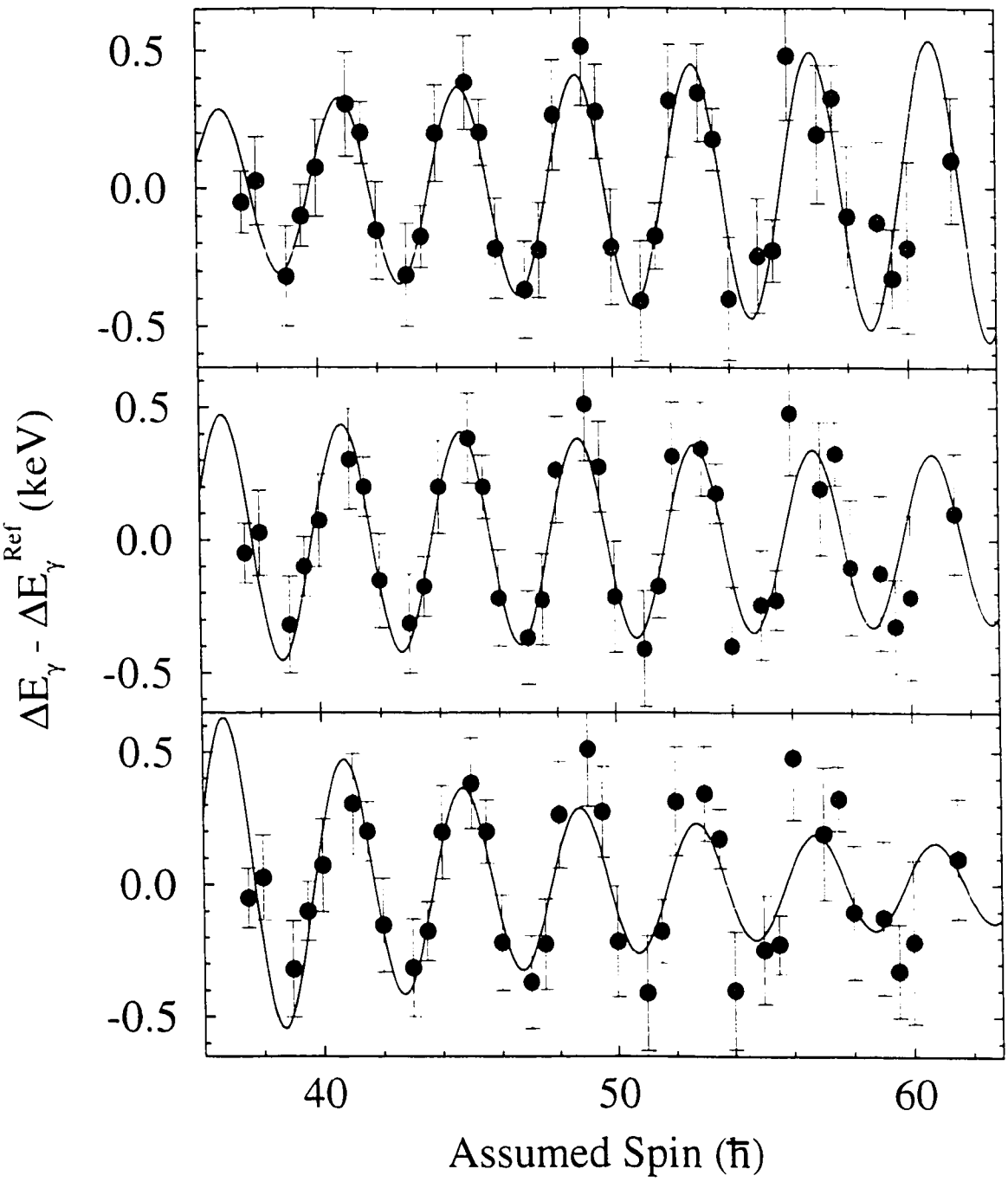

Figure 4.6: Good fits to the identical band staggering data. All three panels show the data from Figure 4.5. The upper, middle, and lower panels also show the best fit to these data with I_0 equal to 0.75, 2.75, and 4.75, respectively.

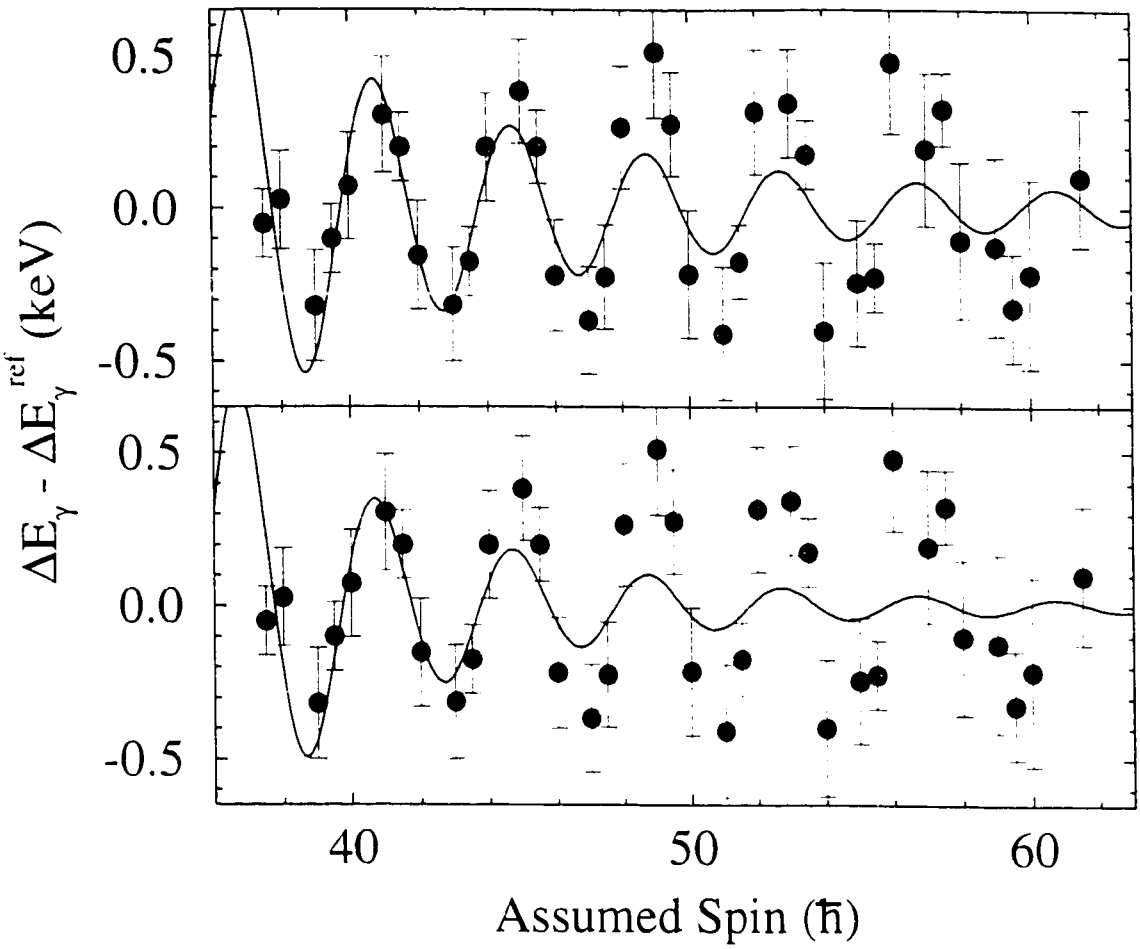

Figure 4.7: A similar set of graphs to those in Figure 4.6. Here, the upper and lower panels show the best fits to the data with I_0 equal to 6.75 and 8.75.

data. The $I_0 = 4.75$ fit is also acceptable, but the clear decrease in amplitude as a function of spin is opposite to the trend of the data. This is even more true of larger I_0 values. Figure 4.7 shows examples for $I_0 = 6.75$ and 8.75, demonstrating that 4.75 is the largest value of I_0 which can replicate the data.

One is now left with the inevitable question: what do these three possible values mean? Table 4.3 gives the values of A and B_1 corresponding to the three acceptable values of I_0. Also given is the approximate height of the barrier through

Table 4.3: A and B_1 values for the three possible I_0 solutions of the Hamamoto and Mottelson Hamiltonian. Also given is the height of the barrier separating the classically allowed regions at $I = 50\hbar$.

I_0	A	B_1	Barrier Height
0.75	2.6 eV	1.2 eV	7.2 MeV
2.75	7.4 keV	240 eV	1.5 GeV
4.75	1.6 MeV	18 keV	110 GeV

which the tunneling takes place (this is $B_1 I^4$ where I is taken to be $50\hbar$). Each I_0 corresponds to an (A, B_1) pair with energy scales that are orders of magnitude apart. Surely one can choose which set of parameters is correct based purely on hand-waving arguments.

Unfortunately, that appears not to be the case, largely because no one understands the origin of the staggering effect. Remember from Section 2.1 that the full particle-rotor Hamiltonian (not just the perturbation) has the form

$$H = \frac{\hbar^2}{2\mathcal{J}}(I(I+1) - 2I_3^2) + \epsilon + AI_3^2 + B_1(I_1^2 - I_2^2)^2 \tag{4.6}$$

where the Coriolis term has been neglected. The terms up to ϵ may be found in Equation 2.8, and the last two are suggested by Hamamoto and Mottelson.

For superdeformed bands, $\hbar^2/2\mathcal{J}$ is approximately 7 keV. It has been suggested [Ham94] that A should be "large" and positive compared to $\hbar^2/2\mathcal{J}$ so that the angular momentum remains perpendicular to the 3-axis, since a small value of A would make rotation around the 3-axis energetically favourable, contrary to what is observed. The $I_0 = 0.75$ solution (with $A = 2.6$ eV) does not satisfy this criterion. In other words, the single-particle part of the nuclear Hamiltonian must surely contain terms proportional to I_3^2 with coefficients much larger than 2.6 eV.

The solution $I_0 = 2.75$ is intriguing, since the corresponding A is approximately equal to $\hbar^2/2\mathcal{J}$. This makes it similar in size to the existing I_3^2 term in the particle-rotor model. The significance of this is not clear. It should again be noted that this A does not satisfy the requirement of Hamamoto and Mottelson that it be "large".

There is little to say about the $I_0 = 4.75$ solution. It seems incorrect, in the sense that 1.6 MeV is a large prefactor for a supposedly perturbative addition to the Hamiltonian. However, since I_3 remains as small as 0.5, this concern may be unfounded.

Before this section concludes, the issue of data exclusion from the fits should be re-addressed. Relatively little data has been excluded at high spins, and Flibotte [Fli97] has expressed reservations about the fits to the highest-energy peaks. As a result, this exclusion may not be so important. The exclusion at lower spins is more of a concern. Several data points have been left out of the fits, and it is clear that the staggering effect does not exist at these rotational frequencies (see Figure 4.3). This may indicate that one or more of the parameters of the Hamiltonian are spin-dependent. It has been noted [Fli93] that the alignment of the $N = 6$ protons at $\hbar\omega \simeq 0.4$ MeV occurs near the onset of the $\Delta I = 4$ bifurcation in ^{149}Gd(1). This could be an extremely important clue, although little has been made of it in the theoretical literature.

4.4.3 Implications for Pavlichenkov

Pavlichenkov has discussed [Pav97b] the significance of these results to his model. This discussion is summarized below.

In Pavlichenkov's model, one can determine whether a band will exhibit staggering by determining the sign of a quantity proportional to the proton and neutron

multipole moments, $Q_{44}(\pi)$ and $Q_{44}(\nu)$. If both Q's are positive, the nucleus exhibits staggering; if both are negative, the nucleus does not exhibit staggering. If the two have different signs, then the relative sizes of the terms matter.

For ^{149}Gd(1), $Q_{44}(\pi) < 0$ and $Q_{44}(\nu) > 0$ (see Figure 2.6). Pavlichenkov's calculation indicates that this band should not stagger, but uncertainties in this calculation make the prediction weak. However, Pavlichenkov points out that the contributions of low-j orbitals (such as the ($j = 1/2$) [301]1/2 or the ($j = 3/2$) [411]1/2) to the multipole moment are small. Therefore, if ^{149}Gd(1) staggers, then one should also expect its two identical bands to stagger, since these bands differ from ^{149}Gd(1) only in the occupation of low-j orbitals. This issue will be revisited in the next chapter.

It is also interesting to notice the frequency dependence of Q_{44}. Pavlichenkov's calculations show Q_{44} changing sign near $\hbar\omega \simeq 0.8$ MeV [Pav97a], causing the onset of staggering. Sign changes like this could cause the $\Delta I = 4$ bifurcation to begin abruptly at $I \simeq 37\hbar$, as observed (it should be noted that $I = 37\hbar$ corresponds to frequencies close to $\hbar\omega \simeq 0.4$ MeV).

The observation of correlated staggering patterns in these identical bands is interesting and provides a compelling reason to continue this analysis in other pairs of identical bands, and in other superdeformed bands in general. The next chapter presents such an analysis for the other superdeformed bands observed in this experiment, and in two other experiments performed with the Gammasphere array.

Chapter 5

Further Studies of Staggering

The results of the previous chapter are interesting and suggest that it would be worthwhile to make a more extensive study of the staggering effect in superdeformed bands in neighbouring nuclei, particularly identical bands. This chapter presents staggering analyses performed on the other superdeformed bands observed in GS-64, and in superdeformed bands observed in a second experiment performed by the McMaster group (GS-118), and in an experiment performed by Fallon and Beausang (GS-43) [Bea97].

5.1 Staggering in ^{148}Eu(2)

Analysis of the GS-64 data revealed an excited superdeformed band in ^{148}Eu. This band, called ^{148}Eu(2), is assigned the ^{149}Gd(1) configuration with a hole in the positive-signature $\pi[301]1/2$ orbital* (see Table 5.1 for ^{148}Eu band configurations). In light of the results obtained for ^{148}Eu(1), this band is an interesting case for study. In particular, the levels in this band have odd spins, so the staggering pattern should be the same as for ^{148}Gd(6), if it fits into the existing picture. Pavlichenkov would also expect this band to stagger, since it differs structurally from ^{149}Gd(1) only by a

*Note that in this chapter the signature of an orbital will often be indicated by a subscript (+) or (−) following the Nilsson numbers, for positive and negative signatures, respectively.

Table 5.1: Single-particle configurations for superdeformed bands in ^{148}Eu. The configurations are given relative to ^{149}Gd(1), which is $\pi 6^2 \nu 7^1$ and filled up to the proton and neutron shell gaps at particle numbers 64 and 85 (see Figure 4.1).

Band	Configuration relative to ^{149}Gd(1)	
	Protons	Neutrons
^{148}Eu(1)	$\{[301]1/2_{(-)}\}^{-1}$	...
^{148}Eu(2)	$\{[301]1/2_{(+)}\}^{-1}$	...

low-j hole.

Unfortunately, as the spectrum of this band in the upper panel of Figure 5.1 indicates, the statistics on this band are low. This makes it difficult to determine which peaks are contaminated by γ rays in the normal-deformed level scheme. And, although the oversubtracted peak at 1212 keV makes it clear that this spectrum is contaminated, it could not be determined from the background spectrum what the source of the contamination is. Therefore, no correction for contaminating lines has been made in the staggering analysis of this band.

It should also be noted that the background subtraction for this case was not performed with the operator formalism. Instead a fraction of a spectrum gated twice on the band and once on a set of background channels was used. Although this is not strictly correct, it is a decent approximation and reduces the statistical fluctuations in the final spectrum, making it preferable for weak bands.

The low statistics also produce huge error bars in the staggering plot, also shown in Figure 5.1 (the γ-ray energies are given in Table 5.2) with the ^{148}Gd(6) staggering pattern overlaid as a comparison. Although there is no evidence for staggering in this graph, the error bars are much too large to make a definitive statement at this time. The clear evidence in the staggering plot for a contaminated peak or a band

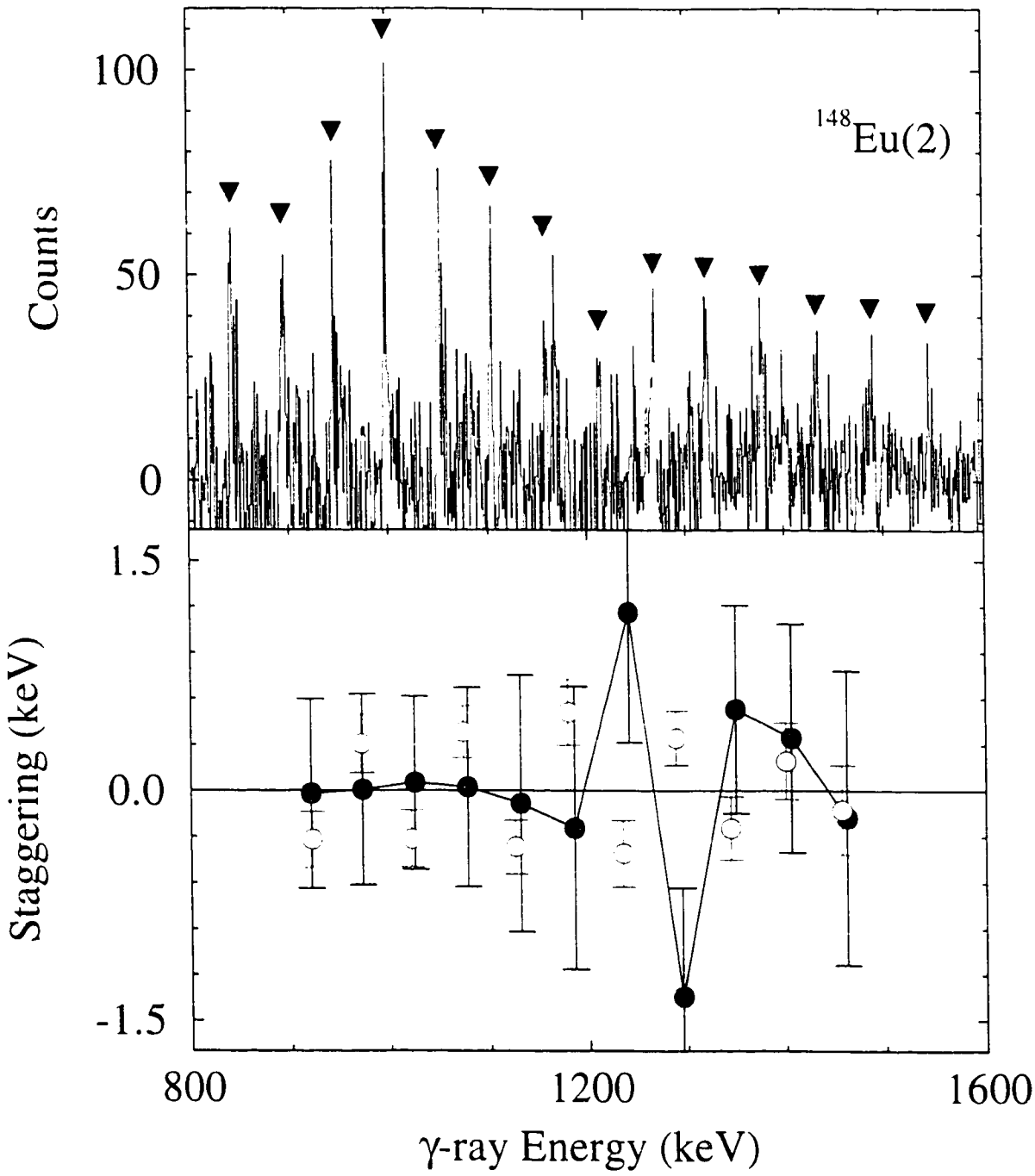

Figure 5.1: Upper panel: Partial γ-ray spectrum of ^{148}Eu(2). Lower panel: staggering plot for this band (filled circles), and ^{148}Gd(6) (open circles), for reference.

Table 5.2: Gamma-ray transition energies, in keV, of ^{148}Eu(2).

^{148}Eu(2)
844.2(6)
894.8(5)
946.1(6)
998.1(5)
1050.9(5)
1104.2(6)
1157.9(9)
1212.4(8)
1268.7(7)
1322.0(5)
1377.8(7)
1434.0(6)
1489.2(10)
1544.1(14)

crossing also complicates the conclusions.

5.2 Staggering in ^{147,148}Gd

5.2.1 Motivations

As mentioned in the previous chapter, the GS-64 experiment produced 1.8 billion events populating ^{147}Gd and ^{148}Gd. Both of these nuclei have been well-studied: ^{147}Gd has six known superdeformed bands [The96], and ^{148}Gd has nine† [Byr98]. However, prior to this work, $\Delta I = 4$ bifurcation has only been studied in one of these bands, ^{148}Gd(1) [deA96]. As a result, this experiment represents an excellent opportunity to do the first extensive study of the staggering in these bands.

The single-particle configurations assigned to the bands in ^{147,148}Gd are given

†Only the first six are studied in this thesis. The last three were reported near the completion of this work, and are likely too weak to analyze in this way with the GS-64 data set.

Table 5.3: Single-particle configurations for superdeformed bands in ^{147,148}Gd. The configurations are given relative to ^{149}Gd(1), which is $\pi 6^2 \nu 7^1$ and filled up to the proton and neutron shell gaps at particle numbers 64 and 85.

Band	Configuration relative to ^{149}Gd(1)	
	Protons	Neutrons
^{147}Gd(1)	...	$\{[651]1/2\}^{-2}$
^{147}Gd(2)	...	$\{[651]1/2_{(+)}\}^{-1}$ $\{[642]5/2_{(+)}\}^{-1}$
^{147}Gd(3)	...	$\{7_1\}^{-1}$ $\{[651]1/2_{(+)}\}^{-1}$
^{147}Gd(4)	...	$\{[651]1/2_{(+)}\}^{-1}$ $\{[411]1/2_{(+)}\}^{-1}$
^{147}Gd(5)	...	$\{[651]1/2_{(-)}\}^{-1}$ $\{[411]1/2_{(+)}\}^{-1}$
^{147}Gd(6)	$\{6_3\}$ $\{[301]1/2_{(-)}\}^{-1}$	$\{[651]1/2\}^{-2}$
^{148}Gd(1)	...	$\{[651]1/2_{(+)}\}^{-1}$
^{148}Gd(2)	...	$\{[651]1/2_{(-)}\}^{-1}$
^{148}Gd(3)	...	$\{7_1\}^{-1}$
^{148}Gd(4)	...	$\{[642]5/2_{(+)}\}^{-1}$
^{148}Gd(5)	$\{6_3\}\{6_4\}$ $\{[301]1/2\}^{-2}$	$\{7_2\}$ $\{[411]1/2\}^{-2}$
^{148}Gd(6)	...	$\{[411]1/2_{(+)}\}^{-1}$

in Table 5.3 [The96, deF95]. These configurations may be used to identify any particularly interesting cases related to the staggering phenomenon. For instance, the analysis of Chapter 4 suggests that holes in the $[301]1/2_{(-)}$ or $[411]1/2_{(+)}$ orbitals produce no change in the Hamamoto and Mottelson parameters. Pavlichenkov agrees that holes in these orbitals should neither produce nor destroy staggering. It would be interesting, therefore, to further examine the role of these orbitals with respect to the staggering phenomenon. Bands 4 and 5 in ^{147}Gd provide such an opportunity, when compared to ^{148}Gd(1,2). Band 6 in ^{147}Gd(6) is similarly interesting, if it could be compared to the band with the $[301]1/2_{(-)}$ orbital filled. However, this would be a band in ^{148}Tb, a nucleus in which no bands are known. The final example of this type is ^{148}Gd(5), which has the ^{152}Dy(1) structure with two holes in the [301]1/2 orbitals and two holes in the [411]1/2 orbitals.

The other bands differ from each other and from ^{149}Gd(1) in the occupation of $N = 6$ and $N = 7$ neutron orbitals. It would be interesting to discover whether any of these orbitals have any kind of systematic effect on the staggering. Such results could be very important in testing Pavlichenkov's model.

5.2.2 Bands Not Analyzed

Staggering is a subtle perturbation of the γ-ray energies of a superdeformed band. That one can observe this perturbation at all is due to the smoothness of the moments of inertia of these bands. Conversely, if the moment of inertia of a superdeformed band is not smooth, then the formulae used to extract the staggering are not as effective, and the $\Delta I = 4$ bifurcation is more difficult to identify.

Several bands in ^{147,148}Gd have quite irregular moments of inertia. This is due to the crossing of the negative-signature [651]1/2 and [642]5/2 Nilsson orbitals [The96], a topic not discussed in this work. When this crossing is not blocked, the moment of inertia changes so rapidly that it is impossible to extract a reliable staggering plot from the data. This is the case for ^{148}Gd(2), ^{147}Gd(1), ^{147}Gd(5), and ^{147}Gd(6). In all other cases, the crossing is blocked, the moment of inertia is smoother and the analysis can be done.

5.2.3 Results

The γ-ray energies of the superdeformed bands in ^{147,148}Gd analyzed in this work are given in Table 5.4 (except for ^{148}Gd(6), the energies of which were given in the previous chapter). The discussion will be broken up into sections according to the experimental motivations presented in Section 5.2.1

A primary motivation is to examine the effect of the [301]1/2 and [411]1/2 Nilsson orbitals. The first case in which this can be done consists of ^{148}Gd(1) and

Table 5.4: Gamma-ray transition energies of the superdeformed bands in ^{147,148}Gd.

^{147}Gd			^{148}Gd			
Band 2	Band 3	Band 4	Band 1	Band 3	Band 4	Band 5
729.9(1)	856.6(2)	934.5(4)	897.87(3)	875.1(2)	890.2(1)	899.7(1)
778.34(7)	910.6(2)	988.2(2)	950.33(3)	924.9(1)	938.6(1)	944.7(1)
827.71(6)	966.3(2)	1041.9(3)	1003.71(5)	975.6(1)	988.4(1)	991.5(1)
877.46(6)	1022.1(3)	1096.5(2)	1058.39(4)	1027.3(1)	1039.4(1)	1038.2(1)
928.77(5)	1079.5(1)	1152.9(2)	1114.21(3)	1079.7(1)	1091.4(1)	1084.8(1)
981.31(5)	1137.3(2)	1210.2(4)	1170.76(4)	1132.7(1)	1144.4(1)	1131.9(1)
1035.32(5)	1194.9(2)	1267.7(2)	1227.94(3)	1186.2(1)	1198.0(1)	1179.0(1)
1090.28(5)	1252.7(2)	1325.9(2)	1285.68(4)	1239.7(1)	1252.9(1)	1226.8(1)
1146.26(5)	1310.4(2)	1384.7(4)	1344.06(4)	1292.8(2)	1308.2(2)	1274.3(1)
1203.44(6)	1367.6(2)	1444.4(4)	1402.87(5)	1344.8(2)	1364.3(2)	1322.2(1)
1261.37(6)	1423.3(3)		1461.78(6)	1395.0(2)	1421.2(2)	1369.3(1)
1320.08(7)	1476.9(4)		1520.92(8)		1479.1(2)	1417.4(2)
1379.55(8)			1580.2(1)		1537.2(3)	1464.8(2)
1439.6(1)			1639.5(2)		1597.3(6)	1513.0(3)
1500.2(2)						1560.7(7)
						1609(1)

^{147}Gd(4), identical bands which differ in structure by a neutron in the positive-signature [411]1/2 orbital. A discussion of these data is deferred to Section 5.3, where the results for a third identical band are presented.

The second case is ^{148}Gd(5), an identical band to ^{152}Dy(1). As shown in Figure 5.2, this band exhibits a regular staggering pattern, with a statistical significance of 2.8 standard deviations from the null result. Band 1 in ^{152}Dy shows no evidence of $\Delta I = 4$ bifurcation [Fli93], in accordance with Pavlichenkov's predictions. However, in this model, bands differing only by particles in low-j orbitals should have similar staggering behaviour; the differing results for ^{152}Dy(1) and ^{148}Gd(5) cannot be reconciled with this model. The model of Hamamoto and Mottelson is difficult to test, since it makes few predictions. However, an idea developed in Chapter 4

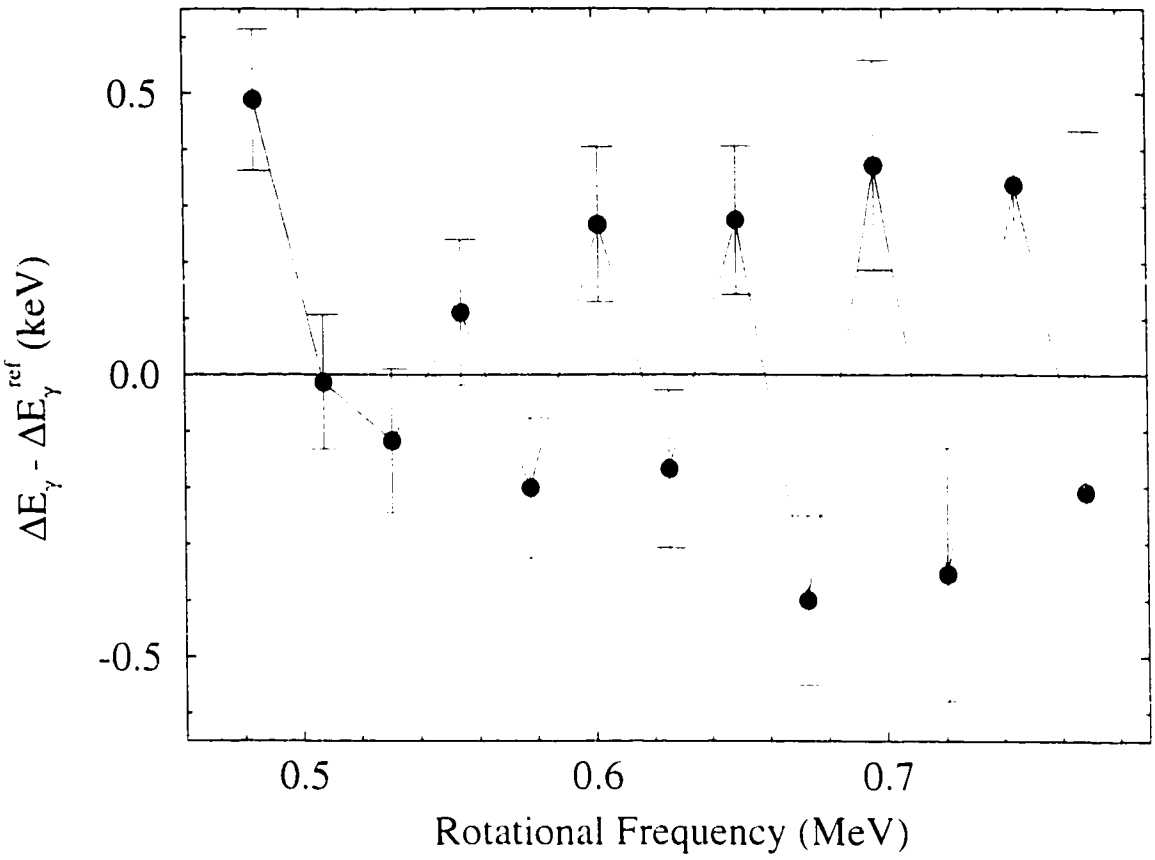

Figure 5.2: The effect of the [301]1/2 and [411]1/2 Nilsson orbitals on staggering. Shown is the staggering pattern of ^{148}Gd(5), a band identical to ^{152}Dy(1).

that the model parameters are unchanged by the [301]1/2 and [411]1/2 orbitals, a "constant-parameter extension" of the model is more testable. It also fails the test, since both ^{148}Gd(5) and ^{152}Dy(1) must have the same staggering plot if both bands have the same spins, as the configuration assignment predicts. Perhaps the constant-parameter extension should only apply to the $\pi[301]1/2_{(-)}$ orbital and not to the other signature.

Another area of interest is the effect of $N = 7$ neutron orbitals on $\Delta I = 4$ bifurcation. Figure 5.3 shows the staggering plot of ^{148}Gd(3), which differs from

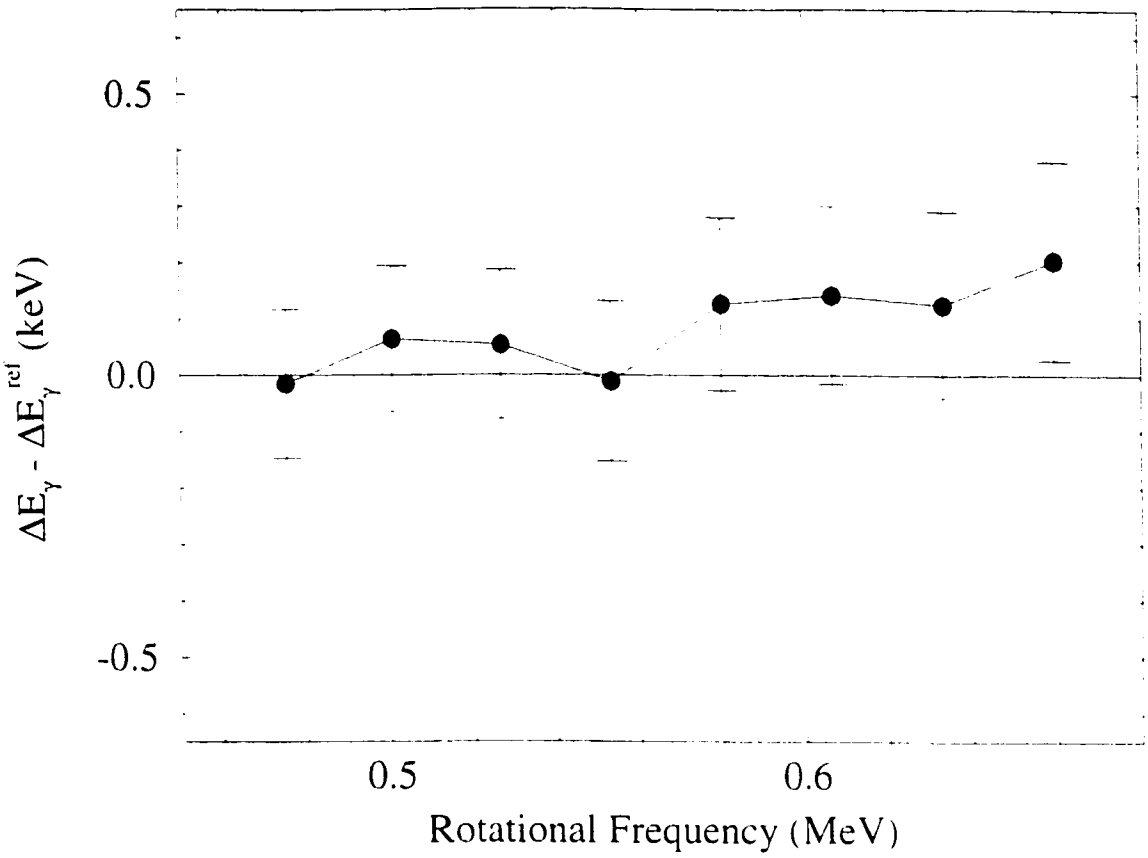

Figure 5.3: Staggering plot of ^{148}Gd(3), showing the effect of the 7_1 intruder on $\Delta I = 4$ bifurcation.

^{149}Gd(1) only in the occupation of the 7_1 intruder. The plot shows clearly that ^{148}Gd(3) does not stagger. This result is in accord with Pavlichenkov's model. Without any $N = 7$ orbitals occupied, the Q_{44} moment of ^{148}Gd(3) should be dominated by the contribution from its two $N = 6$ protons. Pavlichenkov shows this contribution to be negative, indicating that ^{148}Gd(3) should exhibit no staggering.

Finally, there is the role of $N = 6$ neutron orbitals in the staggering phenomenon. Figure 5.4 shows staggering plots for four superdeformed bands in ^{147,148}Gd. All of these bands differ from ^{149}Gd(1) by one or two $N = 6$ neutron orbitals, and

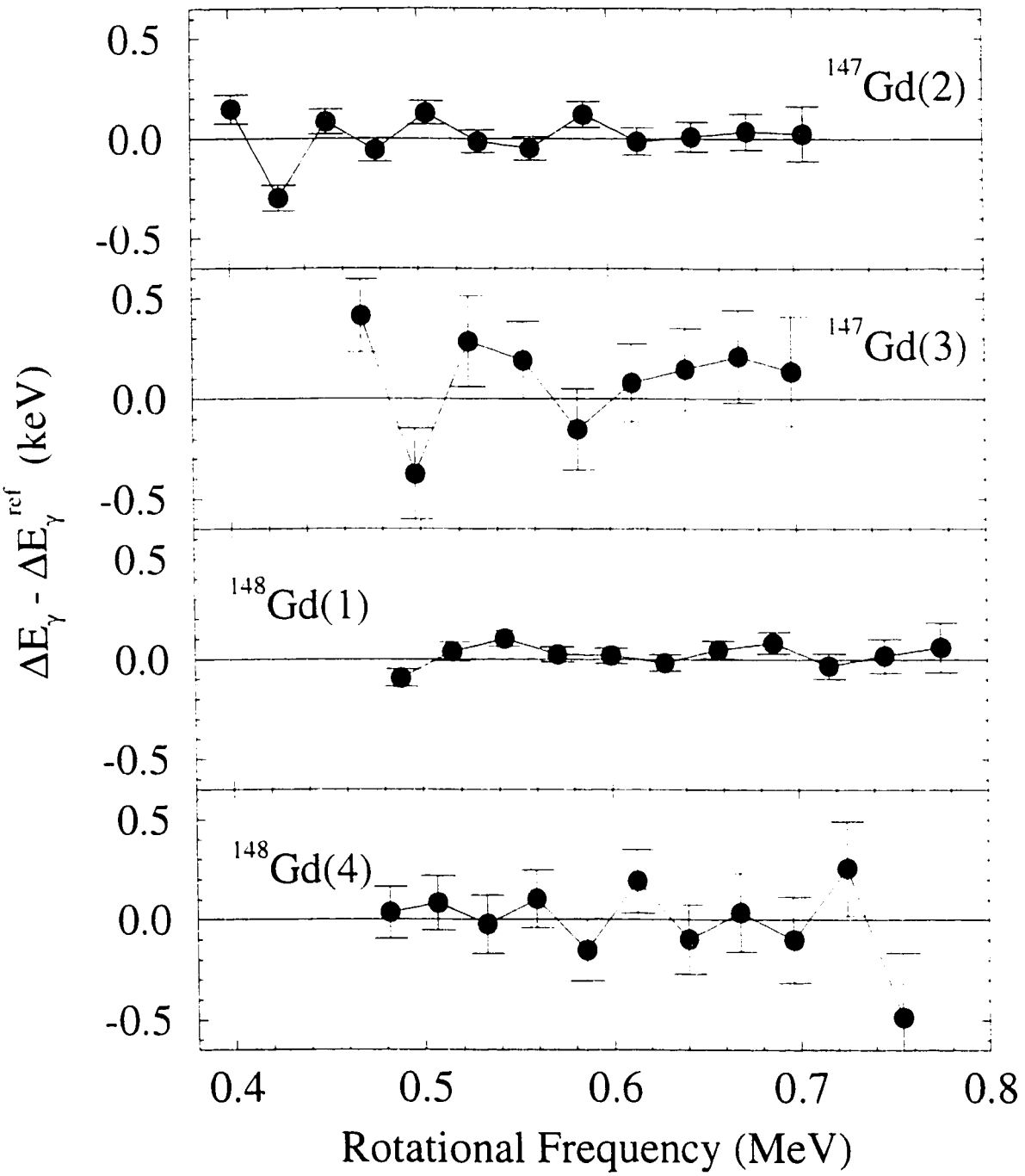

Figure 5.4: The effect of $N = 6$ neutron orbitals on staggering. All of the bands shown differ in structure from ^{149}Gd(1) by one or two $N = 6$ neutrons.

none of them exhibits statistically significant $\Delta I = 4$ bifurcation. The absence of staggering in ^{148}Gd(1) is in contradiction with the tentative result of [deA96]. These four cases provide a (somewhat complicated) test of the Pavlichenkov model. The $[651]1/2_{(+)}$ orbital is the second occupied orbital in the $1i_{11/2}$ subshell. The $[642]5/2_{(+)}$ orbital is the sixth occupied orbital in the $1i_{13/2}$ subshell. As such, both serve to decrease Q_{44} at frequencies above 0.5 MeV and holes in these orbitals should increase Q_{44}[§]. One thus expects all of the bands in Figure 5.4 to exhibit $\Delta I = 4$ bifurcation[¶] (with the possible exception of ^{147}Gd(3), which also has a hole in the 7_1 intruder, relative to ^{149}Gd(1)). Figure 5.4 demonstrates that none of these bands stagger, in contradiction with the predictions.

5.3 Staggering in ^{147}Eu

Two bands identical to ^{149}Gd(1) were studied in Chapter 4. Both have similar structures to ^{149}Gd(1), but ^{148}Eu(1) has a hole in the $\pi[301]1/2_{(-)}$ Nilsson orbital and ^{148}Gd(6) has a hole in the $\nu[411]1/2_{(+)}$ orbital. An obvious next step is to study the band with holes in both of these orbitals.

This band is in ^{147}Eu and should be at an excitation energy, relative to the yrast band, comparable to that of ^{148}Gd(6). As a result, a data set comparable in size to that obtained for ^{148}Gd should be required to study this band. In practical terms, this means that the nucleus must be populated in a neutrons-only evaporation channel. The only reaction employing stable beams and targets which can produce ^{147}Eu at a spin and excitation energy suitable for a study of superdeformation is a beam of ^{23}Na on a target of ^{130}Te. The McMaster group proposed this experiment,

[§]It is important for this argument that both orbitals produce the same effect, since they become so heavily mixed in the superdeformed bands

[¶]Note that the conclusions drawn in this discussion are at variance with those drawn by Pavlichenkov in Reference [Pav97b].

and performed it in July 1997 at the Lawrence Berkeley National Laboratory with the Gammasphere array. For this experiment, named GS-118, Gammasphere comprised 103 germanium detectors. The beam energy was 145 MeV, and two stacked 500 $\mu g/cm^2$ foils of ^{130}Te were used as targets, each evaporated on a similar thickness of gold for support.

The experiment led to the observation of five superdeformed bands in ^{147}Eu, although none of them have been assigned the configuration described above. Why this band was not observed is not clear. As discussed in Reference [Has98b], several bands have been observed in ^{147}Eu with structures that have no analogue in ^{148}Gd. This seems to spread the superdeformed band intensity in ^{147}Eu over more bands than in ^{148}Gd, leading to smaller relative intensities in ^{147}Eu bands than one might expect by looking at the intensities of analogous bands in ^{148}Gd. This could put the intensity of the desired band below the detection threshold. It is also possible that the intensity is smaller than expected because ^{147}Eu is simply too far away from the superdeformed closed shell ^{152}Dy, making superdeformed structures less favoured at high spins.

The single-particle configurations of the five observed bands are given in Table 5.5 (the configuration for band 5 is tentative). The justifications for these configurations are summarized in Reference [Has98b]. A number of these bands are interesting cases for study. Bands 1 and 5 differ from the ^{148}Gd yrast band by a hole in one of the [301]1/2 orbitals, thus providing another opportunity to study the effect of these orbitals on the staggering. The other bands have different intruder configurations and provide additional tests of Pavlichenkov's model.

Most of these bands have pronounced irregularities in their moments of inertia. Bands 2 and 3 show a dramatic increase in $\mathcal{J}^{(2)}$ at high frequency, while band 4 shows

Table 5.5: Single-particle configurations for superdeformed bands in ^{147}Eu. The configurations are given relative to ^{149}Gd(1), which is $\pi 6^2 \nu 7^1$ and filled up to the proton and neutron shell gaps at particle numbers 64 and 85. Although bands 2, 3, and 4 change configurations at high frequencies, only the low frequency configurations are given.

Band	Configuration relative to ^{149}Gd(1)	
	Protons	Neutrons
^{147}Eu(1)	$\{[301]1/2_{(-)}\}^{-1}$	$\{[651]1/2_{(+)}\}^{-1}$
^{147}Eu(2)	$\{6_2\}^{-1}$	$\{[651]1/2_{(+)}\}^{-1}$
^{147}Eu(3)	$\{6_2\}^{-1}$	$\{[651]1/2_{(-)}\}^{-1}$
^{147}Eu(4)	$\{6_3\}\ \{[301]1/2\}^{-2}$	$\{[651]1/2_{(-)}\}^{-1}$
^{147}Eu(5)	$\{[301]1/2_{(+)}\}^{-1}$	$\{[651]1/2_{(-)}\}^{-1}$

a dramatic decrease at the same frequency. This decreases the range over which their staggering can be measured and, combined with the extensive contamination of bands 2 and 4 by transitions in the normal-deformed level scheme, prevents the production of a staggering plot for bands 2 and 4. Band 5 has a large, unexplained irregularity at around 1200 keV, which also destroys any chance of producing a staggering plot for this band.

The transition energies of the two bands that could be analyzed are given in Table 5.6, and the staggering plots are in Figure 5.5. Neither of these bands exhibits any $\Delta I = 4$ bifurcation. In the case of band 3, this disagrees with the prediction of Pavlichenkov. In Pavlichenkov's model, the first particle in a high-j subshell always makes a positive contribution to the Q_{44} moment. Band 3, with only one $N = 6$ proton intruder and one $N = 7$ intruder, must have a substantial positive Q_{44}, and should be expected to stagger. The experimental evidence shows no staggering at all.

The failure of the Pavlichenkov model to predict the occurrence of staggering for bands with the $\pi 6^2 \nu 7^1$ intruder configuration has been well documented in this

Table 5.6: Gamma-ray transition energies, in keV, for bands in ^{147}Eu.

Band 1	Band 3
892.4(1)	772.4(3)
946.8(1)	835.7(2)
1001.3(1)	898.9(2)
1056.3(1)	961.9(2)
1112.5(1)	1025.0(2)
1169.3(1)	1087.6(2)
1226.6(1)	1149.9(2)
1284.2(1)	1200.4(0)
1342.7(1)	1207.8(0)
1401.6(2)	1212.2(4)
1460.5(2)	1271.6(2)
1519.3(3)	1329.8(3)
1578.5(4)	
1637.5(8)	

chapter, and there is little point in going into any further detail about the failure of the model in the case of ^{147}Eu(1). However, the measurement of the staggering in this band permits an interesting comparison. The upper panel of Figure 5.6 shows the familiar staggering patterns of ^{149}Gd(1), ^{148}Eu(1), and ^{148}Gd(6), plotted as a function of angular momentum, as was illustrated in Figure 4.5. The latter two bands are related structurally to the first by holes in the proton $[301]1/2_{(-)}$ and neutron $[411]1/2_{(+)}$ orbitals, respectively. The correlation between the three staggering patterns is remarkable, and inspires further investigation into the role of these orbitals as regards the staggering phenomenon.

The lower panel of Figure 5.6 is the analogous plot for ^{148}Gd(1) and its two identical bands, ^{147}Eu(1) and ^{147}Gd(4). Each band differs from one in the upper panel only by a neutron in the [651]1/2 Nilsson orbital (the pairs are plotted with the same symbols). It is clear that none of the bands in the lower panel exhibit any

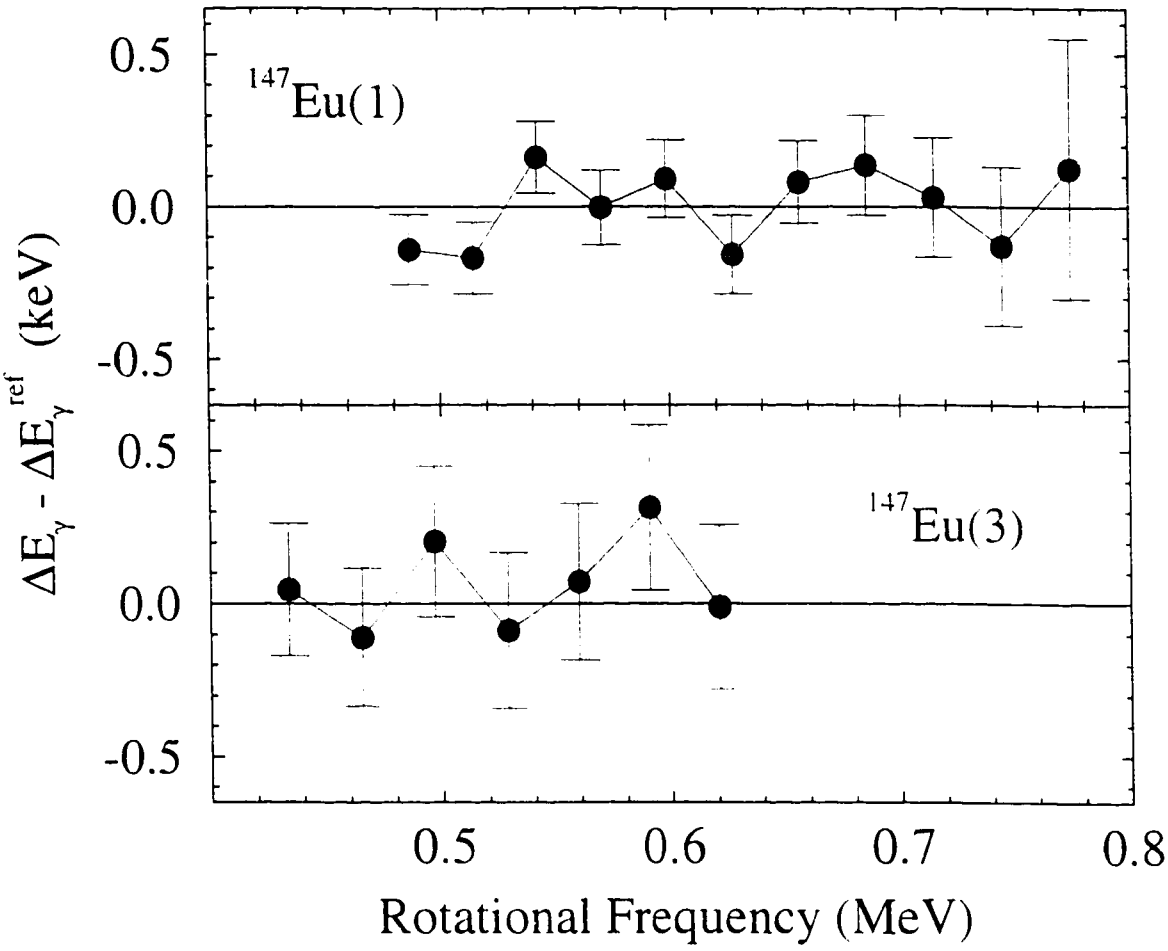

Figure 5.5: Staggering plots for bands in ^{147}Eu.

$\Delta I = 4$ bifurcation. This figure demonstrates two very important requirements of a model attempting to explain the phenomenon of $\Delta I = 4$ bifurcation. The model must explain

1. why the $\pi[301]1/2_{(-)}$ and $\nu[411]1/2_{(+)}$ holes preserve the staggering effect in the nuclei depicted in the upper panel, and

2. why so many orbitals, including the $\nu[651]1/2_{(+)}$ orbital illustrated here, completely destroy the effect.

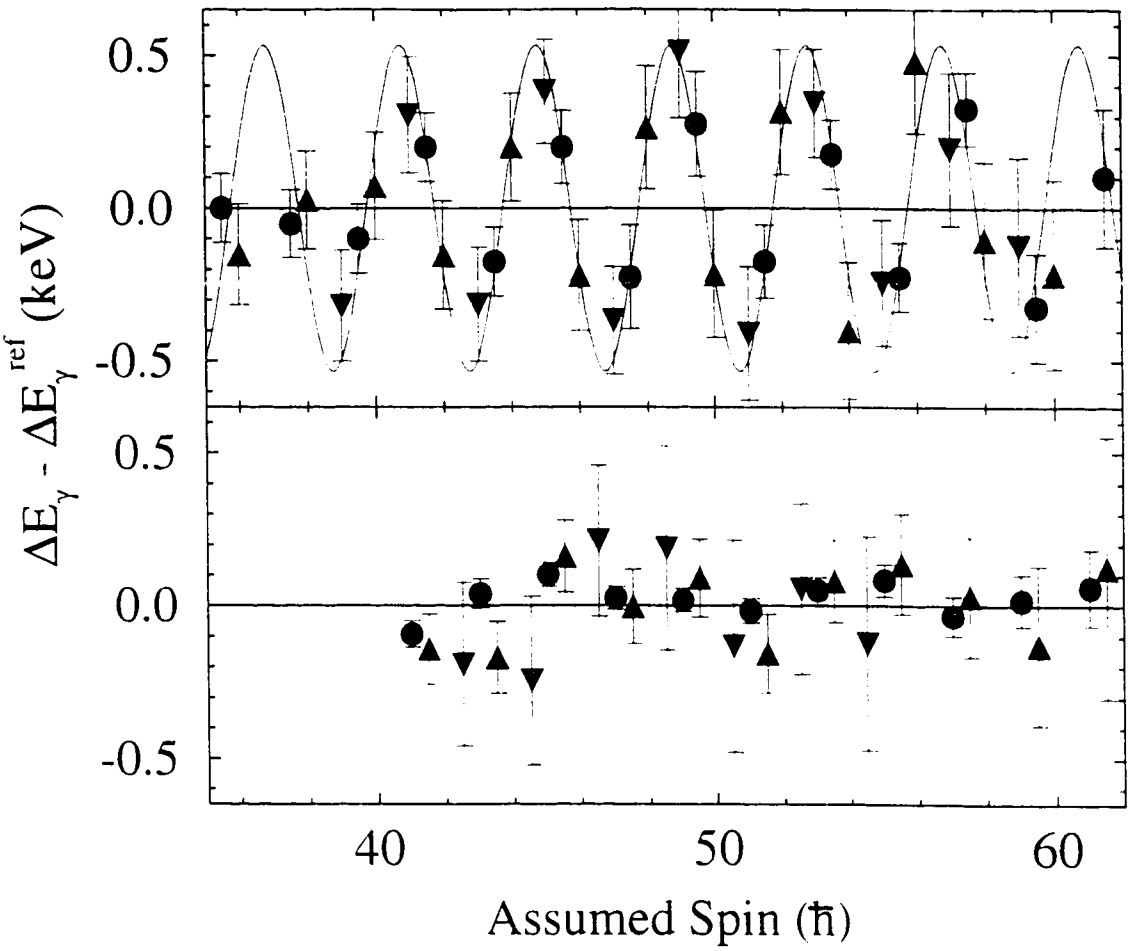

Figure 5.6: Staggering plots as a function of spin. In the upper panel, the circles, upward-pointing triangles, and downward pointing triangles represent the data for the well-known cases ^{149}Gd(1), ^{148}Eu(1), and ^{148}Gd(6), respectively. In the lower panel are the analogous cases, lacking the positive-signature [651]1/2 orbital. These are ^{148}Gd(1), ^{147}Eu(1), and ^{147}Gd(4), respectively.

Neither of the models described in this thesis are up to this challenge. The failure of Pavlichenkov's model for $N = 6$ neutrons has already been explored in Section 5.2.3. Hamamoto and Mottelson's model fares even worse. The lack of a physical basis for their model gives them no predictive power regarding any orbitals.

5.4 Staggering in ^{150,151}Gd

For several years, ^{149}Gd(1) represented the only convincing example of a superdeformed band exhibiting $\Delta I = 4$ bifurcation. Chapter 4 presented the surprising result that two bands identical to ^{149}Gd(1) also stagger. This makes a study of other superdeformed bands identical to ^{149}Gd(1) highly desirable.

The only other known identical bands to ^{149}Gd(1) are in ^{150}Gd. Bands 4a and 4b*, first reported in 1993[Bea93], have transition energies at the 1/4 and 3/4 points of ^{149}Gd(1). They are interpreted as having the ^{149}Gd(1) structure, with the eighty-sixth neutron occupying the strongly-coupled [402]5/2 orbitals (see Table 5.7).

A high-statistics study of ^{150}Gd and ^{151}Gd was performed by Fallon and Beausang in early 1996. This experiment, named GS-43, was performed with Gammasphere comprising 84 germanium detectors at the Ernest O. Lawrence Berkeley National Laboratory. A beam of ^{26}Mg was incident on a target of ^{130}Te, with ^{151}Gd and ^{150}Gd populated in the $5n$ and $6n$ evaporation channels, respectively. In this study, fourteen bands were seen in ^{150}Gd and six in ^{151}Gd†. The data from this experiment have been obtained from Fallon and Beausang [Bea97] in order to study staggering in these bands.

The single-particle configurations [Ert98] of the studied bands are given in Table 5.7. In addition to bands 4a and 4b, discussed above, these nuclei offer a number of interesting cases. Bands 6a and 6b, also in ^{150}Gd, are a second pair of signature partner bands identical to ^{149}Gd(1) with band 6b virtually isospectral to

*Originally labelled bands 3 and 4 in Reference [Bea93]. The notation used in this thesis is that of [Ert98].

†In this thesis, only ten are studied in ^{150}Gd and four in ^{151}Gd. The others are either extremely weak or without a configuration assignment.

Table 5.7: Single-particle configurations for superdeformed bands in ^{150,151}Gd. The configurations are given relative to ^{149}Gd(1), which is $\pi 6^2 \nu 7^1$ and filled up to the proton and neutron shell gaps at particle numbers 64 and 85. The signature assignments of ^{150}Gd(6a,6b) are not certain.

Band	Configuration relative to ^{149}Gd(1)	
	Protons	Neutrons
^{150}Gd(1)	...	$\{7_2\}$
^{150}Gd(2)	$\{6_3\}\{6_4\}\{[301]1/2\}^{-2}$	$\{7_2\}$
^{150}Gd(3)	$\{6_3\}\ \{[301]1/2_{(-)}\}^{-1}$	$\{7_2\}$
^{150}Gd(4a)	...	$\{[402]5/2_{(-)}\}$
^{150}Gd(4b)	...	$\{[402]5/2_{(+)}\}$
^{150}Gd(5)	...	$\{7_3\}$
^{150}Gd(6a)	...	$\{[521]3/2_{(+)}\}$
^{150}Gd(6b)	...	$\{[521]3/2_{(-)}\}$
^{150}Gd(8a)	$\{6_3\}\ \{[301]1/2_{(-)}\}^{-1}$	$\{[402]5/2_{(+)}\}$
^{150}Gd(8b)	$\{6_3\}\ \{[301]1/2_{(-)}\}^{-1}$	$\{[402]5/2_{(-)}\}$
^{151}Gd(1a)	...	$\{7_2\}\{[402]5/2_{(+)}\}$
^{151}Gd(1b)	...	$\{7_2\}\{[402]5/2_{(-)}\}$
^{151}Gd(3a)	...	$\{7_2\}\{[521]3/2_{(-)}\}$
^{151}Gd(3b)	...	$\{7_2\}\{[521]3/2_{(+)}\}$

^{149}Gd(1). The other bands in ^{150}Gd have a number of different proton and neutron intruder configurations, which could provide tests of Pavlichenkov's predictions. In ^{151}Gd, all of the bands have the $\pi 6^2 \nu 7^2$ intruder configuration, with the 87th neutron occupying one of several strongly-coupled orbitals. Thus, all of these bands are very similar to ^{150}Gd(1), and might provide interesting comparisons.

Unfortunately, not all of the bands in these data could be analyzed in this investigation. Bands 3, 4a, and 8b in ^{150}Gd have large irregularities in their moments of inertia which prevent the calculation of a smooth reference. Band 5 in ^{150}Gd, and band 3b in ^{151}Gd are too contaminated by peaks from the normal-deformed level scheme to permit this kind of analysis.

Table 5.8: Gamma-ray transition energies, in keV, for bands in ^{150}Gd.

Band 1	Band 2	Band 4b	Band 6a	Band 6b	Band 8a
849.50(2)	1047.27(7)	860.77(6)	879.7(2)	807.26(8)	875.3(2)
888.26(2)	1097.90(8)	911.23(6)	930.5(1)	855.83(8)	924.8(2)
929.23(2)	1148.84(8)	963.20(7)	982.2(1)	906.12(7)	974.8(2)
971.26(2)	1200.14(9)	1015.51(8)	1034.7(1)	957.07(12)	1025.7(2)
1013.78(2)	1251.15(9)	1068.76(8)	1088.0(3)	1008.61(8)	1077.3(2)
1056.78(3)	1301.48(10)	1122.65(9)	1141.3(2)	1061.06(9)	1129.6(2)
1100.38(3)	1351.52(10)	1177.51(11)	1195.8(2)	1114.04(11)	1182.4(2)
1144.95(3)	1401.26(13)	1232.70(10)	1251.0(2)	1168.06(20)	1236.4(2)
1190.76(3)	1450.34(17)	1288.25(11)	1306.5(2)	1222.61(11)	1290.7(2)
1238.09(3)	1498.89(28)	1344.28(11)	1363.0(2)	1278.39(13)	1345.4(2)
1286.84(3)	1548.36(48)	1401.00(14)	1419.1(2)	1333.91(17)	1400.5(3)
1336.86(4)		1457.57(18)	1475.9(3)	1390.22(22)	1456.3(5)
1388.10(5)		1514.14(25)	1533.2(4)	1446.90(28)	
1440.31(7)		1569.66(49)	1589.7(10)	1503.82(47)	
1493.07(10)				1560.27(93)	
1547.47(24)					

The transition energies measured in the rest of the bands in this data set are given in Tables 5.8 and 5.9. As in the previous section, the discussion of this large quantity of data is broken down according to the experimental motivations.

The first area of interest is the bands in ^{150}Gd that are identical to ^{149}Gd(1). Figure 5.7 shows the staggering patterns of these bands. Neither band 4b nor band 6a exhibit $\Delta I = 4$ bifurcation. This implies that the constant-parameter extension to the model of Hamamoto and Mottelson does not apply to the $[402]5/2_{(+)}$ or $[521]3/2_{(+)}$ orbitals. The staggering results disagree with the predictions of Pavlichenkov. The neutrons that have been added to the ^{149}Gd(1) system in these two bands are in small-j ($d_{5/2}$ and $f_{7/2}$) orbitals. As a result, they should have little effect on the staggering and one would expect that both of these bands should stagger.

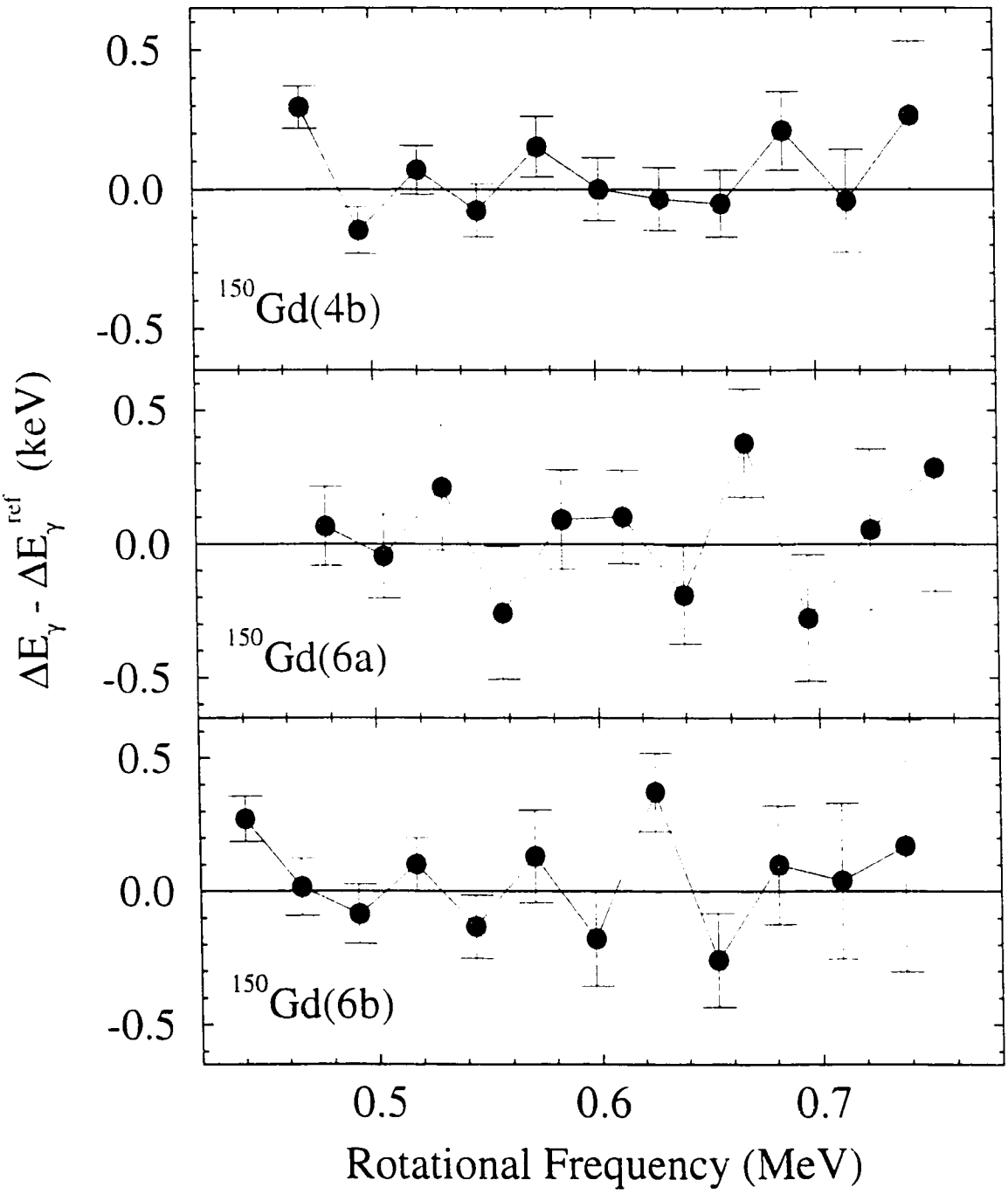

Figure 5.7: Staggering plots for bands in ^{150}Gd identical to ^{149}Gd(1).

Table 5.9: Gamma-ray transition energies, in keV, for bands in ^{151}Gd.

Band 1a	Band 1b	Band 3a
873.8(2)	895.7(2)	1000.6(3)
916.8(3)	939.3(2)	1046.0(3)
960.6(3)	983.1(3)	1092.6(5)
1004.4(2)	1028.0(3)	1139.0(4)
1049.6(2)	1073.5(3)	1187.1(5)
1096.9(3)	1120.8(3)	1235.7(4)
1144.4(2)	1169.1(7)	1286.6(5)
1193.5(2)	1218.5(3)	1338.3(5)
1243.1(3)	1269.2(3)	1388.8(6)
1294.8(3)	1320.5(3)	1443.9(6)
1346.8(3)	1372.7(4)	1498.4(7)
1399.9(4)	1426.1(4)	
1453.0(5)	1479.8(5)	
1507.0(5)		
1561.8(9)		

Band 6b does seem to have a regular staggering pattern. The amplitude is small so that, despite small error bars, the effect is only 1.8 standard deviations away from the null result. It is interesting to note that this band is isospectral with ^{149}Gd(1) and ^{148}Eu(1), and that its staggering as a function of rotational frequency is in phase with the latter.

The results for band 6b are also interesting as a test of Pavlichenkov's model. If this band is a *bona fide* example of a staggering band, then it is intriguing to ask why the $[521]3/2_{(-)}$ orbital should preserve $\Delta I = 4$ bifurcation, but the positive-signature orbital should destroy it (c.f. band 6a). According to Pavlichenkov's model, there is no distinction between these two orbitals, so a different result for the two cases is troubling.

Figure 5.8 shows the staggering plots for ^{150}Gd(1) and ^{151}Gd(1a,1b,3a). All

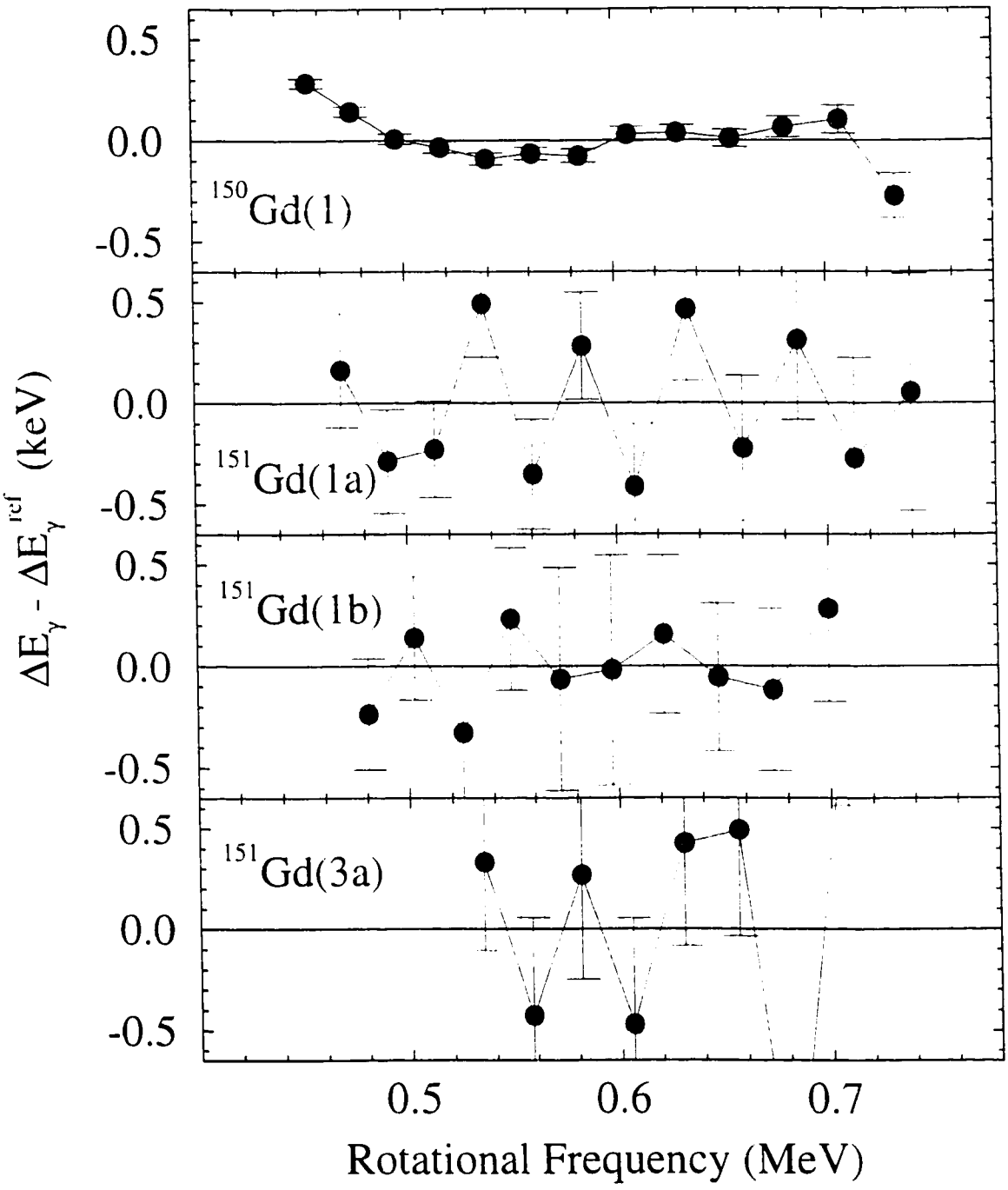

Figure 5.8: Staggering plots for bands identical to ^{150}Gd(1).

of these bands are built on $\pi 6^2 \nu 7^2$ intruder configurations, as discussed above. Their structure is, therefore, sufficiently different from ^{149}Gd(1) for the model of Hamamoto and Mottelson to have no predictive power. However, Pavlichenkov's prediction for this intruder configuration is definite. The moment Q_{44} is negative for both the proton and neutron subsystems, and thus no staggering is expected.

Indeed, no staggering is evident for ^{150}Gd(1), ^{151}Gd(1b), or ^{151}Gd(3a), although the error bars in the latter two cases are large. The plot for ^{151}Gd(1a) is suggestive. The mean staggering is larger in this case than for ^{150}Gd(6b); however, the uncertainties are also larger, and the level of significance of this result is approximately the same. If this case of staggering is more than a statistical fluctuation, it is certainly unexpected, especially since the other bands presented in Figure 5.8, with similar structures, show no such behaviour. The argument is the same as for ^{150}Gd(6a) and ^{150}Gd(6b): why should the staggering of a band depend on which signature of the low-j orbitals is occupied?

Finally, Figure 5.9 shows several bands with more exotic structures. Band 2 in ^{150}Gd has a $\pi 6^4 \nu 7^2$ configuration, and is identical to ^{152}Dy(1). That this band does not stagger is in accord with Pavlichenkov's prediction for this intruder configuration. It can also be reconciled with the constant-parameter extension of the Hamamoto and Mottelson model: since neither band staggers, one only has to assume that $B_1 = 0$ for these bands. However, one should remember the results of Section 5.2.3 for ^{148}Gd(5), a band identical to ^{152}Dy(1) that does stagger. The results for these three identical bands cannot be understood together in either model.

Band 8a in ^{150}Gd does not stagger, either. Since this band has a $\pi 6^3 \nu 7^1$ intruder configuration, it is unlike any of the bands studied so far. The model of Hamamoto and Mottelson is, therefore, not useful here; Pavlichenkov's model is also

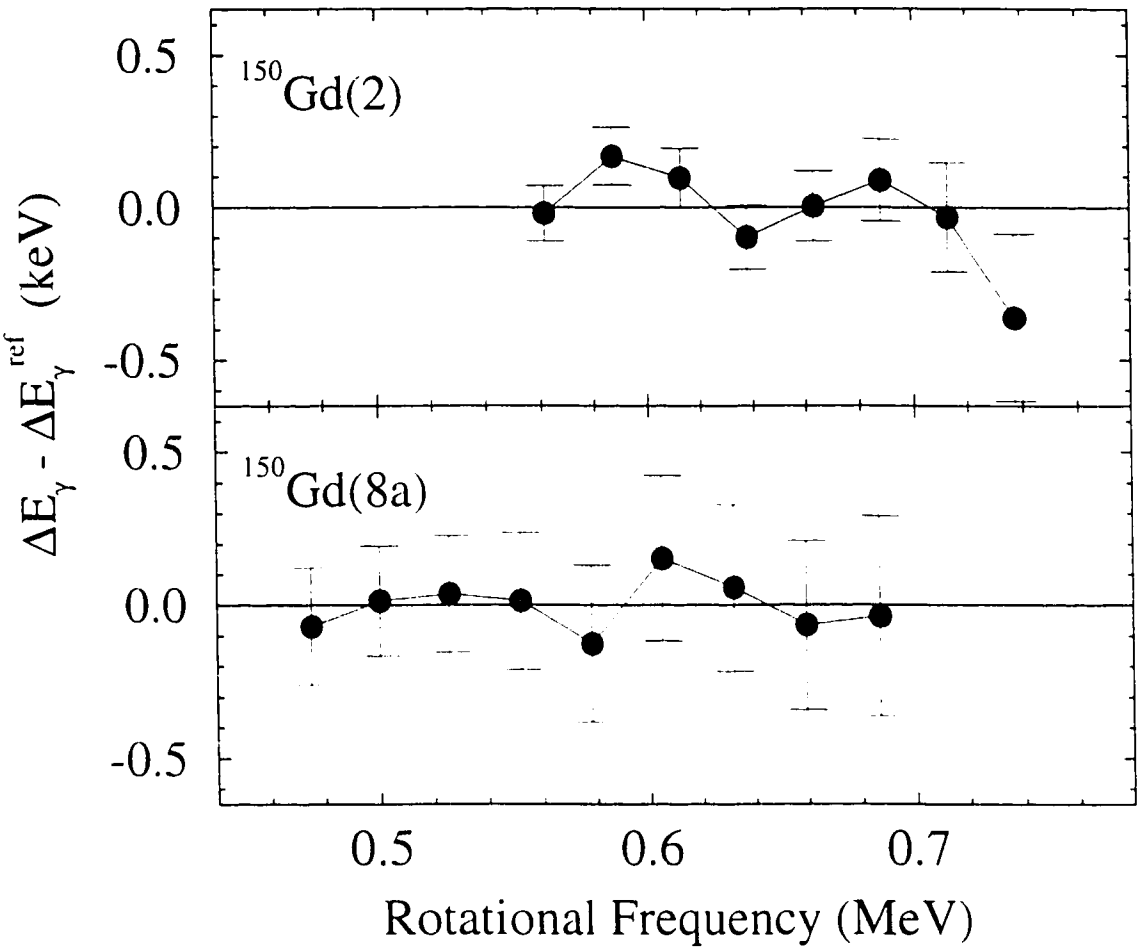

Figure 5.9: Staggering plots for more bands in ^{150}Gd.

ambiguous for this case.

5.5 Statistical Considerations

In Chapter 4, the statistical significances of the staggering patterns in ^{149}Gd(1), ^{148}Eu(1), and ^{148}Gd(6) were discussed. Procedures were developed for calculating the mean staggering X, its significance Y, and the probability P that a measurement of a perfectly regular band would produce a mean staggering of $|X|$ or larger as a

result of statistical fluctuations. It was shown that the significance of each of the patterns in Chapter 4 is two to three standard deviations from the null result, and that the probability that such patterns would arise through chance is no larger than about two percent. It was argued that the staggering patterns in these bands are non-statistical in nature. However, now that staggering patterns have been extracted from twenty-two bands, it is worth looking at the properties of the Y' distribution.

Table 5.10 presents a summary of the staggering analyses presented in this thesis. The table shows the parameters $|X|$, Y', and P for each of the bands. To assist in the analysis of this data, Figure 5.10 shows a histogram of the significances. The dashed curve in the Figure is a Gaussian distribution with its area normalized to that of the histogram. The figure shows that there are still not enough cases to do a detailed statistical analysis. However, to a first approximation, the data below $Y' = 2$ is described by the Gaussian curve, suggesting that one can judge the significance of some of the cases at the left end of the histogram based on statistical considerations.

The most significant examples of the staggering effect are, not surprisingly, those discussed in Chapter 4 and ^{148}Gd(5). Taken individually, the staggering plots for these bands make the effect look very significant. The figure also shows that these examples stand considerably higher than the Gaussian distribution. However, the area under the Gaussian curve is non-negligible at these values of Y', and it is instructive to ask how many cases with this level of significance might be expected from a random sample of twenty-two bands.

The chance that the measurement of a non-staggering band will yield staggering with a significance greater than 2.3 is 2.1%. Thus, for a sample of twenty-two bands, 0.46 cases of this magnitude are expected. This makes the four observed cases look very significant; using a Poisson distribution with a mean of 0.46, the proba-

Table 5.10: Mean staggering $|X|$ and the staggering significance Y for the bands studied in this work. Also given is the probability P as defined in Chapter 4.

Band	Mean Staggering $\|X\|$ (keV)	Significance Y	Probability P
^{147}Eu(1)	0.074(78)	0.95	34%
^{147}Eu(3)	0.099(172)	0.58	56%
^{148}Eu(1)	0.30(13)	2.3	2.1%
^{148}Eu(2)	0.46(49)	0.94	35%
^{147}Gd(2)	0.002(41)	0.05	96%
^{147}Gd(3)	0.02(13)	0.15	88%
^{147}Gd(4)	0.03(19)	0.16	87%
^{148}Gd(1)	0.006(26)	0.23	82%
^{148}Gd(3)	0.01(10)	0.10	92%
^{148}Gd(4)	0.097(99)	0.98	33%
^{148}Gd(5)	0.22(8)	2.8	0.51%
^{148}Gd(6)	0.37(12)	3.1	0.19%
^{149}Gd(1)	0.21(9)	2.3	2.1%
^{150}Gd(1)	0.01(2)	0.50	62%
^{150}Gd(2)	0.01(7)	0.14	89%
^{150}Gd(4b)	0.066(65)	1.0	32%
^{150}Gd(6a)	0.008(128)	0.06	95%
^{150}Gd(6b)	0.18(10)	1.8	7.2%
^{150}Gd(8a)	0.02(15)	0.13	90%
^{151}Gd(1a)	0.35(19)	1.8	7.2%
^{151}Gd(1b)	0.07(28)	0.25	80%
^{151}Gd(3a)	0.008(324)	0.02	98%

bility of observing four or more cases is 0.2%. However, it must be noted that the probability of observing at least one case is 37%, and therefore it cannot be ruled out that one of these cases is only a statistical fluctuation[§].

Slightly less significant are those "suggestive" cases noted earlier in this chapter, ^{150}Gd(6b) and ^{151}Gd(1a). If these are *bona fide* examples of staggering, they

[§]The original ^{149}Gd(1) example is almost certainly not a fluctuation. The significance for this band quoted in this chapter is based on the results published by Flibotte *et al.*. However, the independent confirmation of this result in an earlier experiment by the 8π group, and in a later experiment at Eurogam II makes it much more significant.

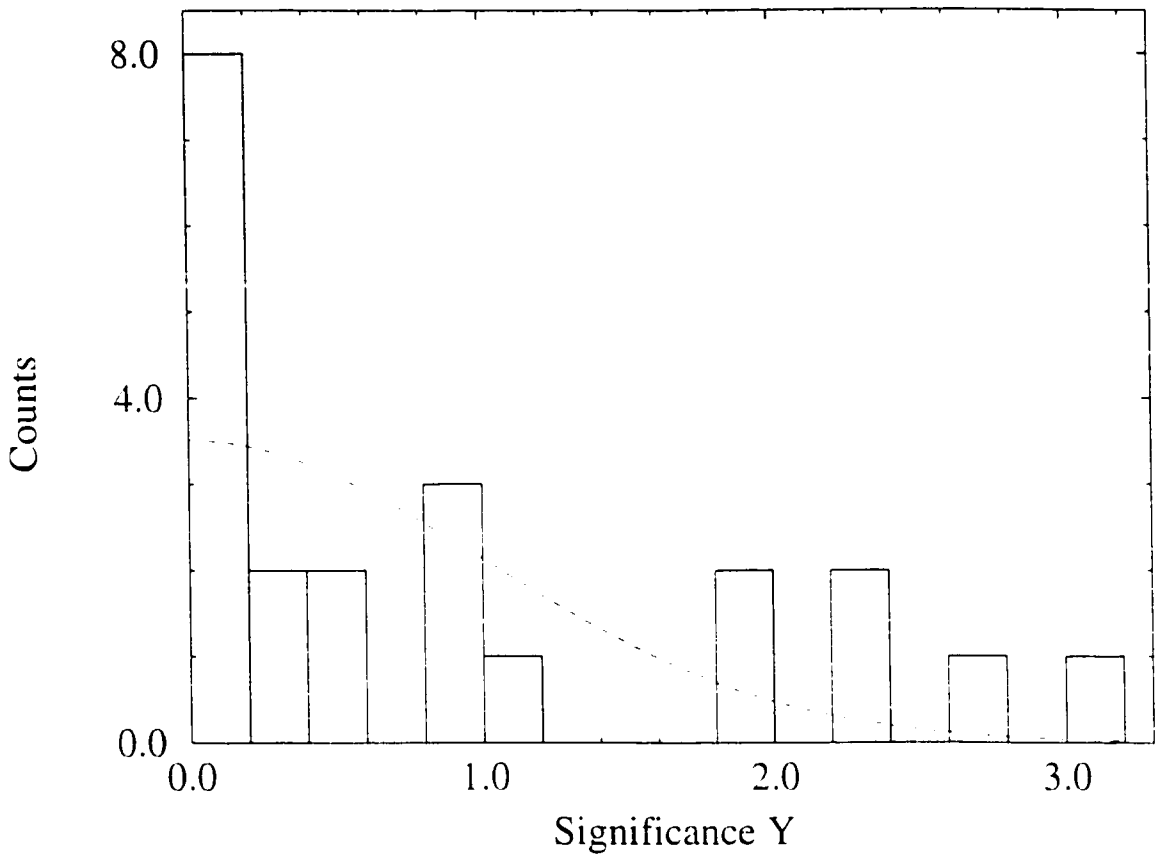

Figure 5.10: Staggering significance for the bands analyzed in this work. The dashed line is a Gaussian distribution, the area under which is equal to that of the histogram.

would be interesting for the reasons discussed earlier in this chapter. However, at this level of significance, they remain at the threshold of believability.

The probability that a measurement of a regular band yields staggering with significance greater than 1.8 and smaller than 2.3 (to separate this discussion from the previous one) is 5.0%. Therefore, a sample of twenty-two bands should yield 1.1 examples of this kind. The observed yield of two bands is not significant in this light, and in fact the probability of drawing two or more cases from a Poisson distribution with a mean of 1.1 is 30.4%. Thus, it is not proven that either of these bands exhibits

$\Delta I = 4$ bifurcation.

Before leaving this discussion, it is worth making some observations about the distribution as a whole. The mean of the squares of the significances is the reduced χ^2 statistic for this distribution (under the assumption that no bands exhibit staggering). The value of this statistic is 1.78. For a sample with twenty-two degrees of freedom, this is an unreasonably large value of χ^2; the probability of seeing a χ^2 this large is approximately $1 - 2\%$. This is an indication that the assumed distribution (no staggering) is inappropriate.

One could perform this test again after removing from the distribution the four most significant examples of the staggering phenomenon. The reduced χ^2 for this collection is 0.61, for eighteen degrees of freedom. This value seems too small: the probability that a correctly characterized distribution of this size gives a χ^2 this small is about 11%. This may indicate one of three things.

First, the data without the four most significant examples may be correctly characterized as a group of non-staggering bands. Events with occurrence probabilities of eleven percent do happen, and this could be one of those times.

Second, this may indicate a systematic bias on the part of the experimenter. The analyses of several bands were aborted because it seemed clear during the analysis that the band was being crossed or contaminated in some way that could not be corrected. Perhaps these deviations are genuine statistical fluctuations, and their exclusion from this distribution biases the sample toward small significances. This would result in a smaller value of χ^2, as observed.

Third, this may indicate that it is inappropriate to exclude all four of the staggering bands from the distribution. That is, it should be conceded that one of these cases is nothing more than a fluctuation. Adding, for example, the ^{148}Eu(1)

band back into the distribution changes the reduced χ^2 to 0.86; a distribution with nineteen degrees of freedom should get a χ^2 this large about 37% of the time.

It is unclear at this time which of the above three options is correct, and it is inappropriate at this time to speculate, based on the limited information available. It would clearly be useful to extend this survey to other bands, and to confirm the results for the large-Y cases presented in this work.

This chapter has presented the first systematic survey of $\Delta I = 4$ bifurcation in superdeformed bands. Mass-150 europium and gadolinium have been studied in great detail, yielding only one case as significant as those presented in Chapter 4. Pavlichenkov's model has been tested thoroughly, and that of Hamamoto and Mottelson has been tested as well, to the extent that this is possible. The following chapter summarizes the results of this work, and presents the conclusions which can be drawn from it.

Chapter 6

Conclusions

6.1 $\Delta I = 4$ Bifurcation in Identical Bands

The observation of $\Delta I = 4$ bifurcation in ^{149}Gd(1) was one of the most exciting discoveries in the study of superdeformed bands. Inspired by this result, the GS-64 experiment was performed. The goal of this experiment was to study superdeformed bands identical to ^{149}Gd(1) and to obtain further data related to the staggering effect.

Staggering patterns can be seen in two of the identical bands observed in this experiment, ^{148}Eu(1) and ^{148}Gd(6). Given the relative rarity of $\Delta I = 4$ bifurcation in superdeformed bands (demonstrated in this work), the occurrence of this phenomenon in three identical bands is most unusual. Even more striking is the graph of staggering versus angular momentum for these three bands, shown in Figure 4.5. This graph shows a remarkable correlation between the staggering patterns in the three bands, and raises a number of interesting issues. First, it suggests that there is some validity to the model of Hamamoto and Mottelson [Ham94], which claims that the staggering in the superdeformed bands is proportional to $\cos(\frac{\pi}{2}(I - I_0))$. Moreover, it suggests that the parameters A and B_1 that characterize this model are the same in all three identical bands, a totally unexpected finding. This vindication of Hamamoto and Mottelson's model is even more surprising since there is no known physical origin for

their Hamiltonian.

An effort has been made to evaluate the full staggering amplitude (not just the oscillatory cosine term) semi-classically for the Hamiltonian put forward by Hamamoto and Mottelson. The results of this work, summarized in Appendix B, have been used to constrain the model parameters A and B_1 by fitting the observed staggering patterns in the three identical bands to the expression derived in the Appendix. The possible values of the parameters are given in Table 4.3; it is not clear which of the three choices is correct, despite the fact that each option is different from the others by several orders of magnitude. It is expected that these parameters will put severe restrictions on future choices for the physical origin of this Hamiltonian.

These results suggest that there is some special connection between the staggering patterns in identical bands, and have motivated a wider study of $\Delta I = 4$ bifurcation in this mass region. Several more bands identical to ^{149}Gd(1) were studied; other identical-band families were also analyzed. This survey has yielded little further evidence of correlated staggering patterns in identical bands. Of the other bands identical to ^{149}Gd(1) (namely, ^{148}Eu(2) and ^{150}Gd(4b,6a,6b)), none exhibit staggering patterns with an amplitude or level of significance approaching that of the first three cases, and none fit on the curve of Figure 4.5. For the ^{148}Gd(5)-^{150}Gd(2) identical band pair, the former exhibits significant staggering while the latter does not. This is a damning result for two bands which should have the same spins. The ^{150}Gd(1) family (also including ^{151}Gd(1a,1b,3a)) are mostly non-staggering, although the result for ^{151}Gd(1a) is ambiguous. Finally, the triplet (^{148}Gd(1), ^{147}Eu(1), ^{147}Gd(4)) are all consistent with zero, as shown in Figure 5.6. Thus, the only correlation observed in identical band staggering patterns beyond the first three cases is in families where none of the members exhibit $\Delta I = 4$ bifurcation, a rather weak result.

6.2 Systematic Survey of $\Delta I = 4$ Bifurcation

The search for staggering in bands identical to ^{149}Gd(1) has permitted a much wider investigation of $\Delta I = 4$ bifurcation. In the course of this work, staggering plots have been produced for twenty-one superdeformed bands in ^{147,148}Eu and $^{147-151}$Gd. However, only three of these twenty-one bands exhibit staggering with statistical significance greater than 2.3.

This survey underlines a crucial question about the staggering phenomenon: what is it about ^{149}Gd(1) that brings about $\Delta I = 4$ bifurcation? Of the four known staggering bands, one is ^{149}Gd(1), and two others are identical to that band. This seems to indicate that ^{149}Gd(1) has a very peculiar property that brings about the effect, although it is unknown what this property is. Of course, any explanation should also explain the staggering in ^{148}Gd(5), a band with a very different structure.

6.2.1 Tests of the Models

A systematic survey of this kind is also useful to test models. In this work, the model of Hamamoto and Mottelson, and that of Pavlichenkov, have both been tested extensively.

The model of Hamamoto and Mottelson is not a good physical model, since it makes very few predictions. Certainly, it makes no predictions about what the parameters of the Hamiltonian should be for various bands, or even which bands should exhibit the effect. However, as discussed above, the results for the ^{149}Gd(1)-like bands observed in GS-64 are encouraging for proponents of this model, since the staggering patterns seem to lie along a common cosine curve. This suggests not only that the staggering is described by a cosine, but that the parameters of the Hamiltonian are the same for the three identical bands. This result has spawned

the so-called "constant-parameter extension" of the model, in which it is assumed that the parameters of the Hamiltonian are the same for pairs of identical bands. This extension of the model is testable. However, the lack of correlation between staggering patterns in all of the other identical bands (discussed earlier) indicates that this model is insufficient to describe this phenomenon.

Pavlichenkov's model is much more testable. His simple picture, in which $\Delta I = 4$ bifurcation is brought about by the Q_{44} moments of the high-j nucleons in partially filled shells (mainly intruders), makes definite predictions about where staggering should occur. These predictions are most reliable when the contributions to Q_{44} from the protons and neutrons have the same sign. When these contributions have opposite signs, one has to worry more about the relative magnitudes of the two contributions, and possibly the contributions from non-intruder orbitals. Pavlichenkov admits that ^{149}Gd(1) is one of these troubling cases, and one in which his calculations predict no staggering.

Table 6.1 summarizes the predictions of the Pavlichenkov model for the bands studied in this thesis. The bands are organized according to their intruder configurations, the dominant factor in whether a band will stagger. The $\pi 6^2 \nu 7^1$ bands are further broken down into two subsets. The first subset includes bands which differ from ^{149}Gd(1) by one or more holes in $N = 6$ neutron orbitals. These bands should stagger, by the arguments given in Section 5.2.3. The second subset differs from ^{149}Gd(1) only by holes in low-j orbitals. These bands should also stagger, because low-j particles have little effect on $\Delta I = 4$ bifurcation, in Pavlichenkov's model. The predictions in the table use the generous assumption that Pavlichenkov's calculations can be fixed up to produce staggering in ^{149}Gd(1) and no staggering in ^{152}Dy(1), another ambiguous case.

Table 6.1: A summary of the tests of Pavlichenkov's model made in this work. Given are Pavlichenkov's predictions (as "stag." or "no" for a prediction of staggering or no staggering, respectively), the actual results for these bands (using the same shorthand), and whether these results agree with the predictions (as "yes" or "no" for agreement or no agreement, respectively). The only bands omitted from this table are ^{147}Gd(3) and ^{150}Gd(8a) (for which the predictions are not clear), and ^{150}Gd(6b) and ^{151}Gd(1a) (for which the experimental evidence is not clear).

Intruder Configuration	Band	Prediction (stag./no)	Experiment (stag./no)	Agreement (yes/no)
$\pi 6^1 \nu 7^1$	^{147}Eu(3)	stag.	no	no
$\pi 6^2 \nu 7^0$	^{148}Gd(3)	no	no	yes
$\pi 6^2 \nu 7^1$	^{147}Eu(1)	stag.	no	no
	^{147}Gd(2)	stag.	no	no
	^{147}Gd(4)	stag.	no	no
	^{148}Gd(1)	stag.	no	no
	^{148}Gd(4)	stag.	no	no
$\pi 6^2 \nu 7^1$	^{148}Eu(1)	stag.	stag.	yes
	^{148}Eu(2)	stag.	no	no
	^{148}Gd(6)	stag.	stag.	yes
	^{150}Gd(4b)	stag.	no	no
	^{150}Gd(6a)	stag.	no	no
$\pi 6^2 \nu 7^2$	^{150}Gd(1)	no	no	yes
	^{151}Gd(1b)	no	no	yes
	^{151}Gd(3a)	no	no	yes
$\pi 6^4 \nu 7^2$	^{148}Gd(5)	no	stag.	no
	^{150}Gd(2)	no	no	yes

Table 6.1 also shows whether staggering was observed in these bands, and whether the theoretical prediction agrees with the experimental result. It is apparent that this theory has as many failures as it has successes. This indicates that Pavlichenkov has not correctly identified the origin of $\Delta I = 4$ bifurcation, or that his calculations of the Q_{44} moments are not accurate enough to make these predictions.

6.2.2 Statistical Significance

Now that so many bands have been measured, it is also possible to conduct a statistical examination of the staggering effect. Section 4.3.3 described a method by which the statistical significance Υ of the staggering in a given band may be evaluated. The significances for all of the bands studied in this work have been calculated and appear in Table 5.10; a histogram of this distribution can be seen in Figure 5.10.

The bands ^{149}Gd(1), ^{148}Eu(1), ^{148}Gd(6), and ^{148}Gd(5) all have staggering patterns with $\Upsilon > 2.3$. The statistical analysis presented in this thesis has shown that most, if not all, of these cases are not the result of statistical fluctuations. The probability of observing four staggering patterns with this level of significance in a sample of twenty-two bands is 0.2%, and the probability of observing no staggering patterns this significant in this sample is 63%. Thus, it is likely that all four of these bands are *bona fide* examples of $\Delta I = 4$ bifurcation.

The same cannot be said of the staggering patterns in ^{150}Gd(6b) and ^{151}Gd(1a). These patterns have significances of 1.8. In this sample of twenty-two bands, one expects 1.1 bands with staggering patterns with $1.8 < \Upsilon < 2.3$ purely by chance, and the probability of observing two or more bands at this level of significance is 37%. These statistics indicate that neither of these bands should be assumed to exhibit $\Delta I = 4$ bifurcation without an independent verification from a second experiment.

The distribution of eighteen non-staggering bands (not including the four cases with $\Upsilon > 2.3$) is reasonably well described by the assumption that none of these bands staggers. In fact, the χ^2 statistic for this distribution seems too small. This may be a chance occurrence; it may also indicate a systematic bias on the part of the experimenter, or that one of the four staggering bands is really nothing more than a statistical fluctuation. The choice between these options cannot be made now

on the basis of the facts at hand.

6.3 Future Prospects

This thesis has certainly extended the current knowledge of $\Delta I = 4$ bifurcation in the $A \sim 150$ region of superdeformation. However, there is considerable work yet to do.

It would certainly be useful to extend this survey into the rest of the mass region. Many superdeformed bands are known in the $A \sim 150$ terbium and dysprosium nuclei, and few of these have been examined for staggering. Indeed, the excited bands of ^{149}Gd should be investigated. There are, unfortunately, no more bands identical to ^{149}Gd(1), either observed or predicted; that study has been completed in this work. However, there are still good reasons to make new measurements in other bands. An expanded survey will provide more weight to the statistical conclusions that can be made, and it will provide more tests for the models. It should also be noted that there are many identical band pairs in this region, including some spectacular examples in which the $\pi[301]1/2_{(-)}$ orbital is involved; these could provide interesting test cases.

It would also probably be worthwhile to confirm or refute some of the results presented in this thesis. In the preceding section, it was noted that it is possible that one of the four best examples of staggering presented in this thesis may be a statistical fluctuation. It is also very likely that one or both of the $Y = 1.8$ cases is a fluctuation. A re-measurement of the staggering patterns in these bands would almost certainly settle these issues. For example, by merely repeating any of the experiments described in this thesis, the statistical error bars on the staggering plots could be reduced by a factor of $\sqrt{2}$, thus changing a $Y = 1.8$ result into a $Y = 2.5$ result, if the mean staggering X remains constant.

Finally, it is certain that more theoretical work on this phenomenon is required. This thesis has demonstrated that neither of the approaches considered in this work is capable of making accurate predictions of where the staggering will occur, or even of convincingly demonstrating what the origin of the phenomenon is. It is also fair to say that none of the many other proposed explanations has generated much interest, although that does not necessarily mean that those explanations are without merit. The large quantity of data presented in this thesis should provide ample tests for theoretical models, and the time is definitely ripe for an explanation of $\Delta I = 4$ bifurcation which can explain the pattern of occurrence observed in this work.

Appendix A

Oscillation of the Tunneling Amplitude

As described in Chapter 2, one begins with the Hamiltonian

$$H = AI_3^2 + B_1(I_1^2 - I_2^2)^2 \tag{A.1}$$

where the parameter B_2 has been set to zero. Hamamoto and Mottelson argue [Ham94] that A should be positive so as to keep the angular momentum perpendicular to the 3-axis. However, B_1 may be either positive or negative. For the rest of this discussion, B_1 will be assumed positive; negative values serve only to rotate the minima of the Hamiltonian through forty-five degrees around the 3-axis, and do not affect the tunneling calculations.

It is useful to switch to cylindrical co-ordinates (I, I_3, ϕ), where

$$I_1 = \sqrt{I^2 - I_3^2}\cos\phi \tag{A.2}$$

$$I_2 = \sqrt{I^2 - I_3^2}\sin\phi. \tag{A.3}$$

At this time, the notation is also changed slightly, with $I_3 \to K$, and $B_1 \to B$. This will eliminate the need for many subscripts and should make the following easier to read.

In these new co-ordinates and with these substitutions, the Hamiltonian becomes

$$H = AK^2 + B(I^2 - K^2)^2 \cos^2(2\phi). \tag{A.4}$$

This clearly has four minima in the $K = 0$ plane, at $\phi = \pi/4, 3\pi/4, 5\pi/4$, and $7\pi/4$, as discussed in Chapter 2. At these minima, the energy is equal to zero.

The quantity of interest is the tunneling amplitude, t. In the WKB approximation, this is given by

$$t = \exp(iS) \tag{A.5}$$

where S is the action for travelling from one minimum to another. For instance, S can be expressed as

$$S = \int_{\pi/4}^{3\pi/4} K(\phi)d\phi \tag{A.6}$$

where $K(\phi)$ is given by the solution of $H = 0$. That is,

$$AK^2 + B(I^2 - K^2)^2 \cos^2(2\phi) = 0. \tag{A.7}$$

The solutions of this equation are

$$K = \pm\sqrt{\frac{-A + 2BI^2\cos^2(2\phi) \pm \sqrt{A^2 - 4ABI^2\cos^2(2\phi)}}{2B\cos^2(2\phi)}}. \tag{A.8}$$

There are two choices to make here. The first is a choice between positive and negative K, and is arbitrary. Both choices describe equivalent paths between the minima of the Hamiltonian. The second choice is important, but relatively simple. Consider the limit $\cos(2\phi) \to 0$. In this limit K must also approach zero, since $\cos(2\phi) \to 0$ describes the minima of the Hamiltonian. However, only the positive root yields $K = 0$. Therefore, for this discussion the following solution will be used:

$$K = \sqrt{\frac{-A + 2BI^2\cos^2(2\phi) + \sqrt{A^2 - 4ABI^2\cos^2(2\phi)}}{2B\cos^2(2\phi)}}. \tag{A.9}$$

Qualitatively, this system has two types of behaviour, depending on the value of I. Consider first the case $I^2 < A/4B$. In this regime, the quantity in the innermost square root, that is $A^2 - 4ABI^2\cos^2(2\phi)$, is always positive. In turn, the argument of the outermost square root is always negative, and so K is always purely imaginary. Thus, the action is purely imaginary, and the tunneling amplitude is a real exponential with no oscillatory behaviour.

Conversely, if $I^2 > A/4B$, then the argument of the innermost square root always becomes negative for some ϕ values between the minima. Thus, the argument of the outermost square root is complex, and so K is complex. Thus, the action is complex, and the tunneling amplitude obtains a factor of $\cos(\Re(S))$ which may change sign as a function of spin. In the rest of this appendix, $\Re(S)$ will be determined, and thus the oscillatory nature of t.

The action integral is

$$S = \int_{\pi/4}^{3\pi/4} d\phi \sqrt{I^2 - \frac{A}{2B}\sec^2(2\phi) - \sqrt{\frac{A}{2B}}|\sec(2\phi)|\sqrt{\frac{A}{2B}\sec^2(2\phi) - 2I^2}}. \qquad (A.10)$$

The integrand depends on ϕ only through the cosine of 2ϕ, so the integral from $\pi/4$ to $\pi/2$ is the same as that from $\pi/2$ to $3\pi/4$. In addition, one might as well simplify the integral by changing variables to $\psi = 2\phi$. The integral becomes

$$S = \int_{\pi/2}^{\pi} d\psi \sqrt{I^2 - \frac{A}{2B}\sec^2\psi + \sqrt{\frac{A}{2B}}|\sec\psi|\sqrt{\frac{A}{2B}\sec^2\psi - 2I^2}}. \qquad (A.11)$$

Now, factor out $\sqrt{A/2B}$ and call $I\sqrt{2B/A} = \eta$ (note that the above condition on I^2 makes $\eta^2 > 1/2$). This leads to

$$S = \sqrt{\frac{A}{2B}} \int_{\pi/2}^{\pi} d\psi \sqrt{\eta^2 - \sec^2\psi + |\sec\psi|\sqrt{\sec^2\psi - 2\eta^2}}. \qquad (A.12)$$

For $\psi < \sec^{-1}(-\sqrt{2}\eta)$, the integrand is purely imaginary. For $\psi > \sec^{-1}(-\sqrt{2}\eta)$, the integrand has both real and imaginary parts. Since the goal of this Appendix is

the calculation of $\Re(S)$, it is sufficient to consider only this latter part of the integral. In this region, the integrand is of the form $\sqrt{(X+iY)}$, where $X = \eta^2 - \sec^2\psi$, and $Y = |\sec\psi|\sqrt{2\eta^2 - \sec^2\psi}$. A little algebra shows that the real part of this integrand is

$$\Re(\text{integrand}) = \frac{1}{\sqrt{2}}\sqrt{2\eta^2 - \sec^2\psi}. \tag{A.13}$$

Its integral is

$$\Re(S) = \sqrt{\frac{A}{4B}} \int_{\sec^{-1}(-\sqrt{2}\eta)}^{\pi} d\psi \sqrt{2\eta^2 - \sec^2\psi} \tag{A.14}$$

A final change of variables to $x = \sec^2\psi$ turns the integral into

$$\begin{aligned}
\Re(S) &= \sqrt{\frac{A}{4B}} \int_1^{2\eta^2} \frac{\sqrt{2\eta^2 - x}}{2x\sqrt{x-1}} dx && \text{(A.15)} \\
&= \frac{1}{4}\sqrt{\frac{A}{B}}(\pi\eta\sqrt{2} - \pi) && \text{(A.16)} \\
&= \frac{\pi}{2}\left(I - \sqrt{\frac{A}{4B}}\right) && \text{(A.17)} \\
&= \frac{\pi}{2}(I - I_0) && \text{(A.18)}
\end{aligned}$$

where the quantity $I_0 = \sqrt{A/4B}$ has been introduced.

Thus, the tunneling amplitude is of the form $t = |t|\cos(\frac{\pi}{2}(I - I_0))$, which not only changes sign, but does so every two units of spin, producing a staggering pattern like that observed in ^{149}Gd(1).

Appendix B

Calculation of the Staggering Amplitude

This appendix is a continuation of the discussion in Appendix A. The same Hamiltonian is used, which is written in cylindrical coordinates as

$$H = AK^2 + B(I^2 - K^2)^2 \cos^2(2\phi). \tag{B.1}$$

The staggering is proportional to the tunneling amplitude t, which is given by

$$t = \exp(iS), \tag{B.2}$$

where S is the action for tunneling between two minima of the Hamiltonian. In Appendix A, it was shown that this action is given by

$$S = \sqrt{\frac{A}{2B}} \int_{\pi/2}^{\tau} d\psi \sqrt{\eta^2 - \sec^2\psi} + |\sec\psi| \sqrt{\sec^2\psi - 2\eta^2}. \tag{B.3}$$

It was demonstrated that the real part of this expression leads to staggering proportional to $\cos(\frac{\pi}{2}(I - I_0))$. In this appendix the imaginary part of the expression will be evaluated to determine the amplitude of the oscillation.

The condition $\psi > \sec^{-1}(-\sqrt{2}\eta)$ has been identified as necessary and sufficient for the integrand to have both real and imaginary parts. Again, in this region, the integrand is of the form $\sqrt{(X + iY)}$, with $X = \eta^2 - \sec^2\psi$, and $Y = |\sec\psi| \sqrt{2\eta^2 - \sec^2\psi}$.

This makes the imaginary part of this integrand, in the region $\psi > \sec^{-1}(-\sqrt{2}\eta)$, equal to the surprisingly simple result, $\sec\psi/\sqrt{2}$. The integral of this term, called S_1, is given by

$$S_1 = i\sqrt{\frac{A}{4B}} \int_{\sec^{-1}(-\sqrt{2}\eta)}^{\pi} \sec\psi\, d\psi \tag{B.4}$$

$$= i\sqrt{\frac{A}{4B}} \ln(\sqrt{2}\eta + \sqrt{2\eta^2 - 1}) \tag{B.5}$$

$$= iI_0 \ln\left(\frac{I}{I_0} + \sqrt{\left(\frac{I}{I_0}\right)^2 - 1}\right) \tag{B.6}$$

where, once again the parameter $I_0 = \sqrt{A/4B}$ is used.

Now consider the region $\psi < \sec^{-1}(-\sqrt{2}\eta)$. The integral of this region is called S_2. In order to evaluate S_2, one factors out i from the integrand, moves the region of integration from $[\pi/2, \pi]$ to $[0, \pi/2]$, and exchanges the limits of integration. This changes the integral to

$$S_2 = i\sqrt{\frac{A}{2B}} \int_{\sec^{-1}(\sqrt{2}\eta)}^{\pi/2} d\psi \sqrt{\sec^2\psi - \eta^2} - \sec\psi\sqrt{\sec^2\psi - 2\eta^2}. \tag{B.7}$$

Now perform a change of variables to ξ where $\sec\psi = \sqrt{2}\eta\sec\xi$. A few lines of algebra later, the integral becomes

$$S_2 = iI \int_0^{\pi/2} \left(\frac{\sec\xi\tan\xi}{\sqrt{2\eta^2\sec^2\xi - 1}} - \frac{\tan^2\xi}{\sqrt{2\eta^2\sec^2\xi - 1}}\right) d\xi. \tag{B.8}$$

The two terms of this integral are tackled separately. The first term, hereafter called S_{21} is evaluated through the substitution $u = \sec\xi$. This yields

$$S_{21} = iI \int_1^{\infty} \frac{du}{\sqrt{2\eta^2u^2 - 1}} \tag{B.9}$$

$$= iI \lim_{x\to\infty} \frac{1}{\sqrt{2}\eta} \ln\left(\frac{\sqrt{2}\eta x + \sqrt{2\eta^2x^2 - 1}}{\sqrt{2}\eta + \sqrt{2\eta^2 - 1}}\right). \tag{B.10}$$

The second term, S_{22}, is solved with the substitution $u = \tan\xi$, becoming

$$S_{22} = -iI \int_0^\infty \frac{u^2 du}{(1+u^2)\sqrt{2\eta^2(1+u^2)-1}} \tag{B.11}$$

$$= -iI \lim_{x\to\infty} \left(\frac{1}{\sqrt{2}\eta} \sinh^{-1}\left(\frac{\sqrt{2}\eta x}{\sqrt{2\eta^2-1}} \right) \right. \tag{B.12}$$

$$\left. - \tanh^{-1}\left(\frac{x}{\sqrt{2\eta^2 x^2 + 2\eta^2 - 1}} \right) \right). \tag{B.13}$$

Taking these limits and combining these terms one obtains

$$S_2 = S_{21} + S_{22} = iI \left(\frac{1}{\sqrt{2}\eta} \ln\left(\frac{\sqrt{1-\frac{1}{2\eta^2}}}{1+\sqrt{1-\frac{1}{2\eta^2}}} \right) + \frac{1}{2} \ln\left(\frac{\sqrt{2}\eta+1}{\sqrt{2}\eta-1} \right) \right). \tag{B.14}$$

Thus, the tunneling matrix element is given by (using also the result of Appendix A)

$$t = \exp(iS) \tag{B.15}$$

$$= \exp(i\Re(S)) \exp(iS_1) \exp(iS_2) \tag{B.16}$$

$$= \frac{\left(\frac{I}{I_0}-1\right)^{(I-I_0)/2}}{\left(\frac{I}{I_0}+1\right)^{(I+I_0)/2}} \cos\left(\frac{\pi}{2}(I-I_0)\right). \tag{B.17}$$

Now one must relate t to the energy splitting. Griffiths [Gri95] states the result that for two harmonic oscillator-type wells separated by a high barrier, the energy splitting due to tunneling is given by $\frac{\hbar\omega_{\rm SHO}}{2\pi}\exp(iS)$, where $\omega_{\rm SHO}$ is the oscillator frequency (not to be confused with the rotational frequency ω of the rotating nucleus). For four oscillators in a ring geometry, as in this case, the result is a factor of two larger. One can find $\omega_{\rm SHO}$ for this case by considering the Hamiltonian for $K = 0$ and $\cos(2\phi) << 1$ (so the system is near the bottom of one of the minima). That is,

$$H = 4BI^4(\phi - \pi/4)^2. \tag{B.18}$$

This means that the oscillator "spring constant" k is given by $4BI^4$. In linear mechanics, k is related to $\omega_{\rm SHO}$ by $k = m\omega_{\rm SHO}^2$, where m is the mass of the system. In

this rotational system, m is replaced by $\mathcal{J}_3$, the inertial "mass" for movement in the direction of oscillation ϕ. Thus, $k = \mathcal{J}_3\omega_{\rm SHO}^2$ and since $A = 1/(2\mathcal{J}_3)$, one obtains

$$\omega_{\rm SHO} = 4I^2\sqrt{AB}. \tag{B.19}$$

This, combined with the result of Griffiths, gives the splitting of the energy levels brought about by tunneling between minima in the Hamiltonian of Hamamoto and Mottelson. And, since $(\Delta E_\gamma - \Delta E_\gamma^{\rm ref})$ is four times as large as the energy level splitting, the staggering is given by

$$\Delta E_\gamma - \Delta E_\gamma^{\rm ref} = \frac{16\hbar I^2\sqrt{AB}}{\pi}\frac{\left(\frac{I}{I_0}-1\right)^{(I-I_0)/2}}{\left(\frac{I}{I_0}-1\right)^{(I+I_0)/2}}\cos\left(\frac{\pi}{2}(I-I_0)\right) \tag{B.20}$$

$$= \frac{8A\hbar I^2}{\pi I_0}\frac{\left(\frac{I}{I_0}-1\right)^{(I-I_0)/2}}{\left(\frac{I}{I_0}+1\right)^{(I+I_0)/2}}\cos\left(\frac{\pi}{2}(I-I_0)\right). \tag{B.21}$$

This expression is fitted to the staggering data in Chapter 4.

Appendix C

Glossary of Symbols

The following is a glossary of the symbols used in this thesis. There are a few cases where the same symbol is used to mean two things. However, the meaning is always clear from the context in which the symbol is used. The section in which each symbol is first used is also indicated.

A	Atomic mass. (Chapter 1)
A	Parameter in the Hamamoto and Mottelson model. (Section 2.5.2)
a	Decoupling parameter. (Section 2.1)
$a_{\lambda\mu}$	Parameters in a description of the nuclear shape by spherical harmonics. (Section 1.1.3)
B	Synonym for B_1. (Appendix A)
B_1	Parameter in the Hamamoto and Mottelson model. (Section 2.5.2)
B_2	Parameter in the Hamamoto and Mottelson model. (Section 2.5.2)
$\mathcal{B}$	Parameter in the Pavlichenkov model. (Section 2.5.2)
C_n	A symmetry group in which the members are invariant under rotations of $360/n$ degrees. (Section 2.5.2)
c	Parameter in the Pavlichenkov Hamiltonian. (Section 2.5.2)
d	Parameter in the Pavlichenkov Hamiltonian. (Section 2.5.2)
E	Energy of a nuclear state. (Section 1.1.2)

E_γ	Gamma-ray energy. (Section 1.1.2)
$E_\gamma^{\rm ref}$	Gamma-ray energy of a reference band used in an alignment calculation. (Section 2.2.1)
$\Delta E_\gamma(I)$	Difference in energy between γ rays feeding and depopulating a state with angular momentum I. (Section 1.1.2)
$\Delta E_\gamma^{\rm ref}$	The smooth reference used in extracting the staggering. (Section 2.5.1)
e	Single-particle energy at $\omega = 0$. (Section 2.3)
e'	Single-particle energy at non-zero ω. (Section 2.3)
F	Parameter in Radford's parametrization of peak widths. (Section 4.3.2)
G	Parameter in Radford's parametrization of peak widths. (Section 4.3.2)
H	Parameter in Radford's parametrization of peak widths. (Section 4.3.2)
H	The Hamiltonian operator. (Section 2.1)
$H_{\rm coll}$	Collective part of the Hamiltonian operator, in the particle-rotor model. (Section 2.1)
I	Total nuclear angular momentum. (Section 1.1.2)
$I^{\rm ref}$	Total nuclear angular momentum of a reference band in an alignment calculation. (Section 2.2.1)
I_0	Parameter in the Hamamoto and Mottelson model, equal to $\sqrt{A/4B_1}$. (Section 4.1, Appendix A)
$I_\pm$	Angular momentum raising and lowering operators, respectively. (Section 2.5.2)
$\Delta i_{\rm inc}$	Incremental alignment. (Section 2.2)
Δi_x	Effective alignment. (Section 2.2)
$\mathcal{J}$	Moment of inertia. Subscripts may be used to denote the principal moments. (Section 1.1.2)
$\mathcal{J}^{(1)}$	Kinematical moment of inertia. (Section 1.1.2)
$\mathcal{J}^{(2)}$	Dynamical moment of inertia. (Section 1.1.2)
j	Total angular momentum of a particle. (Section 1.1.1)

j_+	Raising operator for j. (Section 2.1)
$\langle j_x^{(i)} \rangle$	Expectation value of j_x for the ith nucleon. (Section 2.2.1)
K	Synonym for I_3. (Appendix A)
k	Spring constant for a simple harmonic oscillator. (Appendix B)
l	Orbital angular momentum of a particle. The symbols s, p, d, f, g, h, ... are often used to denote $l = 0, 1, 2, \ldots$. (Section 1.1.1)
$\tilde{l}$	Pseudo-orbital angular momentum. (Section 2.4.1)
m	Mass of an object undergoing simple harmonic oscillation. (Appendix B)
N	Neutron number. (Section 2.3)
$\mathcal{N}$	Principal oscillator quantum number in the Nilsson model. Denotes the total number of oscillator quanta. (Section 1.1.2)
$\tilde{\mathcal{N}}$	Counterpart of the oscillator number $\mathcal{N}$ in the pseudospin framework. (Section 2.4.1)
n_3	Nilsson model label, indicating the number of quanta aligned along the long axis of the nucleus. (Section 1.1.2)
P	Probability that a staggering pattern as significant as that observed could result from the measurement of a regular band. (Section 4.3.3)
Q	Energy released in a reaction. (Section 3.1)
Q_{44}	Hexadecapole moment of the nucleus, important in the Pavlichenkov model. (Section 2.5.2)
R	Angular momentum of the nuclear core, in the particle-rotor model. (Section 2.1)
$R(\theta, \phi)$	Function in spherical coordinates defining the surface of the nucleus. (Section 1.1.3)
R_0	Parameter in the description of the nuclear shape. (Section 1.1.3)
$\mathcal{R}$	The Routhian, the Hamiltonian in the rotating frame of the nucleus. (Section 2.3)
$\tilde{s}$	Pseudo-spin. (Section 2.4.1)

S	Action for tunneling between minima. (Appendix A)
t	Tunneling amplitude. (Appendix A)
W	Peak width. (Section 4.3.2)
X	The mean staggering of a band, given by the mean of the distribution of $\bar{x}$'s. (Section 4.3.3)
x_i	The ith value of $\Delta E_i - \Delta E_i^{\mathrm{ref}}$. (Section 4.3.3)
$\bar{x}$	Average staggering, calculated with the formula $\bar{x} = \sum_{i=1}^{7}(-1)^i x_i$. (Section 4.3.3)
Y	Statistical significance of a staggering pattern, given by $Y = \lvert X\rvert/\sigma_X$. (Section 4.3.3)
$Y_{\lambda\mu}$	Spherical harmonic function. (Section 1.1.3)
Z	Proton number. (Section 2.3)
a	Signature, given by $j_x \bmod 2$. (Section 2.3)
β	Quadrupole deformation parameter in the Hill-Wheeler coordinates. (Section 1.1.1)
β_2	Alternate name for β. (Section 1.1.3)
β_4	Hexadecapole deformation parameter, equivalent to a_{40}. (Section 1.1.3)
γ	Quadrupole deformation parameter in the Hill-Wheeler coordinates. (Section 1.1.3)
δ_{ij}	The Kronecker delta, whose value is unity if $i = j$, and zero otherwise. (Section 2.4.1)
ϵ	Single-particle contribution to the nuclear Hamiltonian. (Section 2.1)
η	Parameter used in the solution of the Hamamoto and Mottelson Hamiltonian, equal to $I\sqrt{2B_1/A}$. (Appendix A)
Λ	Projection of the single-particle orbital angular momentum on the prolate axis. (Section 1.1.2)
$\bar{\Lambda}$	Counterpart of Λ in the pseudospin framework. (Section 2.4.1)
ν	Prefix indicating that the following orbital is a neutron orbital. (Section 1.3)

π	Prefix indicating that the following orbital is a proton orbital. (Section 1.3)
π	Parity. (Section 2.3)
σ_X	Standard deviation of the distribution of $\bar{x}$'s. (Section 4.3.3)
χ^2	The reduced χ^2 of a distribution is the mean of the significances Y. (Section 4.4.2)
Ω	Projection of the single-particle angular momentum on the prolate axis. (Section 1.1.2)
ω	Rotational frequency. (Section 1.1.2)
ω_{SHO}	Oscillator frequency for a simple harmonic oscillator. (Appendix B)

Bibliography

[Ari69] A. Arima, M. Harvey, and K. Shimizu, Phys. Lett. B **30**, 517 (1969).

[Bak95] C. Baktash, B. Haas, and W. Nazarewicz, Annu. Rev. Nucl. Part. Sci., **45**, 485 (1995).

[Bea93] C. W. Beausang, P. Fallon, S. Clarke, F. A. Beck, Th. Byrski, D. Curien, P. J. Dagnall, G. deFrance, G. Duchêne, P. D. Forsyth, B. Haas, M. J. Joyce, A. O. Macchiavelli, E. S. Paul, J. F. Sharpey-Schafer, J. Simpson, P. J. Twin, and J. P. Vivien, Phys. Rev. Lett. **71**, 1800 (1993).

[Bea95] C. W. Beausang, D. Prévost, M. H. Bergstrom, G. deFrance, B. Haas, J. C. Lisle, Ch. Theisen, J. Timár, P. J. Twin, and J. N. Wilson, Nucl. Instrum. Methods Phys. Res., Sect. A **364**, 560 (1995).

[Bea97] GS-43 data obtained and analyzed with permission from C. W. Beausang and P. Fallon.

[Bev92] P. R. Bevington, *Data Reduction and Error Analysis for the Physical Sciences*, McGraw-Hill, Toronto (1992).

[Boh51] A. Bohr, Phys. Rev. **81**, 134 (1951).

[Boh53] A. Bohr and B. R. Mottelson, Mat. Fys. Medd. Dan. Vidensk. Selsk. **27**, No. 16, 1 (1953).

[Boh75] A. Bohr and B. R. Mottelson, *Nuclear Structure II*, W. A. Benjamin, Don Mills (1975).

[Bur95] K. Burzyński, P. Magierski, J. Dobaczewski, and W. Nazarewicz, Phys. Scr. **T56**, 228 (1995).

[Byr90] T. Byrski, F. A. Beck, D. Curien, C. Schuck, P. Fallon, A. Alderson, I. Ali, M. A. Bentley, A. M. Bruce, P. D. Forsyth, D. Howe, J. W. Roberts, J. F. Sharpey-Schafer, G. Smith, and P. J. Twin, Phys. Rev. Lett. **64**, 1650 (1990).

[Byr98] Th. Byrski, O. Stezowski, K. Zuber, D. Appelbe, C. W. Beausang, F. A. Beck, A. Bouguettoucha, D. Curien, G. de France, G. Duchêne, S. Ertürk, C. Finck, B. Gall, B. Haas, A. Z. Kiss, N. Khadiri, B. Kharraja, A. Nourreddine, D. Prévost, H. Savajols, M. Smith, P. J. Twin, and J. P. Vivien, Phys. Rev. C **57**, 1151 (1998).

[Cau94] E. Caurier, A. P. Zuker, A. Poves, and G. Martínez-Pinedo, Phys. Rev. C **50**, 225 (1994).

[Ced94] B. Cederwall, R. V. F. Janssens, M. J. Brinkman, I. Y. Lee, I. Ahmad, J. A. Becker, M. P. Carpenter, B. Crowell, M. A. Deleplanque, R. M. Diamond, J. E. Draper, C. Duyar, P. Fallon, L. P. Farris, E. A. Henry, R. G. Henry, J. R. Hughes, T. L. Khoo, T. Lauritsen, A. O. Macchiavelli, E. Rubel, F. S. Stephens, M. A. Stoyer, W. Satuła, I. Wiedenhoever, and R. Wyss, Phys. Rev. Lett. **72**, 3150 (1994).

[Cro95] B. Crowell, M. P. Carpenter, R. G. Henry, R. V. F. Janssens, T. L. Khoo, T. Lauritsen, and D. Nisius, Nucl. Instrum. Methods Phys. Res., Sect. A **355**, 575 (1995).

[deA96] G. de Angelis, R. Wyss, D. Bazzacco, M. De Poli, A. Gadea, S. Lunardi, D. R. Napoli, C. M. Petrache, C. Rossi Alvarez, M. Sferrazza, and B. Rubio, Phys. Rev. C **53**, 679 (1996).

[deF95] G. de France, D. Prévost, J. C. Lisle, H. R. Andrews, G. C. Ball, C. W. Beausang, F. A. Beck, Th. Byrski, D. Curien, G. Duchêne, Ch. Finck, S. Flibotte, B. Gall, B. Haas, G. Hackman, V. Janzen, B. Kharraja, J. C. Merdinger, S. M. Mullins, S. Pilotte, D. C. Radford, C. Rigollet, H. Savajols, O. Stezowski, Ch. Theisen, P. J. Twin, J. P. Vivien, J. C. Waddington, D. Ward, L. Wei, K. Zuber, J. Dobaczewski, J. Dudek, W. D. Luo, A. Bouguettoucha, and W. Nazarewicz (unpublished).

[Don96] F. Dönau, S. Frauendorf, and J. Meng, Phys. Lett. B **387**, 667 (1996).

[Dud87] J. Dudek, W. Nazarewicz, Z. Szymanski, and G. A. Leander, Phys. Rev. Lett. **59**, 1405 (1987).

[Erc88] A. Ercan, R. Broda, P. Kleinheinz, M. Piiparinen, R. Julin, and J. Blomqvist, Z. Phys. A **329**, 63 (1988).

[Ert98] S. Ertück, Ph.D. thesis, University of Liverpool, Liverpool, United Kingdom.

[Fis96] S. M. Fischer, M. P. Carpenter, R. V. F. Janssens, B. Crowell, I. Ahmad, D. J. Blumenthal, T. L. Khoo, T. Lauritsen, D. Nisius, W. Reviol, W. F.

Mueller, L. L. Riedinger, B. H. Smith, and B. Cederwall, Phys. Rev. C **53**, 2126 (1996).

[Fle77] J. G. Fleissner, E. G. Funk, F. P. Venezia, and J. W. Mihelich, Phys. Rev. C **16**, 227 (1977).

[Fli93] S. Flibotte, H. R. Andrews, G. C. Ball, C. W. Beausang, F. A. Beck, G. Bélier, T. Byrski, D. Curien, P. J. Dagnall, G. de France, D. Disdier, G. Duchêne, Ch. Finck, B. Haas, G. Hackman, D. S. Haslip, V. P. Janzen, B. Kharraja, J. C. Lisle, J. C. Merdinger, S. M. Mullins, W. Nazarewicz, D. C. Radford, V. Rauch, H. Savajols, J. Styczen, Ch. Theisen, P. J. Twin, J. P. Vivien, J. C. Waddington, D. Ward, K. Zuber, and S. Aberg, Phys. Rev. Lett. **71**, 4299 (1993).

[Fli97] S. Flibotte, private communication (1997).

[Gri95] David J. Griffiths, *Introduction to Quantum Mechanics*, Toronto: Prentice-Hall Canada Inc., 1995.

[Haa90] B. Haas, D. Ward, H.R. Andrews, G.C. Ball, T.E. Drake, S. Flibotte, A. Galindo-Uribarri, V.P. Janzen, J.K. Johansson, H. Kluge, J. Kuehner, A. Omar, S. Pilotte, D. Prévost, J. Rodriguez, D.C. Radford, P. Taras, J.P. Vivien, J.C. Waddington and S. Åberg, Phys. Rev. C **42**, 1817 (1990).

[Hac95] G. Hackman and J. C. Waddington, Nucl. Instrum. Methods Phys. Res., Sect. A **357**, 559 (1995).

[Hac96] G. Hackman, Ph.D. thesis, McMaster University, Hamilton, Ontario, Canada (1996).

[Ham94] I. Hamamoto and B. R. Mottelson, Phys. Lett. B **333**, 294 (1994); Phys. Scr. **T56**, 27 (1995).

[Has94] D. S. Haslip, G. Hackman, and J. C. Waddington, Nucl. Instrum. Methods Phys. Res., Sect. A **345**, 534 (1994).

[Has97] D. S. Haslip, S. Flibotte, G. de France, M. Devlin, A. Galindo-Uribarri, G. Gervais, G. Hackman, D. R. LaFosse, I. Y. Lee, F. Lerma, A. O. Macchiavelli, R. W. MacLeod, S. M. Mullins, J. M. Nieminen, D. G. Sarantites, C. E. Svensson, J. C. Waddington, and J. N. Wilson, Phys. Rev. Lett. **78**, 3447 (1997).

[Has98a] D. S. Haslip, S. Flibotte, G. de France, M. Devlin, A. Galindo-Uribarri, G. Gervais, D. R. LaFosse, I. Y. Lee, F. Lerma, A. O. Macchiavelli, R. W. MacLeod, S. M. Mullins, J. M. Nieminen, D. G. Sarantites, C. E. Svensson, J. C. Waddington, and J. N. Wilson, Phys. Rev. C **57**, 442 (1998).

[Has98b] D. S. Haslip, N. Kintz, S. Flibotte, R. A. E. Austin, G. de France, M. Devlin, Ch. Finck, A. Galindo-Uribarri, G. Gervais, D. R. LaFosse, T. J. Lampman, I. Y. Lee, F. Lerma, A. O. Macchiavelli, R. W. MacLeod, S. M. Mullins, J. M. Nieminen, T. Rodinger, D. G. Sarantites, O. Stezowski, C. E. Svensson, J. P. Vivien, J. C. Waddington, D. Ward, and J. N. Wilson, Phys. Rev. C **57**, 2196 (1998).

[Hec69] K. T. Hecht and A. Adler, Nucl. Phys. **A137**, 129 (1969).

[Hil53] D. L. Hill and J. A. Wheeler, Phys. Rev. **89**, 1102 (1953).

[Kra88] K. S. Krane, *Introductory Nuclear Physics*, John Wiley and Sons, Toronto (1988).

[Kru96] R. Krücken, G. Hackman, M. A. Deleplanque, R. V. F. Janssens, I. Y. Lee, D. Ackermann, I. Ahmad, H. Amro, S. Asztalos, D. J. Blumenthal, M. P. Carpenter, R. M. Clark, R. M. Diamond, P. Fallon, S. M. Fischer, B. Herskind, T. L. Khoo, T. Lauritsen, A. O. Macchiavelli, R. W. MacLeod, D. Nisius, G. J. Schmid, F. S. Stephens, and K. Vetter, Phys. Rev. C **54**, R2109 (1996).

[Lee90] I. Y. Lee, Nucl. Phys. **A520**, 641 (1990).

[Leo87] W. R. Leo, *Techniques for Nuclear and Particle Physics Experiments*, New York: Springer-Verlag, (1987).

[Mac95] A. O. Macchiavelli, B. Cederwall, R. M. Clark, M. A. Deleplanque, R. M. Diamond, P. Fallon, I. Y. Lee, F. S. Stephens, and S. Asztalos, Phys. Rev. C **51**, R1 (1995).

[Mag95] P. Magierski, K. Burzyński, J. Dobaczewski, and W. Nazarewicz, Acta Phys. Pol. B **26**, 291 (1995).

[Mar97] G. Martínez-Pinedo, A. P. Zuker, A. Poves, and E. Caurier, Phys. Rev. C **55**, 187 (1997).

[Mik95] I. N. Mikhailov and P. Quentin, Phys. Rev. Lett. **74**, 3336 (1995).

[Nil55] S. G. Nilsson, Mat. Fys. Medd. Dan. Vidensk. Selsk. **29**, No. 16, 1 (1955).

[Nya84] B. M. Nyakó, J. R. Creswell, P. D. Forsyth, D. Howe, P. J. Nolan, M. A. Riley, J. F. Sharpey-Schafer, J. Simpson, N. J. Ward, and P. J. Twin, Phys. Rev. Lett. **52**, 507 (1984).

[Pal85] G. Palameta and J. C. Waddington, Nucl. Instrum. Methods Phy. Res., Sect. A **234**, 476 (1985).

[Pav95] I. M. Pavlichenkov and S. Flibotte, Phys. Rev. C **51**, R460 (1995).

[Pav97a] I. M. Pavlichenkov, Phys. Rev. C **55**, 1275 (1997).

[Pav97b] I. M. Pavlichenkov, JETP Lett. **66**, 796 (1997).

[Pav98] I. M. Pavlichenkov, private communication.

[Pol62] S. M. Polikanov, V. A. Druin, V. A. Karnaukhov, V. L. Mikheev, A. A. Pleve, N. K. Skobelev, G. M. Ter-Akopyan, and V. A. Fornichev, Soviet Phys. JETP **15**, 1016 (1962).

[Pre75] M. A. Preston and R. K. Bhaduri, *Structure of the Nucleus*, Addison-Wesley Publishing Company, Don Mills (1975).

[Rad85] D. C. Radford, RADWARE suite of programs (1985).

[Rad94] D. C. Radford, Nucl. Instrum. Methods Phys. Res., Sect. A **361**, 297 (1994).

[Rag90] I. Ragnarsson, Nucl. Phys. **A520**, 67c (1990).

[Rag91] I. Ragnarsson, Phys. Lett. B **264**, 5 (1991).

[Rag93] I. Ragnarsson, Nucl. Phys. **A557**, 167c (1993).

[Rev96] W. Reviol, H. Q. Jin, and L. L. Riedinger, Phys. Lett. B **371**, 19 (1996).

[Ril96] M. A. Riley, J. Simpson, T. B. Brown, D. E. Archer, J. Döring, P. Fallon, C. Kalfas, J. F. Sharpey-Schafer, and S. L. Tabor, in *Proceedings of the Conference on Nuclear Structure at the Limits*, ANL/PHY-97/1, 136 (1996).

[Rin80] P. Ring and P. Schuck, *The Nuclear Many-Body Problem*, Springer-Verlag, New York (1980).

[Sar96] D. G. Sarantites, P.-F. Hua, M. Devlin, L. G. Sobotka, J. Elson, J. T. Hood, D. R. LaFosse, J. E. Sarantites, and M. R. Maier, Nucl. Instrum. Methods Phys. Res., Sect. A **381**, 418 (1996).

[Sem96] A. T. Semple, P. J. Nolan, C. W. Beausang, S. A. Forbes, E. S. Paul, J. N. Wilson, R. Wadsworth, K. Hauschild, I. M. Hibbert, R. M. Clark, J. Gizon, A. Gizon, D. Santos, and J. Simpson, Phys. Rev. Lett. **76**, 3671 (1996).

[Sin96] B. Singh, R. B. Firestone, and S. Y. F. Chu, Nucl. Data Sheets **78**, 1 (1996), and references therein.

[Ste90] F. S. Stephens, Nucl. Phys. **A520**, 91c (1990).

[Str67] V. M. Strutinsky, Nucl. Phys. **A95**, 420 (1967).

[Sun95] Y. Sun, J.-y. Zhang, and M. Guidry, Phys. Rev. Lett. **75**, 3398 (1995).

[Sve98] C. E. Svensson, private communication (1998).

[The96] Ch. Theisen, N. Khadiri, J. P. Vivien, I. Ragnarsson, C. W. Beausang, F. A. Beck, G. Belier, T. Byrski, D. Curien, G. de France, D. Disdier, G. Duchêne, Ch. Finck, S. Flibotte, B. Gall, B. Haas, H. Hanine, B. Herskind, B. Kharraja, J. C. Merdinger, A. Nourredine, B. M. Nyakó, G. E. Perez, D. Prévost, O. Stezowski, V. Rauch, C. Rigollet, H. Savajols, J. Sharpey-Schafer, P. J. Twin, L. Wei, and K. Zuber, Phys. Rev. C **54**, 2910 (1996).

[Tsa70] C. F. Tsang, and Sven Gösta Nilsson, Nucl. Phys. **A140**, 275 (1970).

[Twi86] P. J. Twin, B. M. Nyakó, A. H. Nelson, J. Simpson, M. A. Bentley, H. W. Cramer-Gordon, P. D. Forsyth, D. Howew, A. R. Mokhtar, J. D. Morrison, J. F. Sharpey-Schafer, and G. Sletten, Phys. Rev. Lett. **57**, 811 (1986).

[Viv96] J. P. Vivien, "Euroball Proposal — Staggering Effects in $N = 85$ Isotones: the ^{150}Tb case" (1996).

[Wil97a] J. N. Wilson and D. C. Radford, Nucl. Instrum. Methods Phys. Res., Sect. A **385**, 108 (1997).

[Wil97b] J. N. Wilson, R. A. E. Austin, D. S. Haslip, and J. C. Waddington, Nucl. Instrum. Methods Phys. Res., Sect. A **399**, 147 (1997).

[Zho97] X. H. Zhou, E. Ideguchi, Y. Gono, T. Kishida, S. Mitarai, T. Morikawa, H. Tsuchida, M. Shibata, H. Watanabe, M. Miyake, A. Odahara, M. Oshima, Y. Hatsukawa, S. Hamada, H. Iimura, M. Shibata, T. Ishii, and M. Ishihara, Z. Phys. A **358**, 285 (1997).